Marsbee - Swarm of Flapping Wing Flyers for Enhanced Mars Exploration

NASA Innovative Advanced Concepts (NIAC) Phase I

Final Report

Principle Investigator: Chang-kwon Kang[1]

Co-Investigators: Farbod Fahimi[1], Rob Griffin[1], D. Brian Landrum[1], Bryan Mesmer[1], Guangsheng Zhang[1], Taeyoung Lee[2], Hikaru Aono[3]

Additional Authors: Jeremy Pohly[1], Jesse McCain[1], Madhu Sridhar[1], Hunter Dunne[1], Giulia Palma[1], Shahrom Shahzad Doneshwar[1], Kelby L. Starchman[1], Gabriel M. Cavalheiro[1], Takuto Iriyama[1], Evan Kaufman[2]

Affiliation:

1. University of Alabama in Huntsville
2. George Washington University
3. Tokyo University of Science

Table of Contents

1   INTRODUCTION

1.1   Marsbees – Bioinspired Mars Flight Vehicles

Mars exploration has received significant interest from academia, industry, government, and the general public. Despite continued interest, flying on Mars remains challenging, mainly due to the ultra-thin Martian atmospheric density. Although the gravitational acceleration on Mars is 38% of Earth's 9.8 m/s^2, the Martian atmospheric density is only 1.3% of the air density on Earth. The aerodynamic forces are proportional to the ambient fluid density. Therefore, flying near the surface of Mars has been considered nearly impossible.

The proposed mission architecture (Fig. 1) consists of a Mars rover (already existing) that serves as a mobile base for Marsbees - a deployable swarm of small bioinspired flapping wing vehicles. In one ConOps scenario, each Marsbee would carry an integrated stereographic video camera and the swarm could construct a 3D topographic map of the local surface for rover path planning. These flying scouts would provide a "third-dimension" to the rover capabilities [1]. In other scenarios, each part of the swarm of Marsbees could carry pressure and temperature sensors for atmospheric sampling, or small spectral analyzers for identification of mineral outcroppings. In each scenario, the rover acts as a recharging and deployment/return station and data and communication hub.

Human exploration of Mars is one of the major objectives of NASA and commercial entities such as SpaceX and Boeing. The identified innovations unique to the bioinspired flapping Marsbee provide viable multi-mode flying mobility for Martian atmospheric and terrain exploration. A swarm of Marsbees provides an enhanced reconfigurable Mars exploration system that is resilient to individual component failures. These Marsbees can carry sensors and wireless communication devices in combination with a Mars rover and helicopters. These enhanced sensing and information gathering abilities can contribute to the following NASA Mars mission objectives: i) "Determine the habitability of an environment", ii) "Obtain surface weather
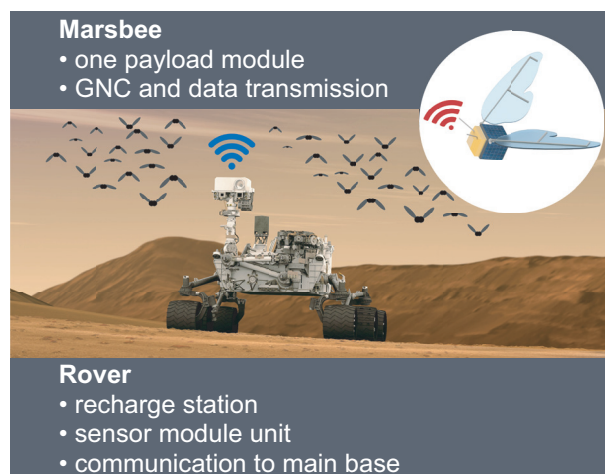
Figure 1. Marsbee architecture.

measurements to validate global atmospheric models", and iii) "Prepare for human exploration on Mars" [2]. Various commercial entities, e.g. SpaceX [3] and Boeing [4], are investing in technologies to transport humans to Mars.

1.2   Challenges to Flying on Mars

The force balance between a vehicle's weight and lift (Eq. 1) effectively summarizes the challenges to flying on Mars. In cruise flight, the wing lift L offsets the weight W as

$$W = mg_{mars} = L = \frac{1}{2}\rho_{mars}U^2SC_L \tag{1}$$

where C_L is the lift coefficient, and g_{mars} and ρ_{mars} are the Martian gravitational acceleration and atmospheric density, respectively. U is the reference velocity, m is the vehicle mass, and S is the wing planform area. Although g_{mars} is about one-third of the gravitational acceleration on Earth, the average Martian atmospheric density is only 1.3% of the air density on Earth [5,6] (see Fig. 2 with Mars Pathfinder data [7]). Aerodynamic forces are proportional to the ambient fluid density, implying that conventional terrestrial flight vehicle designs generate insufficient lift on Mars. Furthermore, oxygen is absent in the Martian atmosphere preventing the use of air-breathing propulsion.

The low density also leads to a relatively low operational Reynolds number Re of $O(10^2)$–$O(10^3)$ [5,8]. The dynamic viscosity coefficient on Mars is 1.5×10^{-5} kg/(ms) [9], similar to that on Earth - 1.8×10^{-5} kg/(ms). In these low Reynolds number regimes, the lift coefficients
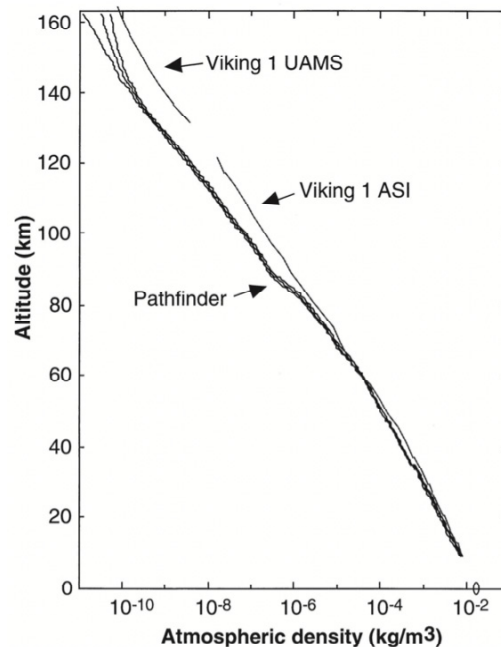
Figure 2. Mars Pathfinder data of the Mars atmospheric density [7].

2

of traditional fixed wing and rotary wing aircraft are significantly reduced [8,10]. To augment the reduced lift coefficient C_L, all conventional aircraft designs must fly faster (higher U) with a much lower wing loading m/S to compensate.

1.3   Prior Mars Flight Vehicle Designs

Several intriguing aerial vehicles have been proposed to overcome the challenges associated with flying on Mars. Dr. Aono, our international collaborator, provides a comprehensive review of these vehicles [6]. The Aerial Regional-scale Environmental Surveyor (ARES) is a rocket-powered, robotic airplane platform that was intended to aid the NASA Mars Exploration Program [11–16]. The prototype was designed to fly at Martian altitudes between 1 – 2 km. However, the ARES design does not permit landing on the Martian surface. The Mars Gashopper was a propulsion concept for a robust Mars flight vehicle that used CO_2 propellant to enhance mobility [17]. To explicitly tackle the issue of the low-density atmosphere, freely falling concepts [18] and Mars balloons [19,20] have also been proposed.

Insect-inspired lift production has also been considered to achieve flight on Mars. The Entomopter [21,22] is a flapping wing vehicle that uses a blown wing concept for lift enhancement. The Solid State Aircraft [23] is a solar-powered flapping wing aircraft that employs recent advancements in material science. However, both the Entomopter and the Solid State Aircraft designs are scaled-up versions of insects. The increase in the size of a vehicle generally yields a proportionally greater weight. When the wing length scale doubles, the wing area quadruples, and the volume increases by a factor of eight. Without a significant reduction in structural material density, a significant technological challenge, the vehicle weight will likewise increase by a factor of eight. This large weight increase negates the increase in lift, which makes it improbable for these vehicles to fly on Mars. This prior research in bio-inspired flight on Mars employed simplified aerodynamic tools that could not accurately predict the complex, unsteady flow resulting from flapping wing motion [21,22]. Most importantly, none of these designs have been realized and thus the goal of flight on Mars is still an open problem.

1.4   Current Mars Flight Vehicle Designs

Resurgent interest in manned and unmanned exploration of Mars has revitalized research into Mars flight vehicles. As a result, the likelihood of achieving flight on Mars is ever increasing. NASA JPL is currently considering a Mars Helicopter, which is slated to fly on the next Mars mission in 2020. While the Mars helicopter will likely be the first vehicle to achieve flight on Mars, there is room for improvement in Mars flight technology. For example, the Mars helicopter is limited to a purported 3 minutes of flight time each day [24], which may be a result of the known efficiency loss incurred by using rotorcraft lift production in low densities [8]. Additionally, the Mars helicopter is very large, with a rotor diameter of over 1 meter [24], thus requiring a large amount of transportation volume.

In light of these potential mission deficiencies inherent to rotorcraft, insect-inspired solutions for lift generation provide another set of Mars flight vehicle designs that are efficient,

robust, and compact. Insects operate in the same low Reynolds number regime on Earth as is present on Mars. They rely on unsteady aerodynamic mechanisms that are uniquely suited to low Re environments and lead to a high C_L [10]. This inspired the Marsbee design [25], which uses insect-inspired flapping wing motion to exploit unsteady lift-enhancing mechanisms in order to achieve lift in a Martian environment. This solution has been generated using a fully validated Navier-Stokes equation solver, designed for flapping wings at low Reynolds numbers, tightly coupled to a flight dynamics solver. This ensures that the resulting wing design and motion produces sufficient lift to balance its weight in the Martian conditions.

2   PROPOSED MARSBEE DESIGN AND TECHNICAL INNOVATION

The initial size and mass estimates for a realizable Marsbee are based on two existing terrestrial flapping wing vehicles. The first reference vehicle, the AeroVironment Nano Hummingbird [26], was reported in 2012 to have a wing span of 16 cm and a mass of 19 grams including motors, batteries, controls, communication, and color video camera. The fully controllable vehicle was able to freely hover and fly forward at 6.7 m/s for approximately 10 minutes. The second reference vehicle, the hummingbird Micro-Air Vehicle (MAV) (Fig. 3) [27,28], was developed by our Japanese collaborators. This vehicle weighs approximately 8 grams with motors, batteries, controls, and communications, but without a payload. This MAV can currently fly controlled for 5 to 10 minutes. After researching the current state of battery and sensor technology, we believe a 10 gram vehicle is currently realizable. Advances in miniaturization and energy storage, as well as multi-functional structures, will enable a future vehicle in the 6 gram range. Therefore, 6 grams is the nominal mass used in the following discussion.

The enabling innovation is two-fold: i) the use of dynamically scaled bioinspired motions to benefit from the high unsteady lift coefficients produced by insects; and ii) harvesting the kinetic energy of the flapping motions to reduce the inertial power and thus reduce the total flight power consumption.

2.1   Dynamically Scaled Marsbees

A consequence of the low density on Mars is that the operational Reynolds number of small flight vehicles is $O(10^2)$–$O(10^3)$ [5,6]. The dynamic viscosity coefficient on Mars is 1.5×10^{-5} kg/(ms) [9], similar to that on Earth: 1.8×10^{-5} kg/(ms). In these low Re regimes, the lift coefficients of traditional fixed wing and rotary wing aircraft are significantly reduced [8,10]. As illustrated by Eq. (1), to match the reduced lift coefficient C_L, all conventional aircraft designs must fly faster (higher U) with a much lower wing loading m/S to compensate.

The proposed Marsbees are dynamically scaled to benefit from the high lift coefficients $C_L = O(1)$ produced by insects in these low Reynolds number regimes [10]. The C_L in Eq. (1) is a function of a set of dimensionless parameters, $C_L = C_L(Re, M, k, AR)$ where M is the Mach number, k is the reduced frequency, and AR is the aspect ratio [10,29,30]. The wing motions and
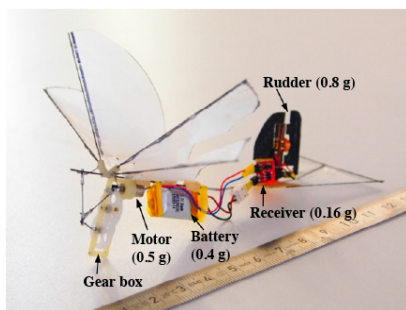
Figure 3. Hummingbird MAV [27,28].

geometric shapes should be designed such that the dimensionless numbers on Mars are within the insect flight regime that guarantees C_L remains high. Simply scaling up the wing size S or increasing U by flying or flapping faster alters these dimensionless numbers, leading to a reduced lift coefficient C_L and, hence, lower lift L.

Table 1. Bioinspired Marsbee dimensionless parameters are within the insect flight regime, benefitting from the high lift coefficients produced by insects. Marsbee solutions are determined using this concept of dynamic similarity. R is the wing length, c is the mean chord. The speed of sound on Mars, a_{mars}, is about 72% of that on Earth [8].

dimensionless parameter	definition	insect regime	small 0.21 g Marsbee	nominal 6 g Marsbee
Reynolds number, Re	$\rho_{mars} U c / \mu_{mars}$	$O(10^2\text{-}10^4)$ [10]	121	740
Mach number, M	U / a_{mars}	< 0.1	0.03	0.08
reduced frequency, k	$\pi f c / U$	$0.2 - 0.4$ [10,29]	0.32	0.32
aspect ratio, AR	R / c	$2 - 9$ [10]	3.3	3.3
dynamically similar?			yes	yes

Our preliminary results (Table 1) show that dynamically similar solutions exist for various vehicle sizes: i) A nominal-sized 6 gram Marsbee with a pair of 20 by 6 cm wings, flapping at 20 Hz and; ii) a small 0.21 gram Marsbee with a pair of 5 by 1.5 cm wings, flapping at 63 Hz. These motions and shapes yield dimensionless parameters that are within the insect flight regime (Table 1). Furthermore, substitution of these parameters in Eq. (1), where U is the maximum wing tip velocity, shows that these Marsbees yield sufficient lift to offset their total weight including the increased wing mass. The small Marsbee results were used to obtain a verified hover trim solution on Mars using a Mars flight simulator, which includes a fully validated Navier-Stokes equation solver [25,30–32], fully coupled with a flight dynamics solver [25,32]. The coupling between the Navier-Stokes equation solver and the flight dynamics solver is necessary to properly model the effects of both the important unsteady lift enhancement mechanisms [10,33] and the reduced gravitational acceleration environment on the resulting dynamics. In Phase I, we determined and validated a range of bioinspired Marsbee solutions with back of the envelope analysis (dimensional analysis as in Table 1 and lift requirement given by Eq. (1)), high-fidelity Mars flight simulator, and physical experiments.

2.2 Power Reduction by Energy Harvesting

While the low-density Mars atmosphere poses a challenge to generate lift, the proposed bioinspired flapping wing concept has the potential to benefit from the low-density environment by substantially reducing the flight power consumption, implying an improved payload margin and flight time.

Because of the ultra-low Martian density, the power consumption due to aerodynamic damping (aerodynamic power) is orders of magnitudes smaller than the power needed for
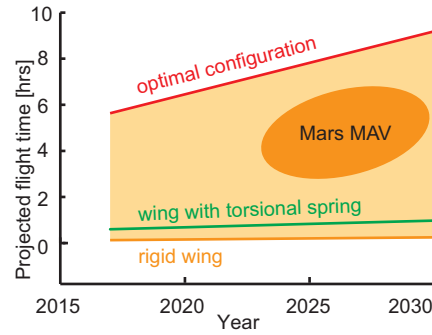
Figure 4. Projected flight times using flexible structures and projected advancements in battery energy density.

accelerating and decelerating the wings during flapping (inertial power). Therefore, the total power is dominated by the inertial power. A torsional spring at the wing root stores the wing kinetic energy during the decelerating half-cycle to drive the next accelerating half-cycle, reducing the inertial power when operating at resonance [34]. Whereas rotary wing concepts are more mature in both design and control, this energy harvesting mechanism is uniquely suited to flapping wing motions.

For a rigid wing structure, our Navier-Stokes equation calculations for our small Marsbee solution in Table 1 show that hover flight time is 8 min (0.13 hrs) with commercially available battery technology (Panasonic lithium-ion battery NCR18650B's specific energy: 243Wh/kg). Mounting a torsional spring at the wing root to reduce flapping inertial power can increase the hover time to an estimated 37 min (0.62 hrs). For a bioinspired flexible wing design with both the flapping and pitching inertial powers minimized, we expect the time to further improve to an optimal value of 348 min (5.8 hrs), a more than 40 fold increase over the rigid wing design. Assuming battery energy density increases to 400 Wh/kg by 2030 [35,36], an optimal configuration can hover for 9.5 hrs in 2030 as shown in Fig. 4. Flexible wings can also be made much lighter than a rigid wing, further enhancing the Marsbee performance.

3 PHASE I STUDY OVERVIEW

3.1 Project Approach

The proposed project combines expertise and talent from the US and Japan in a multidisciplinary effort to revolutionize the sensing and information gathering abilities on Mars.

3.2 Work Plan: Objectives

The objective of Phase I was to demonstrate that the proposed Marsbee can fly on Mars and to quantify the nominal power required, payload margin, and flight time. Also, the Marsbee architecture was assessed in the context of its proposed mission. Six specific objectives were to be addressed during Phase I, which were proposed as follows:

Objective 1. Determine the dynamically similar wing shape and motion that can hover in the Martian atmosphere.

Equation (1) and the dimensionless parameters (Table 1) will be used to determine the shape and motions of the dynamically similar Marsbees as a back of the envelope analysis. The Navier-Stokes and the flight dynamics equations will be simultaneously solved to verify these dynamically similar motions. The Navier-Stokes equations capture all bioinspired, unsteady, viscous aerodynamic mechanisms that insects use [10,30]. The numerical framework has been validated with a wide range of experiments [29,37–39].

Objective 2. Validate the numerical solution by replaying the motion and measuring the resulting forces and moments in a large vacuum chamber.

The air density inside a vacuum chamber at the UAH Propulsion Research Center (PRC) will be adjusted to simulate the atmospheric density on Mars. The vacuum chamber is 1.8 m in diameter and 4 m in length, and capable of achieving high vacuum (10^{-10} atm) [40]. The wing kinematics and shapes determined from the numerical solutions will be replayed on mechanical wing designs. Forces on the flapping wings will be measured from instrumented test stands. A motion tracking system will be placed in the chamber to record the wing motion (Fig. 5). We successfully measured the free flight of a Monarch butterfly with this motion tracking system at a density altitude of 3,000 m on Earth [41].

Objective 3. Assess the performance of an MAV in the Martian conditions.

The hummingbird MAV, developed by the Japanese team [27,28], is one of only a few robotic flappers in the world that can fly on Earth (Fig. 3). The hummingbird MAV will be redesigned by our international collaborator Aono with the wing shape, size, and kinematics determined from the numerical solutions. The Japanese team will visit UAH in Month 7 to help conduct flight experiments of the Mars-optimized micro-air vehicle (Marsbee) in the PRC vacuum chamber. Time-resolved kinematics of the wings and motion of the body of the Marsbee flight will be measured with the motion capture technique. We do not expect that the Marsbee in Phase I or Phase II will be fully

a) Large vacuum chamber and students   b) Setup inside the chamber   c) Flapping angle at 3,000 m
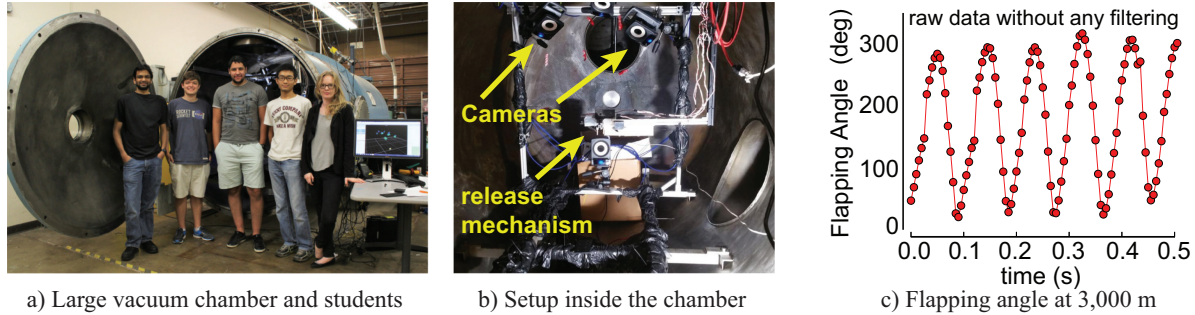
Figure 5. The large PRC vacuum chamber.

autonomous. Instead tethered flight will be considered with a counter balance to simulate the lower gravitational forces on Mars. The proposed flight-testing will identify important challenges that will be addressed in Phase II and beyond.

Objective 4. Use a system value model to quantify the worth of different systems and missions.

A significant challenge in the space community is justifying the selection of a specific mission from a set of possible missions or the selection of a system from a set of alternative systems. To overcome this challenge, systems engineers have used different decision analysis tools such as AHP [42] and QFD [43]. Major flaws in such approaches are found in the weights which are typically arbitrary, unitless, and subjective. We will use an improved approach to decision making - the system value model [44–49] - to quantify the worth of different systems and, in a broader view, the worth of different missions. A value model captures the primary attributes of a system and relates them to a single value, representative of the desires of the stakeholder. This value model will be used to compare different systems, e.g. rotary wing concepts that perform similar functions as the Marsbee, to show that the Marsbee architecture is the best system for the proposed mission. By determining the values of a set of alternative systems, a holistic comparison can be made and the alternatives can be rank ordered using a meaningful quantity.

Objective 5. Develop a conceptual Design Structure Matrix for the Marsbee.

A Design Structure Matrix (DSM) [50] is a decomposition of the system by process, people, or components. The decomposition captures the design variables (what the designer can change), the subsystems, and the links between the subsystems. A DSM will be created and combined with the value model to enable a mathematical understanding of the systems and optimize the design process.

Objective 6. Preparation for Phase II.

Identify any technical challenges that need to be addressed in Phase II.

9

3.3 Assessment Against Phase I Objectives

The objectives of Phase I (Section 3.2) are to use a high-fidelity, first principles physics model coupled with a flight dynamics solver to numerically investigate various Marsbee configurations. Dynamic scaling of these configurations consistent with terrestrial insects is a key aspect of this study. These numerical results were validated through selected experimental studies. This approach intends to confirm the feasibility of the Marsbee flying on Mars with an innovative energy harvesting mechanism to produce a usable payload margin and extended flight time. In addition, the Marsbee architecture was assessed in a mission context using a system value model and a Design Structure Matrix. In order to achieve the end goal of a Marsbee system, six specific goals were addressed during Phase I as shown in Table 2.

Table 2. Phase I specific objectives and outcomes.

	specific objectives	outcome	
1	Determine the dynamically similar wing shapes and motions that can hover in the Martian atmosphere.	success	§4
2	Validate the numerical solution by replaying the motion and measuring the resulting forces in a large vacuum chamber.	partial success	§5
3	Assess the performance of an MAV in the Martian conditions.	not met	§5
4	Use a system value model to quantify the worth of different systems and missions.	in process	§6
5	Develop a conceptual Design Structure Matrix for the Marsbee	success	§6
6	Preparation for Phase II.	success	§3.4, §8

The main findings are as follows.

1. Physics Modeling, Simulation, and Validation:

The initial stage of the research was mainly characterized by determining whether or not insect-inspired flapping wing motion could be used as a viable means of lift generation on Mars. In order to answer this question, we used a fully validated Mars flight simulator that tightly couples Navier-Stokes equations for low Reynolds number flapping wing motion to a multi-body flight dynamics solver. Numerical simulations including 3D and 2D Navier-Stokes equation solutions were conducted to identify combinations of wing shapes and motions that result in sufficient lift to hover on Mars. Wing shapes and motions were calculated using a zeroth-order method. This zeroth-order method is an algebraic approach that uses dimensional analysis to relate the insect flight flow regime to the bioinspired Mars flight flow regime. We argue that scaling up the wing area relative to a baseline insect and adjusting the wing kinematics appropriately is the most optimal approach. It was determined that such motion is achievable, and that dynamically scaled flapping wing motion on Mars can exploit unsteady lift enhancement mechanisms that are similar to insects on Earth.

Guided by numerical simulations, a flapping wing robot was designed for lift production

in a Martian density environment. Forces and wing deformations from this robot were measured in a vacuum chamber at Martian density conditions. These measurements indicate that ultra-low density detrimentally altered the lift producing ability of flapping wing motion, as anticipated. Positive lift that can sustain a Mars flight vehicle in the target mass range was measured when the flapping wing robot was properly scaled and sufficient kinematics were achieved. Although positive lifting forces were generated by the robot, achieving sufficient lift to hover in a predictable and controlled way can be hampered by the complex fluid-structure interactions. The fluid-structure interaction of relatively large flapping wings in an ultra-low density environment is inadequately understood. In particular, the wing deformation measurements suggest that the lift production is closely related to the passive pitch angle due to wing deformation, both of which are results of fluid-structure interaction.

2. Assessment and Feasibility of the Marsbee Architecture in a Mission Context

To identify the various subsystems of the Marsbee as well as the couplings that exist between the subsystems, a Design Structure Matrix (DSM) was formed [50–54]. This information is critical when developing system level models as well as to enable optimization of the system that addresses the subsystem couplings. A single Marsbee was decomposed into seven main subsystems: Battery, Motor, Frame, Gear Assembly, Wing, Control System, and Tail. The Motor and Gear subsystems consist of second-level subsystems. The preliminary DSM indicates that the subsystems are not fully coupled with respect to all coupling types: energy flow, vibrations, information flow, and force exerted, but that significant couplings do exist.

We employed a single iteration of a three-step approach to develop a Marsbee system value model and related the findings to previously developed NASA value models.

1. The templating step involved a brainstorming session within the research team to propose system level attributes that would be of importance to the stakeholder: range, payload size and mass, data type and transmission, modularity, robustness, and cost.

2. The evidence and analysis step involved the gathering of data to inform the value model interactions between attributes, and between attributes and value. Results indicate that subsystem mass and cost have a weak negative correlation, likely due to the narrow band of alternatives examined.

3. The stakeholder preference elicitation step was performed by surveying the Phase I team members, which consists of faculty members, graduate students, and undergraduate students in various Departments at the University of Alabama in Huntsville, George Washington University, and Tokyo University of Science. The results suggest that the issue of charging was important as well as the mission of monitoring a rover's path. Of less importance was the ability of Marsbee to equip specific sensors.

The findings from the three-step process relate highly to the NASA Mission value model previously researched [55], where knowledge, prestige, and avoidance of catastrophes

were identified as the key benefit-side system attributes. The evidence and questionnaire findings have a strong emphasis on knowledge as seen in the rover path monitoring, flight duration, and high sensor capabilities. All of these desires relate to enabling quicker knowledge gathering through a non-rover system, indicating the need to form a multi-system, mission-driven value model that includes a rover to interact with, e.g. the Marsbees.

3. Autonomous Exploration for 3D Topographic Mapping

To investigate the feasibility of autonomous exploration using Marsbees, we developed an optimal motion planning and guidance algorithm for a swarm of Marsbees. The mission objective was to construct a local 3D Mars topographic map by integrating depth measurements captured by a group of cooperating Marsbees. Our numerical simulations, in a simulated environment constructed by using contour data from the surface of Mars, illustrate the efficacy of the proposed exploration scheme and the feasibility of contrasting a 3D topological map with a group of Marsbees [56].

The environment is represented by a probabilistic occupancy grid map, modeled by a set of cells whose probability of occupancy is determined by the measurements from on-board depth scans. We employ the Bayesian framework where the current belief of the map is integrated with new measurements in an optimal fashion by gauging the level of confidence. The proposed stochastic framework for mapping quantifies the degree of uncertainties in a specific area of the map and the expected information gain for a given area of scanning. Utilizing these, we formulated an optimal autonomous exploration scheme, where Shannon's entropy serves as a measure of map uncertainty and the motion of Marsbees is guided to minimize the entropy. This distributes the sensing capability in an optimal fashion to maximize the information gain for topographic mapping [56]. It is further extended with a receding-horizon scheme such that Marsbees can react in real-time to avoid collision from unforeseen obstacles in dynamic environments.

3.4   Identified Key Remaining Unknowns and Challenges

The zeroth-order model and high-fidelity Navier-Stokes equation model results show that bioinspired Mars flight is feasible (Section 4.5.2). These Marsbees require significantly lower power resulting in a longer flight time (Sections 2.2 and 5.4) and can revolutionize Mars exploration by providing autonomous sensing platforms (Section 7).

In addition to these auspicious results, we have also identified several key remaining unknowns and challenges that must be addressed to facilitate a successful Marsbee exploration mission.

1. Flexible Flapping Wings in Martian Conditions

The zeroth-order and high-fidelity analyses in Phase I assumed a rigid wing. However, the large, thin Marsbee wings undergo relatively fast motions. As a result, the Marsbee wings significantly deform and the resulting lift is affected by the fluid-structure

interaction of the flexible wings.

Additional dimensionless parameters arise when flexible wings are considered. An important fluid-structure interaction parameter is the ratio between the fluid and structural densities [29,57]. The large discrepancy in the magnitude between the air density on Earth and Martian atmospheric density ($\rho_{mars} \approx 0.013 \rho_{earth}$) implies that preserving the density ratio is difficult. This qualitatively different fluid-structure interaction is illustrated in the proof-of-concept physical experiments (Section 5.1). The Marsbee wings in the ultra-thin Mars density do not deform in the same way as on Earth. Consequently, the passive pitch angles were not optimal. The resulting mean lift was sufficiently positive, however the nature of the fluid-structure interaction of flexible flapping wings in the Martian conditions must be understood to further optimize and control Marsbee flight.

Also, because of this challenge and funds arriving 2 months late, we have not had the time to design the Marsbee flapper mechanism to accurately replay the zeroth-order solution and to experimentally demonstrate the Marsbee take-off from the ground in the Martian density conditions.

2. System and Mission Analysis

We have developed the preliminary DSM and value model for the Marsbee (Section 6). However, system and mission analyses comparing the Marsbee architecture against existing Mars flight concepts (e.g. Mars helicopter and Netlander) must be performed to quantify the benefits of Marsbee exploration missions.

3. Autonomous Exploration of Swarm of Marsbees

The autonomous exploration scheme described in Section 7 is developed for an individual Marsbee. Cooperative autonomous aerial exploration and mapping schemes to generate a 3D topographic map must be developed for a group of Marsbees and the rover.

4 BIOINSPIRED LIFT GENERATION ON MARS

Bioinspired solutions for lift generation provides a unique set of Mars flight vehicle designs. For decades, the aerodynamics of insect flight remained inexplicable. A well-known example is the myth that bumblebees cannot fly according to classical aerodynamic theories [58]. Subsequent findings on unsteady lift production mechanisms [59–63] have enhanced our understanding of insect flight [10]. Insects rely on these unsteady aerodynamic mechanisms to produce high C_L values [10] in low Re environments, such as the Martian atmosphere.

Previous bioinspired concepts for Mars flight include the Entomopter, which is a flapping wing vehicle that uses a blown wing concept for lift enhancement, and the Solid State Aircraft, which is a solar-powered ornithopter [6]. However, both of these concepts suffer from the adverse effects of scaling up the entire vehicle in an effort to increase wing area. When the wing length scale l doubles to $2l$, the wing area quadruples to $4l^2$, but the volume increases by $8l^3$. As illustrated in Eq. (1), the lift increases with the wing area by $4l^2$, insufficient to offset the weight increase of $8l^3$. Without a significant reduction in structural material density, a substantial technological challenge, the vehicle weight will likewise increase enough to make it improbable that these vehicles could fly on Mars. Moreover, the analysis of the Entomopter was based on simplified aerodynamic models, not including all the unsteady low Re lift production mechanisms. They were forced to augment lift production with the blown wing in order to achieve the large lift coefficients which are routinely achieved by insect-style flapping wings [10].

One of the complexities associated with studying insect flight and developing bioinspired micro-air vehicles (MAVs) is the number of morphological, kinematic, and aero/structural/dynamic parameters involved. The vast amount of data available on flapping wing insects such as bumblebees, hawkmoths, fruit flies, dragonflies, etc. provides several potential starting points for a bioinspired flapping wing MAV. Rather than exploring the entire design space, we use dynamic similarity as a guideline to test the hypothesis that a bioinspired Mars flight vehicle can fly on Mars.

We consider the bumblebee as a starting point for the design. The primary reason for this choice comes from the observation that the wing-to-body mass ratio of bumblebees is only 0.52% [64]. A significant increase in the wing area increases the total mass by only a fraction. By contrast, the lowest wing to total mass ratios in aircraft are typically 10% for large cargo aircraft such as the Boeing 747 [65]. Furthermore, a bumblebee's ability to hover and operate at high forward speeds with heavy payloads makes it a particularly attractive candidate for biomimicry since this feature aligns with the design goals of reconnaissance MAVs in general.

That said, the scope of this task is limited to testing the hypothesis that a bioinspired hover solution exists when considering the coupled unsteady aerodynamics and flight dynamics. Since this is a question that has not been answered before, we believe that testing the existence of a bioinspired hover solution on Mars would be an appropriate first step before optimizing the performance.

4.1   Bioinspired Scaling

A consequence of the low density on Mars is that, as previously mentioned, the operational Reynolds number Re of small flight vehicles is $O(10^2)$–$O(10^3)$ [5,6]. In these low Re regimes, the lift coefficients of traditional fixed wing and rotary wing aircraft are significantly reduced [8,10]. As illustrated by Eq. (1), to match the reduced lift coefficient C_L, all conventional aircraft designs must fly faster (higher U) with a much lower wing loading m/S to compensate.

Marsbees must be dynamically scaled to benefit from the high lift coefficients $C_L = O(1)$ produced by insects in these low Reynolds number regimes [10]. The C_L in Eq. (1) is a function of a set of dimensionless parameters $C_L = C_L(Re, M, k, AR, AoA)$. The wing motions and geometric shapes must be designed such that the dimensionless numbers on Mars are within the insect flight regime that guarantees C_L remains high. Simply scaling up the wing size S or increasing U by flying or flapping faster alter these dimensionless numbers, leading to a reduced lift coefficient C_l and, hence, lower lift L.

Table 3. Dimensionless parameters, their definitions, and typical values which govern the high lift coefficients of insects.

dimensionless quantity	symbol	definition	typical value for insects [10]
aspect ratio	AR	$\dfrac{R^2}{S}$	$2 \le AR \le 10$
reduced frequency (hover)	k	$\dfrac{\pi f c}{U_{ref}} \rightarrow \dfrac{1}{2Z(AR)}$	$0.1 \le k \le 0.4$
Reynolds number	Re	$\dfrac{U_{ref} L_{ref}}{\mu} \rightarrow \dfrac{2\pi Z f R \hat{r}_2 c}{\mu}$	$O(10^2\text{-}10^4)$
angle of attack	AoA	$\dfrac{\pi}{2} - |\alpha|$	$\sim 45°$
wing tip Mach number	M_{tip}	$\dfrac{U_{ref}}{a} \rightarrow \dfrac{2\pi f Z R}{a}$	$M_{tip} \le 0.1$
lift coefficient	C_L	$\dfrac{L}{\frac{1}{2}\rho U_{ref}^2 S}$	$O(10^1)$

The proposed method seeks to ensure that the resulting body parameters and motion are dynamically similar to insects on Earth [66,67] and can therefore benefit from the high lift mechanisms typical of unsteady insect motion. We are motivated by the fact that insect lift coefficients with rigid wings are governed by five dimensionless parameters such that $C_L = C_L(Re, M, k, AR, AoA)$ [10,29]. These parameters are defined by combinations of

15

morphological and kinematic parameters as shown in Table 3.

In Table 3, R is the span of one wing, S is the planform area of one wing, f is the flapping frequency, c is the mean chord length, Z is the half peak-to-peak flapping amplitude, U_{ref} is the reference velocity taken at the second moment of area location along the span r_2 where $U_{ref} = 2\pi f Z R \hat{r}_2$, L_{ref} is a reference length, μ is the fluid dynamic viscosity, and a is the speed of sound. Using the ranges provided in Table 3 and the physical parameters defined in Fig. 6 for the Marsbee, a range of solutions with resulting dimensionless parameters in the insect regime can be determined for a given vehicle mass.
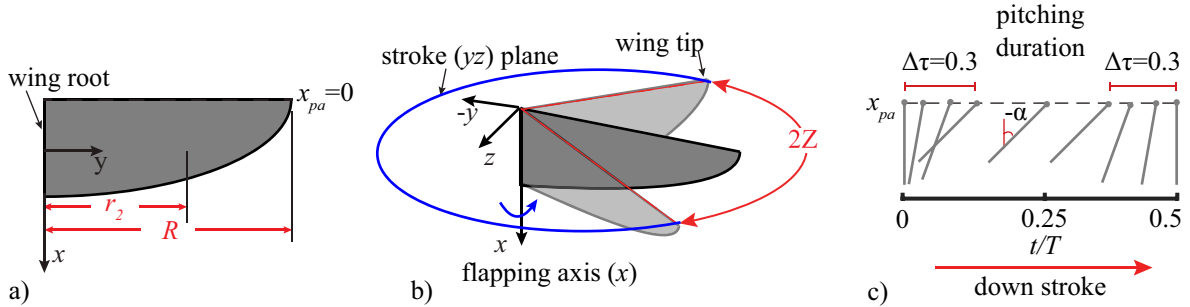
Figure 6. Schematic illustration of the key parameters for (a) the wing with pitch axis location x_{pa} at the leading edge (as used by some FWMAVs [27,68]), (b) the flapping motion, and (c) the pitching motion. The wing parameters are determined by considering a semi-elliptic wing, similar to the wing planforms used in practical applications of FWMAVs [27].

4.2   Modeling and Simulation of Bioinspired Flight on Mars

The objective of this task was to investigate the aerodynamic performance of a bioinspired flapping wing vehicle in Martian atmospheric conditions. There are multiple methods to accomplish this analysis.

One potential method is through scaling analysis. By systematically identifying important governing dimensionless parameters, we have determined key scaling relations between biological flight dynamics on Earth and bioinspired Mars aerodynamics. These scaling relations provide a zeroth-order model, which algebraically relates the governing dimensionless parameters to guide us in finding bioinspired wing shapes and motion as shown in Section 4.3.

Another potential method are the quasi-steady models. Although the nature of flapping wings is inherently an unsteady aerodynamic problem, there has been much success in modeling the physics with quasi-steady models. For example, Lentink and Dickinson [69] showed that quasi-steady rotational accelerations can play a more important role compared to unsteady accelerations. Additionally, the experimental work of Usherwood and Ellington [70,71] showed that the lift generated in the translational phase, as modeled by quasi-steady aerodynamics, is sufficiently high to balance weight in hover. Similarly, there are well validated theoretical models based on quasi-steady assumptions such as the blade element analysis [72] and the lifting line model [73] which can reasonably predict and model the forces produced by insect-like

vehicles.

However, it has been shown in our previous work [25] that wing-wake interaction, a nonlinear, unsteady aerodynamic effect, has a significant impact on the lift production, power required, and the flight dynamics. This leads us to use a Navier-Stokes (NS) equation solver which can accurately model this unsteady effect and therefore provide more accurate predictions of the vehicle's flight dynamics.

With this in mind, we use a combined zeroth-order model and the NS equations to solve for the flow around the wings of a bioinspired Mars MAV and properly account for unsteady lift enhancement mechanisms, including delayed stall, wake-capture, rotational lift, and added mass effects. Additional unsteady mechanisms such as clap-and-fling and Wagner's effect can play a role but are of less importance in this study. All relevant dimensionless parameters are preserved to benefit from the high lift coefficients produced by insects on Earth. The NS solver is tightly integrated with a flight dynamics solver to ensure that the resulting wing design produces sufficient lift to sustain the total weight of the flyer in hovering free flight. The understanding of the role of unsteady aerodynamic mechanisms in Martian conditions can help the development and validation of quasi-steady flapping wing aerodynamics models for Martian flight in the future. The wing size and flapping frequency are varied to assess their effects on the resulting lift and power.

We use 2D aerodynamics solutions, tightly coupled to 3DOF flight dynamics equations of motion. 2D flow solutions have previously been shown to be a good approximation of the 3D flapping wing aerodynamics at $Re=O(10^2)$ [74]. The main reason is that the effects of spanwise flow that seem to stabilize the LEVs [75] or LEV-tip-vortex interaction [76] on the overall aerodynamics are less important than at higher Reynolds numbers [62,77]. Also, the characteristics of the LEVs in two-dimensions for plunging motions are representative of 3D flapping wings as long as the stroke-to-chord ratio is within the typical range of insects, i.e. around 4 to 5 [78], which we consider in this study. That said, 3D effects including the downwash distributions [79,80] cannot completely be neglected. To test the validity of 2D NS solutions for bioinspired Mars flight, we compute 3D NS solutions and determine if sufficient lift for hover is generated on a dynamically scaled 3D wing, undergoing 3D wing motion in Section 4.5.

It is important to note that only the aerodynamics and the free flight dynamics are considered here without any consideration for actuator dynamics or added actuator mass. The wing weight is properly scaled when a larger wing is considered with the assumption that the scaled wing is the same constituent material as the baseline bumblebee wing. The body mass is kept as a constant. Despite the recent advancements in material science, developing an autonomously flying bee-scale robotic flyer is still a challenge even on Earth. Here we address the question of whether or not the flapping wing motion generates sufficient lift to sustain the weight of a wing-body configuration. Only after this fundamental question is positively answered can one consider developing a flapping wing robotic flyer and other components such as controllers, sensors, and power sources to actuate and sustain the motion (Section 8).

Additionally, this study is a prerequisite for optimizing the parameter design space, such as the wing kinematics, wing size, or adding power-saving devices, etc. The results of this investigation pave the way for system optimization and studying the effects of features such as wing flexibility as topics of future research, e.g. Phase II.

4.2.1 Wing Kinematics

The wing kinematics used in the computational model are described using bio-inspired relations [81]. The flapping motion with respect to the wing root is a sinusoidal function of time t described by

$$\zeta(t)=Z\cos\left(2\pi ft\right)+\zeta_{o} \tag{2}$$

where the flapping offset angle ζ_o biases the flapping toward the ventral ($+\zeta_o$) or dorsal ($-\zeta_o$) side of the wing root. We prescribe a pitch angle α as a rotation away from the vertical orientation in the stroke plane:

$$\alpha(t)=\frac{A}{\tanh\left(C_{\alpha}\right)}\tanh\left(C_{\alpha}\sin\left[2\pi ft-\alpha_{\phi}\right]\right) \tag{3}$$

where the pitch amplitude is denoted by A. The timing of wing rotation is controlled by α_φ, which can be positive for advanced rotation, zero for symmetric rotation, and negative for delayed rotation. Vertical deviation angle out of the stroke plane is not considered. Varying C_α from ∞ to 0 transitions from a square wave to a sinusoidal wave. The pitching amplitude and pitch phasing angle are assumed to be A=40° (refer to section 1 of the online supplemental material) and α_φ=0.3, corresponding to advanced pitch rotation which is known to yield the highest lift [61,82]. We set C_α=3.1, resulting in a modified square wave, as considered by other studies [63,83]. The angle of attack at any instant is approximately $AoA=\pi/2-|\alpha|$, although it also includes contributions from the body motion as well.

Motivated by the works of Badrya et al. [82] and Faruque and Humbert [84], we select the stroke plane angle β, flapping amplitude Z, and the flapping offset angle ζ_o, as the three control inputs to actuate the three degree of freedom (3-DOF) system. Each control primarily affects the vertical, horizontal, and angular degree of freedom, respectively.

4.2.2 Aerodynamics Modeling – Navier-Stokes Equation Solver

We consider hover and assume any aerodynamic forces generated by the body can be neglected [85]. We only simulate a single, rigid wing, assuming left-right symmetry of the system with respect to the longitudinal plane. We directly solve the incompressible NS equations

$$\nabla^* \cdot V^* = 0,$$

$$\frac{k}{\pi} \frac{\partial V^*}{\partial \tau} + \left(V^* \cdot \nabla^*\right) V^* = -\nabla^* p^* + \frac{1}{Re} \nabla^{*2} V^*, \tag{4}$$

to determine the pressure and shear stress distributions on the wing. The velocity field V is normalized with the reference velocity U, or $V^*=V/U$. Time is normalized by the flapping period $(1/f)$, $T=ft$. Lengths are normalized by the mean wing chord c, and pressure is normalized per $p^*=p/\rho U^2$.

These equations are solved using a fully-validated structured, finite-volume, pressure-based incompressible NS equation solver used extensively in flapping wing studies to calculate the velocity and pressure field around a flapping wing [29–31,86,87]. Remeshing is realized using the radial basis function interpolation scheme, shown to conserve good initial grid qualities and handle large wing motions and even deformations [10].

For all motions considered in this study, the resulting Reynolds number is in the range of $Re<1000$. In this Reynolds number regime, the fluid flow can be considered as laminar and the computational accuracy of the NS equation solver employed in this study is satisfactory [74].

The reduced frequency remains in the range of $k=0.29$ to 0.32 due to variations in the flapping amplitude from case to case. The wing section is rectangular and modeled as a rigid flat plate with a 2% thickness to chord ratio (Fig. 6). The solver determines forces and moments at a rate of 480 time steps per flapping period. The wing is moved at each time step in accordance with the wing kinematics and body motion determined by the trimmer. The grid and additional computational setup are described in the appendix. The grid and time-step sensitivity studies were presented in our work [57].

We tightly integrate the NS solver with a flight dynamics solver to create a Mars flight simulator to determine the control inputs and other initial conditions required for the vehicle to hover on Mars. Of particular importance is the requirement that the lift balances the weight,
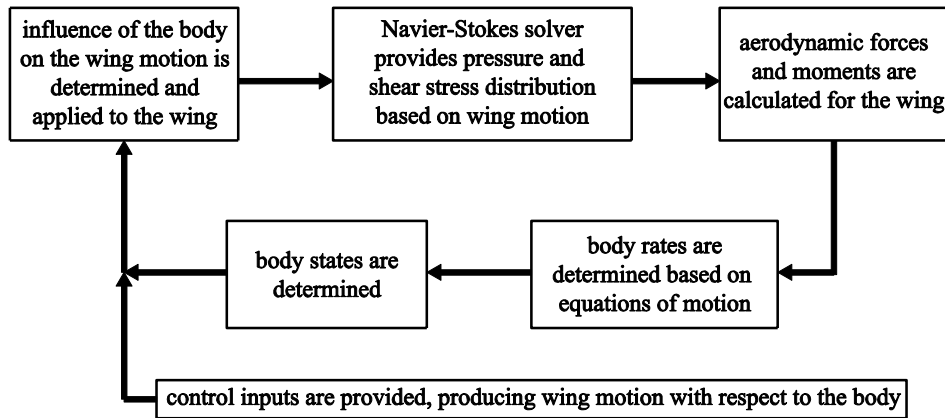
Figure 7. Computational framework based on previous work [25]. Flowchart describes the coupling between the NS and flight dynamics equations that occurs within a time step. The framework determines solutions for trimmed, hovering flight.

19

where the wing weight scales with n^3. For constant flapping frequency and amplitude, the resulting aerodynamic forces and moments scale with the wing scaling factor as n^4, as shown in equation (3).

The computational framework demonstrated in Fig. 7 is based on our recent work [25] which couples a 2D NS equation solver to a nonlinear multi-body flight dynamics equation solver. Aerodynamic forces and moments on the flapping wings yield the body motion, which in turn affects the instantaneous fluid dynamics on the wings. To simulate free flight, the wing motion with respect to the wing root is prescribed by the wing kinematic parameters, while the body motion is simultaneously applied to the wing root. Therefore, the motion of the wing with respect to the air is a superposition of these two motions. The equations of motion are integrated at every time step. Hence, in free flight, the motion at each time step is a result of both the dictated wing kinematics and the body's free response. A detailed description and validation of the flight dynamics model and the coupling to the NS equation solver is described in our previous work [25].

4.2.3 Dynamic Interaction Between the Body and Wing

We assume that the wing and body are rigid. The velocity $_b\mathbf{v}_{cg}$ and acceleration $_b\mathbf{a}_{cg}$ of the body center of mass in the body frame are given by

$$_b\mathbf{v}_{cg} = \begin{bmatrix} u & v & w \end{bmatrix}^T \tag{5}$$

$$_b\mathbf{a}_{cg} = \frac{d}{dt}\left(R_{b \to I}\,_b\mathbf{v}_{cg} \right) = _b\dot{\mathbf{v}}_{cg} + _b\boldsymbol{\omega}_{b/I} \times _b\mathbf{v}_{cg} \tag{6}$$

where the leading subscripts b and w indicate that the variable is expressed in the body and wing frames, respectively. The rotation matrix $R_{b \to I}$ transforms vector components from the body to inertial frame and $_b\boldsymbol{\omega}_{b/I}$ is the angular velocity vector of the body with respect to the inertial frame, expressed in the body reference frame.

The velocity and acceleration of the wing consist of both the prescribed kinematics with respect to the body as well as contributions from the body motion itself. The resulting motion and orientation directly generate aerodynamic forces and moments. The velocity vector and acceleration of the wing aerodynamic center ac are given as

$$_w\mathbf{v}_{ac/I} = R_{b \to w}\left(_b\mathbf{v}_{cg} + _b\boldsymbol{\omega}_{b/I} \times _b\mathbf{r}_{o/cg} \right) + _w\dot{\mathbf{r}}_{ac/o} + _w\boldsymbol{\omega}_{w/I} \times _w\mathbf{r}_{ac/o} \tag{7}$$

$$_b\mathbf{a}_{ac/I} = _b\mathbf{a}_{cg} + _b\boldsymbol{\omega}_{b/I} \times _b\mathbf{v}_{cg} + _b\dot{\boldsymbol{\omega}}_{b/I} \times _b\mathbf{r}_{o/cg} + _b\boldsymbol{\omega}_{b/I} \times _b\boldsymbol{\omega}_{b/I} \times _b\mathbf{r}_{o/cg}$$
$$+ R_{w \to b}\left(_w\mathbf{a}_{ac/o} + 2\,_w\boldsymbol{\omega}_{w/I} \times _w\mathbf{v}_{ac/o} + _w\dot{\boldsymbol{\omega}}_{w/I} \times _w\mathbf{r}_{ac/o}\,_w + _w\boldsymbol{\omega}_{w/I} \times _w\boldsymbol{\omega}_{w/I} \times _w\mathbf{r}_{ac/o} \right) \tag{8}$$

As indicated in Fig. 8, the aerodynamic center of the wing is the coordinate on the wing that is 25% chord from the leading edge and at the spanwise location of the center of the second

moment of wing area (approximately $0.55R$ according to Ellington [88]). An equivalent expression can be derived for the wing's center of gravity *wg*. Detailed expressions for the angular rates, accelerations, and rotation matrices are provided in our earlier work [25].

To simulate free flight, the wing motion with respect to the wing root is prescribed by the control inputs (i.e. wing kinematic parameters), while the body motion is simultaneously applied to the wing root. Therefore, the motion of the wing with respect to the air is the superposition of these two motions. The three-dimensional flapping is converted to a two-dimensional plunge motion. The arc length of the second moment of wing area is set equal to the plunge amplitude $h_a = ZR$. The equations of motion are integrated at every time step. Therefore, in free flight, the
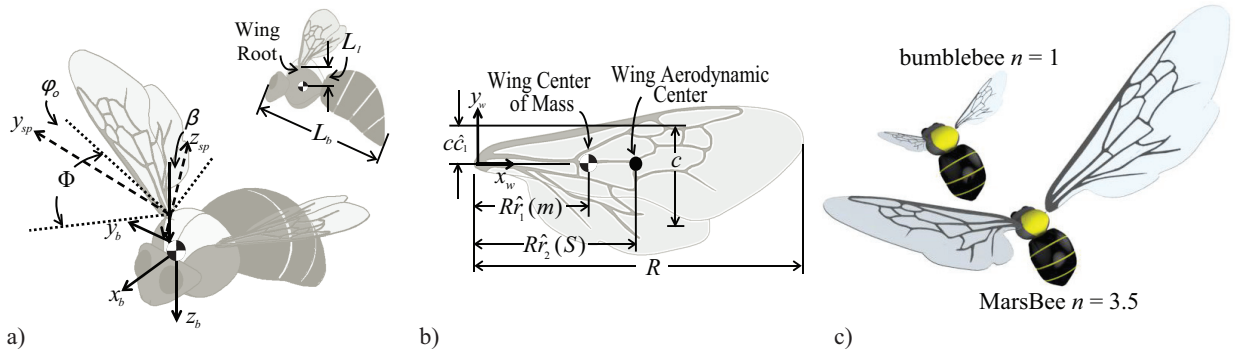
Figure 8. Schematic illustration of the key parameters for a) the body and b) the wing for c) a bumblebee (*n*=1) and a Marsbee with enlarged wing area (*n*=3.5). The wing parameters are determined by considering the wing to be a composite of the fore- and hindwings, as calculated by Ellington [88].

motion at each time step is a result of both the dictated wing kinematics and the body's free response.

4.2.4 Equations of Motion and Determining Equilibrium

With the mass of the wings included, the force and moment balance of the vehicle results in lengthy expressions, which are detailed in our previous work [25] and summarized here as

$$_b\dot{\mathbf{v}}_b = {}_b\mathbf{g} - {}_b\tilde{\omega}_b\,{}_b\mathbf{v}_b + \frac{1}{m_{body}}\sum_{j=1}^{\#wings}\left({}_b\mathbf{F}_{Aero,w} + {}_b\mathbf{F}_{Iner,w}\right)_j \tag{9}$$

$$_b\dot{\omega}_b = \frac{1}{{}_b\mathbf{I}_b}\sum_{j=1}^{\#wings}\begin{bmatrix} R_{w,j\to b}\left({}_w\mathbf{M}_{Aero,w,j} + {}_w\tilde{\mathbf{r}}_{ac/o}\,{}_w\mathbf{F}_{Aero,w,j}\right) \\ + {}_b\tilde{\mathbf{r}}_{o/cg,j}R_{w,j\to b}\left({}_w\mathbf{F}_{Aero,w,j} + m_{w,j}\,{}_w\mathbf{g}\right) \end{bmatrix} - {}_b\tilde{\omega}_b\,{}_b\mathbf{I}_b\,{}_b\omega_b \tag{10}$$

Here, the tilde over a vector quantity denotes a cross product and an over-dot represents the time derivative. $\mathbf{F}_{Aero,w}$ and $\mathbf{M}_{Aero,w}$ represent the aerodynamic contribution of the wing to forces and moments, respectively. In addition, $\mathbf{g}$ is the gravitational acceleration, m_{body} is the mass of the body, and I_b is the body inertia. Inertial properties of the bumblebee and other morphological

21

parameters are reported by Sun and Xiong [83].

The system is tracked in state space form with a state vector

$$\mathbf{x} = \begin{bmatrix} u & w & q & {}_I x_{cg} & {}_I z_{cg} & \theta \end{bmatrix}^T \tag{11}$$

where it is restricted to motion in the *x-z* plane. In order to find the trimmed state at hover, we express Eqs. (9) and (10) to highlight their dependence on the states and the control inputs as

$$\dot{\mathbf{x}} = A\mathbf{x} + B\mathbf{u}, \tag{12}$$

where the elements of the system matrix, *A*, and the control matrix, *B*, are themselves nonlinear functions of the states and control inputs. We construct the *A* matrix numerically by perturbing each degree of freedom and using a central difference approximation to compare the system response with and without a perturbation. Each disturbance is modeled by moving the wing root with a prescribed motion that corresponds to the desired disturbance for three flapping cycles. During this time, the fluid's response to both the prescribed motion and flapping motion is computed and the surrounding wake is allowed to develop fully. The *B* matrix is obtained by perturbing each control in a similar fashion and determining its effect on the average system response.

In order to achieve hovering trim, we require $\dot{\mathbf{x}}_{ave}$=mean($[\dot{u} \; \dot{w} \; \dot{q} \; u \; w \; q]^T$)=**0**, where the mean operator denotes the cycle averaged value. We utilize the trim method described by Badrya et al. [82] and further detailed in our previous work [28] to find the necessary control inputs, i.e. Z, ζ_o, and β, and initial conditions, u_0, w_0, q_0, and θ_0 that place the system in equilibrium. Convergence is set such that $\| \dot{\mathbf{x}}_{ave} \| < 1 \times 10^{-2}$ where the rate vector contains both accelerations (m/s^2) and velocities (m/s).

The detailed description of the free flight simulator and trim calculator as well as validation cases at fruit fly scales can be found in our previous work [25,67]. While we are able to validate our numerical free flight simulator against experimental results from flapping wing flyers on earth, we are not able to do the same for the Martian conditions. This is due to the fact that presently there is no physical experimental data for flapping wings in Martian atmospheric conditions. In Section 5.3, we present force measurements of bioinspired Marsbee prototype wings in Martian density conditions to report a preliminary validation data.

4.2.5   Aerodynamic Performance Metrics

Operating in remote environments such as Mars dictates that power considerations are critical to vehicle design success. A flapping wing is actuated by imparting angular motion to the wing. Therefore, the power required is the product of the moment required to actuate the wing and the angular velocity of the wing. The required moment is simply the difference between the

rate of change of angular momentum about the wing root (first term in Eq. (13)) and the aerodynamic moments (second term in equation (13)).

$$\mathbf{M}_{req} = \left({}_wI_{wo}\, {}_w\dot{\boldsymbol{\omega}}_w + {}_w\boldsymbol{\omega}_w \times {}_wI_{wo}\, {}_w\boldsymbol{\omega}_w + m_w\, {}_w\mathbf{r}_{wg/o} \times {}_w\mathbf{a}_o \right) - \left({}_w\mathbf{M}_{Aero,w} + {}_w\mathbf{r}_{ac/o} \times {}_w\mathbf{F}_{Aero,w} \right) \tag{13}$$

Because the angular velocity components of the wing contain body rates the body motion affects the required wing power. At each simulation time step, the components of the moment are multiplied by the corresponding components of the angular velocity of the wing with respect to the body as

$$\begin{aligned} P_{pitch} &= {}_wM_{req,x}\, {}_w\dot{\alpha} \\ P_{flap} &= {}_{sp}M_{req,y}\, {}_{sp}\dot{\zeta}, \end{aligned} \tag{14}$$

resulting in a time-history of power required. Note that this returns both positive and negative values. When P_{pitch} or P_{flap} is positive, power is required in order to achieve the desired wing motion. Because the atmosphere is so thin, and inertia dominates the power requirements, positive power typically occurs in portions of the stroke where the wing must be accelerated. Negative power typically occurs in the portions of the stroke where the wing decelerates. Many studies simply neglect negative power in their calculations [81,89,90], assuming that power is not expended during these portions of the stroke. We use the term positive power P_{pos} = mean($\forall P(t) > 0$) to refer to this definition. We report the validation of the power calculations for fruit fly motions and bumblebee motions [25,67].

Another way of treating power that we consider in this study is simply to directly average the negative and positive portions of the power required, P_{ave}=mean($P(t)$). This method assumes that the system can perfectly store the energy associated with negative power and fully utilize it in the parts of the stroke that require positive power. This method of calculating power provides an assessment of the minimum possible power required to fly, assuming a spring or other energy storage device is incorporated into the system to offset the large power consumption [90–92].

4.3   Zeroth-Order Method for Bioinspired Mars Flight

To achieve hover on Mars, in addition to scaling up the wing, the flapping wing motion must be adjusted to offset the reduced density ($\rho_{mars} \approx 0.013\rho_{earth}$) and reduced gravity ($g_{mars} \approx 0.38g_{earth}$). In this section, we show in detail how dynamic similarity can be achieved. A generalized method is presented in Section 4.3.2.

Equation (1) can be rewritten in terms of the reference velocity $U = 2\pi f Z r_2$, where f is the sinusoidal flapping frequency in Hz, Z is the half peak-to-peak flapping amplitude in radians, and R is the span of a single wing in meters (Fig. 8). This substitution results in

23

$$L = \frac{1}{2}\rho_{mars}(2\pi f Z r_2)^2 S C_L \tag{15}$$

Equation (15) demonstrates that scaling the flapping frequency f, flapping amplitude Z, or wing size R and S can increase the lift.

4.3.1 Example – Bumblebee Inspired Marsbee Solution

We begin by quantifying the impacts that the reference wing velocity $U \sim fZ$ and the wing area S have on the resulting lift L. This can be expressed by introducing scaling parameter n for wing scaling, m for frequency scaling, and p for stroke amplitude scaling into Eq. (15), resulting in

$$L \sim f^2 n^2 R^3 c \Rightarrow L \sim (p^2 m^2 n^4) f_0^2 n_0^2 Z_0^3 c_0 \tag{16}$$

where wing length $R=nR_0$, mean chord $c=nc_0$, stroke frequency $f=mf_0$, and stroke amplitude $Z=pZ_0$. Equation (16) demonstrates that the most efficient way of achieving lift is by increasing the wing size, as done in this study, since L scales with n^4.

More importantly, the lift coefficient C_L is a function of four dimensionless parameters that are subject to change in this study while operating on Mars with enlarged wings. Specifically we see that $C_L=C_L(Re,M,k,\alpha)$ in 2D [10,29]. The aspect ratio is included in the generalized zeroth-order model (Section 4.3.2).

We seek to preserve dynamic similarity between flapping on Mars and on Earth to be reasonably assured that the flapping wings will experience the high C_L produced by insects. Equations (15) and (16) and Table 1 show that determining a dynamically similar hover solution is not trivial. The first constraint that must be considered is the effect of the flapping amplitude on the reduced frequency. Since AR is unchanged in 2D, the flapping amplitude Z must remain similar to the biological bumblebee value in order to maintain an appropriate value for reduced frequency k in hover. It can be seen that Re is more sensitive to an increase in the wing size n as opposed to f or Z. Specifically, Re scales with n^2 since it is a product of both wing length R and chord length c. This would seem to suggest that wing scaling could quickly result in a Reynolds number that is no longer bioinspired. However, recall that Re also scales directly with the gas density ρ, which is significantly reduced in the case of Mars. As a result, Re can sustain a significant increase in n while maintaining a bioinspired value.

As it turns out, the most influential driver of maintaining a dynamically similar solution is the wing tip Mach number. M scales equally with flapping frequency, amplitude, and wing size. However, refer back to Eq. (16) which demonstrates that frequency would need to be scaled by a factor of m^2 to achieve the same amount of lift obtained with scaling the wing size by a factor of n^4. Consequentially, if flapping frequency was chosen as the parameter to scale in order to produce the required lift, it would result in a Mach number that exceeds the typical range of

insects. This means that the most efficient method of achieving lift and maintaining dynamic similarity is by scaling of the wing. This makes sense physically since scaling the wing size increases both the planform area S and the reference velocity (which affects the dynamic pressure due to a larger span R), both of which contribute to a higher lift (Eq. (15)). This is contrasted to scaling the frequency and flapping amplitude, which can only provide a higher reference velocity if they are increased.

Simply increasing the flapping frequency in Eq. (16) would not be a sufficient method for achieving lift on Mars. Specifically, the flapping frequency of a bumblebee would need to increase by a factor of 6 to around 990 Hz to offset the lower Mars density and gravity. Although the Reynolds number and reduced frequency remain in the insect flight regime, the wing tip Mach number increases to around 0.3. At this Mach number, compressibility effects can begin to become significant [93]. Also, it is unknown whether or not unsteady insect flight mechanisms can produce high lift coefficients at this value for M, which is beyond the scope of the present study.

Furthermore, as this study will eventually extend beyond hovering flight, it is important to also consider the relevant dimensionless parameters in forward flight. Both the forward flight reduced frequency and the Strouhal number scale directly with the flapping frequency f. If a large frequency is required to achieve hover, then it is likely that these parameters could surpass their respective range typical of insect flight on earth, resulting in a solution that is not dynamically similar.

4.3.2   Generalized Zeroth-order Method

To generate an informed solution for dynamically similar motion on Mars given a vehicle mass, we provide a method that combines the lift-weight balance equation (Eq. 1) with the typical ranges of relevant dimensionless parameters that govern the high lift coefficients of unsteady insect motion in Table 1 [94].

Obtaining a dynamically similar solution is non-trivial as there are multiple dimensionless parameters to consider in the design of a flapping wing robot. Also, a small change in one parameter can quickly drive another parameter out of the insect-inspired regime. The proposed zeroth-order method will result in dynamically similar solutions for the flapping frequency f and amplitude Z, as well as the wing span R and mean chord c required to balance the weight of the desired vehicle W on Mars.

The largest constraint imposed by dynamically similar motion on Mars is the effect of the Mach number M on the reference velocity U_{ref}. The reduced speed of sound on Mars ($a_{Mars}=0.72a_{Earth}$) results in more rapidly approaching the speed of sound for a given velocity, as compared to that same velocity on Earth. We can use the information that insects typically operate at $M<0.1$, such that $M_{max}=0.1$, to determine the maximum of the reference velocity, while maintaining an appropriate Mach number. The maximum wing velocity is defined as the velocity at the wing tip and is constrained by the Mach number and speed of sound as

$$U_{tip} = 2\pi f ZR = M_{max} a_{Mars}. \tag{17}$$

Since the reference velocity is taken at the r_2 location, we can express U_{ref} in terms of U_{tip} as

$$U_{ref} = \hat{r}_2 U_{tip}. \tag{18}$$

The wing area of each wing required to sustain the vehicle with weight W, while operating at a flapping speed of U_{ref}, can be determined by rearranging Eq. (1) in terms of S, such that

$$S = \frac{W}{\rho U_{ref}^2 C_L} \tag{19}$$

As a result, the wing span R and mean chord c can be expressed in terms of the desired wing aspect ratio AR as

$$R = \sqrt{S \cdot AR} \quad \text{and} \quad c = R/(AR). \tag{20}$$

Expressing R and c in this manner gives us the advantage of solving for the wing morphological and kinematic parameters explicitly in terms of two dimensionless parameters, M and AR. As such, we can guarantee that the resulting solution is dynamically and geometrically similar with respect to two (M and AR) of the five relevant dimensionless parameters (Table 1). To factor in a third dimensionless parameter to guide our solution, we express the flapping amplitude Z in terms of the reduced frequency in hover k as

$$Z = \frac{1}{2k \cdot AR}. \tag{21}$$

Lastly, the flapping frequency f can be expressed in terms of the reference velocity (Eq. 18), wing span (Eq. 20), and flapping amplitude (Eq. 21) as

$$f = \frac{U_{ref}}{2\pi ZR\hat{r}_2}, \tag{22}$$

which ensures that the flapping frequency will result in dynamically similar motion with respect to M, AR, and k.

We have obtained a family of insect-inspired robots that can achieve lift across a broad range of vehicle masses: 1 – 25 g (Fig. 9). For example, the parameters for 5 g and 25 g Marsbees are shown in Table 4. For the 5 gram Marsbee, a wing with an aspect ratio of 3, flapping at 35 Hz with an amplitude of 47 deg can generate sufficient lift for hover (Fig. 9a,b).

In this project, the mass of these zeroth-order Marsbee solutions correspond to two existing terrestrial flapping wing vehicles. The first reference vehicle, the AeroVironment Nano

Hummingbird [26] has a wing span of 16 cm and a mass of 19 g. It was able to hover and fly forward at 6.7 m/s for 10 minutes. The second reference vehicle, the hummingbird-inspired Micro-Air Vehicle (MAV) [27,28], was developed by our Japanese collaborators. This vehicle weighs approximately 8 g. This MAV can currently fly controlled for 5 to 10 minutes. After researching the current state of battery and sensor technology, we believe a 10 g vehicle is currently realizable. Advances in miniaturization and energy storage, as well as multi-functional structures, will enable a future vehicle in the 5 g range.

Table 4. Bioinspired Marsbee solutions exist that maintain the relevant dimensionless parameters governing the high lift coefficient producing motion of insects on Earth.

dimensionless parameter	definition	insect regime	5 g Marsbee	25 g Marsbee
Reynolds number, Re	$\rho_{mars} U c / \mu_{mars}$	$O(10^2\text{-}10^4)$ [10]	480	1100
Mach number, M	U / a_{mars}	< 0.1	0.1	0.1
reduced frequency, k	$\pi f c / U$	$0.2 - 0.4$ [10,29]	0.2	0.2
aspect ratio, AR	R / c	$2 - 9$ [10]	3	3
angle of attack, AoA	AoA	$\sim 45°$	45°	45°
average lift coef., C_L	$L / (\frac{1}{2}\rho U^2 S)$	$O(10^0)$	1.8	2.1
dynamically similar?			yes	yes

Note that only three of the five dimensionless parameters are used in the above approach for determining *c, R, f,* and Z. This is because the angle of attack *AoA* is governed by the instantaneous pitch angle α (see Section 4.2.1) and is therefore independent from the wing geometry or flapping motion. Additionally, the Reynolds number *Re* is left to vary as a function of the previously defined wing parameters. This is because *Re* is directly proportional to the atmospheric density ρ (see Table 1), which is extremely low on Mars. As a result, *Re* is generally low for a given combination of kinematic and morphological parameters on Mars and will therefore remain in the desired insect-inspired regime.
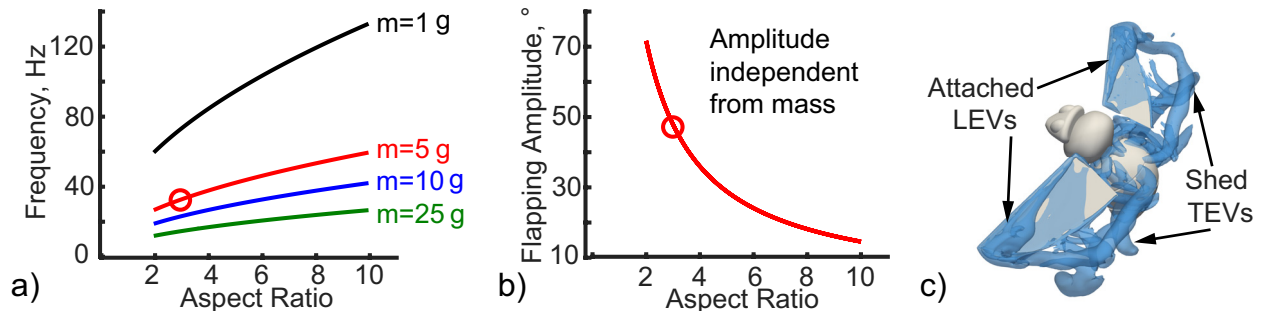
Figure 9. (a,b) Zeroth-order solutions for dynamically similar flapping wing motions on Mars for a broad range of vehicle masses. (c) bioinspired flight solution from a well-validated 3D Navier-Stokes solver for a 5 g flapping wing robot, corresponding to the highlighted points on solution curves (a,b).

4.4   Bioinspired Hover Flight on Mars - 2D Aerodynamics Solution

In order to justify the need to scale up the wings, we first test whether a standard bumblebee could fly on Mars. Using the flight simulator described in Section 4.2, but with gravitational and atmospheric parameters that correspond to the Martian atmosphere, we solve for the control inputs that permit hovering flight on Mars. Per Table 4, flight for a standard bumblebee (i.e. $n=1$) in a Martian atmosphere requires a flapping amplitude of Z=366.3°. When the half peak-to-peak flapping amplitude exceeds 90°, the left and right wings touch each other, which is not physically permissible. Therefore, the wing kinematics and morphology of a standard bumblebee cannot generate sufficient lift on Mars because the Martian atmosphere is too thin.
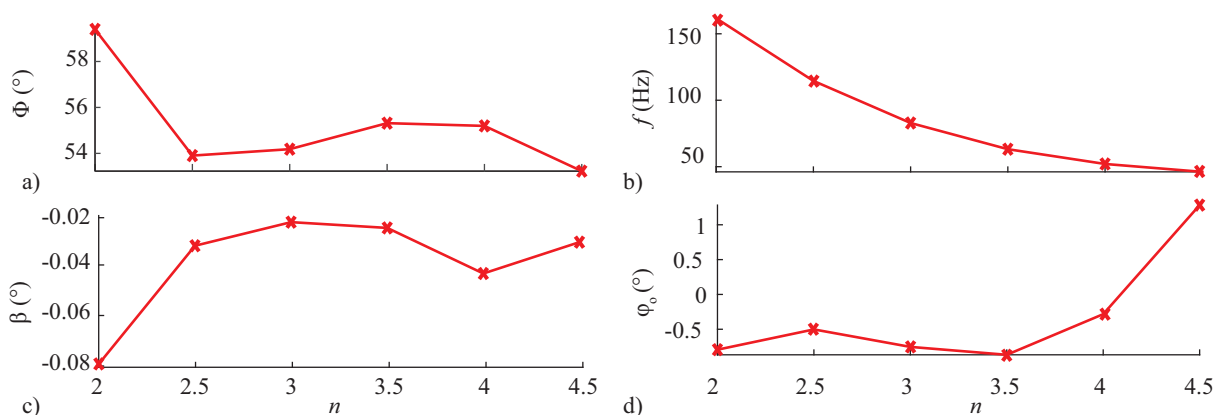
Figure 10. Control parameters required to hover on Mars for various wing sizes for a) the flapping amplitude, b) flapping frequency, c) stroke plane angle, and d) offset angle.

Therefore, our results show that the natural bumblebee cannot sustain its weight in hover in the rarefied atmosphere on Mars. However, if we consider a Marsbee, a hybrid bumblebee with larger wings that are scaled in all dimensions by a factor of n, ranging from 2 to 4.5, the resulting lift is sufficiently high to sustain its weight. This sufficient lift is achieved primarily by the enlarged wings which have four to twenty times the planform area of the Earth bumblebee wings.

4.4.1   Small Marsbee Solution

Figure 10 shows the control parameters that yield hover equilibrium on Mars for a bumblebee-sized Marsbee. It can be seen that the resulting flapping amplitudes remain in a relatively small range (Fig. 10a). This is by design, resulting in a relatively consistent value for the reduced frequency in hover $k=1/(ZAR)$. Recall that by consistently scaling up the chord and span by n, the aspect ratio AR is kept the same. Thus, the resulting k for the Marsbees ranges from 0.315 to 0.323 which is within the insect flight regime. The Reynolds number remains of the order of $O(10^2)$ by reducing the flapping frequency as the wing size increases (Fig. 10b). The stroke plane angle β and the flapping offset angle ζ_o are also provided, but their variation for different wing sizes is small. Although the wing's velocity is larger than on Earth and the speed

of sound on Mars is approximately 72% of the speed of sound on Earth [8], the Mach number remains less than 0.09, indicating that the flow is incompressible and within the insect flight regime.

Table 5. A summary of physical and flapping parameters for bumblebee flight on Earth and Mars and Mars MAV flight on Mars. Results are based on our coupled NS-flight dynamics code. Note that bumblebee flight on Mars in characterized by an unphysical flapping amplitude and a reduced frequency that results in a non-dynamically similar solution. However, the dimensionless parameters for both Mars MAVs result in dynamically similar solutions, where n=3.5 requires the least amount of power.

	bumblebee on Earth	bumblebee on Mars	Mars MAV on Mars, *n*=2.5	Mars MAV on Mars, *n*=3.5
wing size factor	1	1	2.5	3.5
atmospheric density [kg/m^3]	1.225	1.55×10^{-2}	1.55×10^{-2}	1.55×10^{-2}
gravitational acceleration [m/s^2]	9.81	3.72	3.72	3.72
viscosity coefficient [kg/(ms)]	1.8×10^{-5}	1.5×10^{-5}	1.5×10^{-5}	1.5×10^{-5}
body mass [kg]	1.75×10^{-4}	1.75×10^{-4}	1.75×10^{-4}	1.75×10^{-4}
total wing area [m^2]	1.06×10^{-4}	1.06×10^{-4}	6.60×10^{-4}	1.29×10^{-3}
mass of wings [kg]	9.10×10^{-7}	9.10×10^{-7}	1.42×10^{-5}	3.90×10^{-5}
wing mass / body mass	0.52%	0.52%	8.13%	22.3%
total mass [kg]	1.75×10^{-4}	1.75×10^{-4}	1.88×10^{-4}	2.13×10^{-4}
total weight [mN]	1.72	0.652	0.702	0.794
flapping amplitude [deg]	41.6[*]	366	53.9	55.3
flapping frequency [Hz]	155	155	114	63.1
Reynolds number	1439	340.6	127	141
wing tip Mach number	0.028	0.33	0.05	0.03
aspect ratio	3.3	3.3	3.3	3.3
angle of attack	50°	50°	50°	50°
reduced frequency	0.4054	0.048	0.323	0.315
power required [W]	0.012	0.19	0.20	0.19
specific power required [W/kg]	68.6	1090	1090	901
flap amplitude less than 90°?	yes	no	yes	yes

* flapping amplitude for bumblebee on earth using advanced rotation

Table 5 also shows the main parameters of realizable flapping motions for trimmed, hovering flight on Mars for a family of small, bumblebee-sized Marsbees consisting of enlarged wings on a bee's body (Fig. 10c) with lift equal to total weight. When the chord and span of a standard Earth bumblebee wing are increased by factors of *n*=2.5 and *n*=3.5, i.e. the area is

increased by corresponding factors of 6.25 and 12.25, sufficient lift can be generated that can offset the increased total weight. Despite the cubic increase in the wing weight, the total system weight increases only by 8% and 22%, respectively. This is again a benefit of the nominal bumblebee's small wing-to-body mass ratio. Note that in Table 5, the bumblebee on earth simulation was performed using the same kinematics used in the small Marsbee simulations (Section 4.2.1). As a result of maintaining consistent kinematics across simulations, namely the use of advanced rotation, the flapping amplitude for the bumblebee on earth is lower than typically reported in literature. This is expected, as advanced rotation is reported to produce higher lift compared to the symmetric pitching typical of biological flapping motion [61,82]. This reasoning also applies to the slight discrepancies between the dimensionless parameters presented in Tables 3 and 5 for the bumblebee on earth.

Although we use the bumblebee parameters as a starting point in this study, we seek a bioinspired Mars flight design that falls within the insect flight regime, not necessarily constrained by the bumblebee regime. The larger wings of the bioinspired Marsbee allows hover in the low density environment on Mars. However, the penalty associated with using such large wings is clearly seen in the power required to actuate them. From Table 5, operating on Mars requires over 13 times the power to fly on Earth when considering the case where the wings are scaled by a factor of n=3.5. Because of the ultra-low density in the Martian atmosphere, the resulting Reynolds number reduces to $Re=O(10^2)$, which is an order of magnitude lower than the Earth bumblebee Reynolds number. The higher power required for the Marsbee compared to the bumblebee on Earth suggests that the performance may be further improved. Moreover, the reduced performance may be ascribed to the fact that the Mars flight vehicle operates at a reduced Reynolds number. Still, the resulting Reynolds number is within the insect flight regime and the resulting lift coefficient is sufficiently high such that the bioinspired Mars flight vehicle is able to sustain its own weight on Mars. The power required and an energy harvesting method to reduce power substantially is further discussed in more detail in Section 4.6.3.

4.4.2   Bioinspired Unsteady Lift Enhancement Mechanisms on Mars – 2D

Figure 11 shows the lift histories for various wing sizes subject to the constraint of operating in trim on Mars. Each trace describes the average lift that is necessary to balance the weight on Mars for the wing size factor of n=1 (bumblebee on Mars) and n=2.5, 3.5 (small Marsbees on Mars). The associated drag and wing kinematics are included in Fig. 11 as well. This figure also depicts the unsteady lift generation mechanisms that yield much higher lift coefficients than conventional airplane or helicopter designs at low Reynolds numbers [95]. Insects use unsteady lift production mechanisms, including the well-known mechanisms of delayed stall, rotational lift, added mass forces, and wing-wake interaction (or wake-capture) [10,60–63] to fly. These unsteady lift generation mechanisms are the reason that the dynamically similar flapping wings can produce sufficient lift despite the low-Reynolds environment on Mars.

The lift time histories are qualitatively similar for n=2.5 and 3.5 with the averaged lift

being higher for $n=3.5$ because the total weight is greater in trim. To simplify the discussion, we only compare the lift production mechanisms and vortex dynamics between $n=1$ and 3.5 in this section. The corresponding vorticity contours are illustrated in Fig. 12 for $n=1$ and 3.5. The wing is flapping from left to right with advanced rotation. The z-component of vorticity is positive into the page and it is normalized by U/c. The vorticity contours clearly identify the location and direction of the vortical structures relative to the wing. The leading-edge vortex generated in the current stroke is denoted by LEV_1; the LEV shed in the previous stroke is labeled as LEV_0, and so on. Trailing-edge vortices (TEVs) follow the same convention.

   The first high-lift mechanism is wake-capture, which causes the large lift increment for $n=3.5$ at the stroke ends $\tau=0$ and $\tau=0.5$. During this phase of the stroke, the wing encounters the LEV_0 (figure 12b at $\tau=0$) that was shed during the previous half-stroke, enabling the wing to recover energy from the flow [86,87]. In the case of $n=1$, however, the vortex structures in the immediate vicinity of the wing are dominated by the TEV_0 shed during wing rotation, which imparts downwash on the wing and delays lift production from wing-wake interaction with LEV_0 until $\tau=0$ to 0.0625. This is reflected in Fig. 11a, where no lift increment is seen at $\tau=0$ or $\tau=0.5$ for $n=1$.

   The second region of large lift generation for $n=3.5$ occurs from $\tau=0.125$ to 0.35 in the first half-stroke and from $\tau=0.625$ to 0.85 in the second half-stroke (Fig. 11a). The lift in this region results from the stable LEV_1 that forms during the translational phase of the stroke, hence it is termed translational lift [61]. The LEV_1, which can be seen at $\tau=0.25$ and 0.375 for $n=3.5$ in Fig. 12b, significantly reduces the pressure behind the wing and increases the lift.
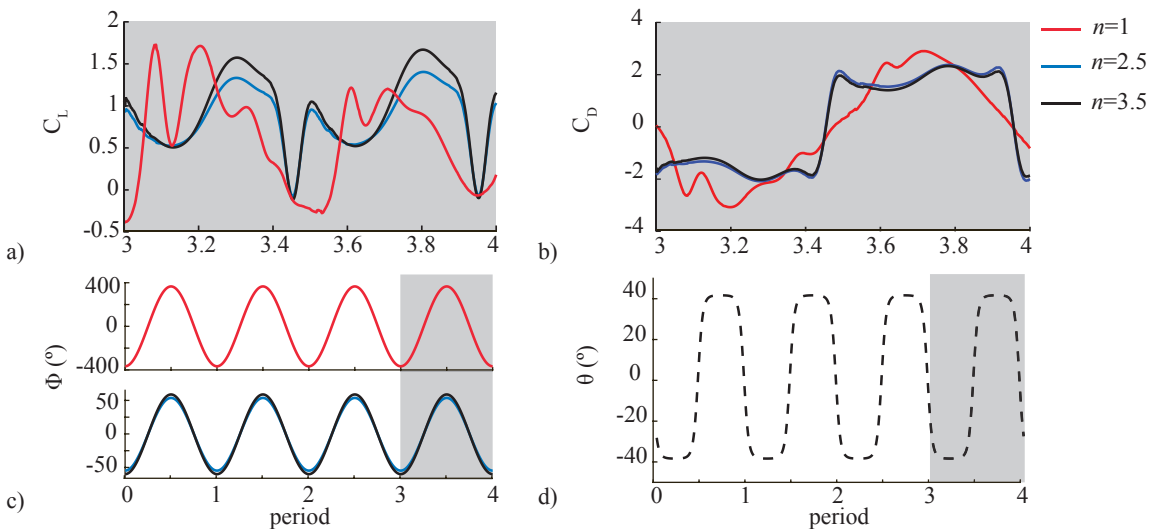
Figure 11. a) Lift and b) drag produced by a bee on Mars ($n=1$) and two bumblee-sized Marsbees ($n=2.5$ and $n=3.5$) during the fourth and final flapping period. Corresponding c) flapping and d) pitching motions, where the flapping amplitude varies as a function of n while the pitching amplitude is the same for all values of n.
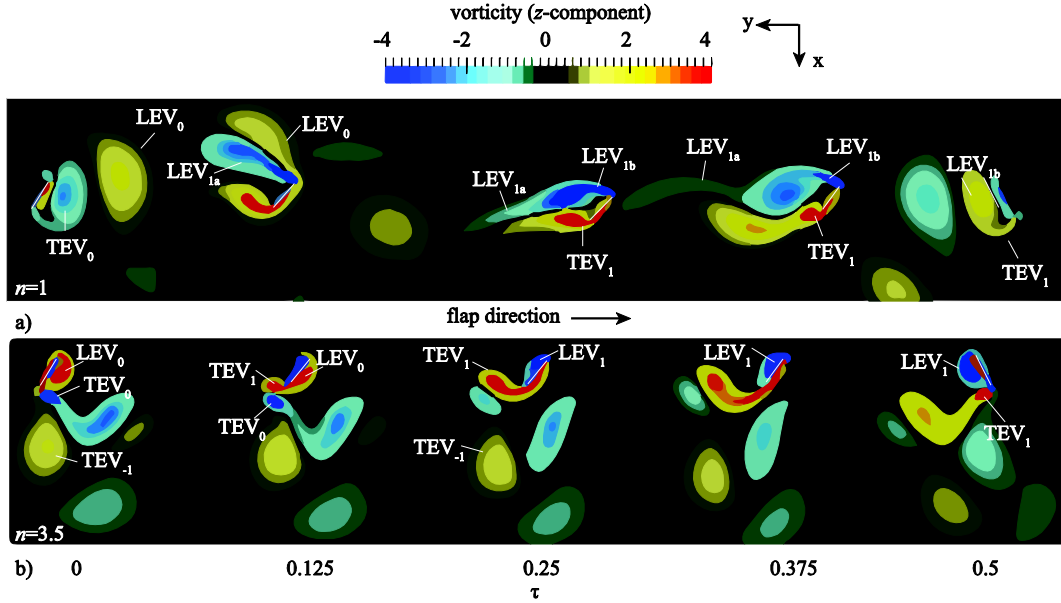
Figure 12. Unsteady vortex generation for a) $n=1$ where f=155 Hz, Z=366.3° and b) $n=3.5$ where f=63.1 Hz and Z=55.3°. The unphysically large stroke amplitude in conjunction with the bumblebee's natural flapping frequency results in a) flow structures and a lift history which are not exhibited by insects. However, the flow structures for the case of b) $n=3.5$ are similar to those for typical flapping flyers. Vorticity is normalized with U/c.

On the other hand, in the case of $n=1$, two separate LEVs form in each half-stroke with a noticeable shedding event that results in the abrupt loss of lift immediately preceding and following $\tau=0.25$ in Fig. 11a. The first LEV_{1a} that forms can be seen at $\tau=0.125$ (Fig. 12a) associated with the second lift peak (figure 11a). The timing of this lift peak is earlier than the case of $n=3.5$ because of the unphysically large flapping amplitude, yielding a relatively faster flapping motion. It is destabilized by interference from LEV_0 and by the rapid growth of TEV_1, leading to the separation of LEV_{1a} around $\tau=0.2$. A new LEV_{1b} can be seen forming at $\tau=0.25$, and it produces the third lift peak at $\tau=0.3$ in Fig. 12a. This process is repeated in the second half stroke. Thus, for the $n=1$ case, the translational force mechanism is the source of both peaks that are seen in Fig. 11a in each half stroke, with delayed contributions from wake-capture generating the first peak. The strength and size of the TEV_0 is much larger for $n=1$, which changes the overall flow field and prevents the LEV_0 from interacting with the wing as described previously for the bioinspired Mars MAV configurations ($n=3.5$).

The lift time history and the vortex dynamics for the bioinspired Marsbee configuration at $n=3.5$ resemble the insect flapping aerodynamics for hover with both wake capture and delayed stall lift peaks [10]. However, when $n=1$, wake capture is delayed by the unphysically large flapping amplitude, and the delayed stall mechanism is characterized by two noticeable shedding events of the LEV. This discussion demonstrates that a bioinspired dynamic similar solution is promising and important to realize flying on Mars by flapping motion.

32

4.5   Bioinspired Hover Flight on Mars - 3D Aerodynamics Solution

To test the question that the zeroth-order model produce solutions that are valid in 3D flow fields, we compute 3D Navier-Stokes equation solutions for the bioinspired Marsbees. We focus on the aspect ratio, which was neglected in the 2D aerodynamics analysis. Furthermore, we neglect the coupling to flight dynamics as the magnitude of the lift production and the presence of insect-scale, unsteady lift enhancement mechanisms are the main questions.

To systematically determine a solution for the kinematic and morphological parameters for a 5 g flapping wing robot with motion dynamically similar to the motion of insects on Earth, we begin with the zeroth-order approach described in Section 4.3. We use the zeroth-order results to define the input parameters into the NS solver. We then analyze the NS results to determine whether or not the zeroth-order method produces wing geometry and kinematics that generate sufficient lifting force to balance the weight of the vehicle in the Martian conditions.

4.5.1   Zeroth-order Solution

We apply the solution the procedure outlined in Section 4.3.2 to a 5 g vehicle to determine the morphological and kinematic parameters to supply to the NS solver. In order to find a solution, some assumptions must be made about the flight characteristics. First, since the average lift coefficient C_L can only be determined *a posteriori*, we must assume a value to solve Eq. (19) for the wing planform area S. Since insects are capable of producing lift coefficients in excess of 1 [10,96] and our previous study revealed that the average lift coefficient for symmetrically flapping 3D wings is near 1.5 [97], we use assume a value of C_L=1.5 in the zeroth-order method. The validity of this assumption will be verified once the NS solutions are obtained (Section 4.5.2).

Additionally, the reduced frequency in hover k governs the flap amplitude required to maintain dynamic similarity Eq. (21). In light of our previous results showing that increasing the flapping amplitude and reducing the flapping frequency to achieve a desired lift reduces the inertial flap power required (the dominant power component for flapping wing motion on Mars when an inertial spring is not considered) [98], we set k=0.2 such that it remains in the insect regime, while having the effect of increasing the flapping amplitude instead of the flapping frequency.

4.5.2   Hover Solution from 3D NS Solver

To achieve a hover solution on Mars, we provide the results from the zeroth-order model into the NS solver to determine the resulting lift force. As the aspect ratio is one of the main parameters driving the lift coefficient in bioinspired flight, we choose discrete values of AR=2, 4, and 6 to cover the aspect ratios in a range from fruit flies (AR=2.4 [99]) to bumblebees (AR=6.6 [100]). Many studies have investigated the effects of aspect ratio on the lift coefficient of flapping wings [101,102]. The goal is not to perform a parametric investigation of aspect ratio effects. Instead, we include various aspect ratios to demonstrate the ability of the zeroth-order model to properly inform the dynamically similar solutions of flapping wing vehicles with

varying dimensionless parameters (aspect ratio included). The results of the zeroth-order informed 3D NS simulations for a range of dimensionless parameters in the insect-inspired regime can be found in Table 4.

It is worth noting first in Table 4 that the lift coefficients from the NS solutions, generated for the Mars solutions are in excess of the assumed lift coefficient in the zeroth-order model (i.e. $C_L > 1.5$). This result is a clear confirmation that the zeroth-order method can be used as an appropriate tool to scale the bioinspired solutions for hovering flight on Mars. Since the lift force scales with C_L, any increase in the lift coefficient from the assumed value is an increase in the vehicle mass for the given wing geometry and kinematics.

The results for bioinspired flight on Mars in Table 4 are couched between representative bioinspired values at the upper and lower ends of the relevant nondimensional parameters. It is evident that all of the dimensionless parameters for the medium-size bioinspired flight vehicle on Mars are well within the typical values common to biological flapping wing flight. The Mars solutions appear to have dimensional and nondimensional parameters that lie close to those of a hummingbird, which is not surprising given the 5 g mass of the bioinspired flapping wing vehicles, similar to the 8 g mass of a hummingbird. However, the most noticeable differentiation between the Mars solutions and the representative solutions on Earth is the wing size required for sufficient lift on Mars, noted by the relatively large values of S compared to the biological flappers on Earth. Augmenting the low density on Mars with large wings is the same approach used in our previous study [67] and is built into the zeroth-order method to ensure appropriate lift generation along with dynamically similar motion. Additionally, the Reynolds number is nearly two orders of magnitude lower than hummingbirds and one order of magnitude lower than bumblebees, which is mostly due to the ultra-low density of the Martian atmosphere.

4.5.3 Bioinspired Unsteady Lift Enhancement Mechanisms on Mars – 3D

It is critical to understand the behavior of the aerodynamics that generate sufficient lift to hover in the ultra-low density Mars atmosphere. In fact, the zeroth-order method proposed in the present work hinges on the ability of dynamically similar motion to generate forces that benefit from the unsteady lift-enhancing mechanisms of insects on Earth. To test if this is the case, we simulate the motion resulting from the zeroth-order method for the 5 g with a pair of 15 by 4.8 cm wings, flapping at 35 Hz and analyze the resulting aerodynamic mechanisms present in the solutions, which can be found in Fig. 13.

It should first be noted that the full-cycle-averaged lift coefficients C_L (Fig. 13a) are sufficiently high to balance the weight of the vehicles in hover. Additionally, a constant C_L for $2 < AR < 4$, then a reducing C_L for $AR > 4$ is consistent with aspect ratio effects on C_L as described by other researchers [102]. Additionally, the C_L curve in Fig. 13a reveals lift peaks similar to those produced by insects on Earth. Each half-stroke is characterized by two dominant lift peaks near the beginning and end, which bookend the translational lift section in the middle of each half-stroke. These dominant lift peaks on the ends of each half-stroke are mainly due to the rotational lift mechanism due in part to the wing forcing the surrounding flow down and

generating a positive reaction force in the direction of lift. The translational lift section can be found between $0.15<t/T<0.35$ in Fig. 13a, during which the wing maintains a constant angle of attack of $\pm45°$ (Fig. 13b).

During the translational phase, a strong LEV remains attached until the mid-stroke, which is near the time when it sheds and the lift reduces significantly. Figure 13c contains snap shots of contour iso-surfaces of the Q-criterion which are indicative of regions of high vorticity in the flow. The presence and locations of these contour iso-surfaces can be correlated to unsteady lift enhancement mechanisms utilized by biological fliers. For instance, the attached LEV can be seen at $t/T=0.10$ and $t/T=0.25$ in Fig. 13c, in addition to the shed TEV at $t/T=0.25$. A break down and separation of the tip vortex can be seen during the rotational lift period at the end of the down stroke in Fig. 13c at $t/T=0.40$. Since the lift histories and cycle-averaged lift coefficients of

c) $t/T=0.05$ $t/T=0.10$ down stroke $t/T=0.25$ $t/T=0.40$
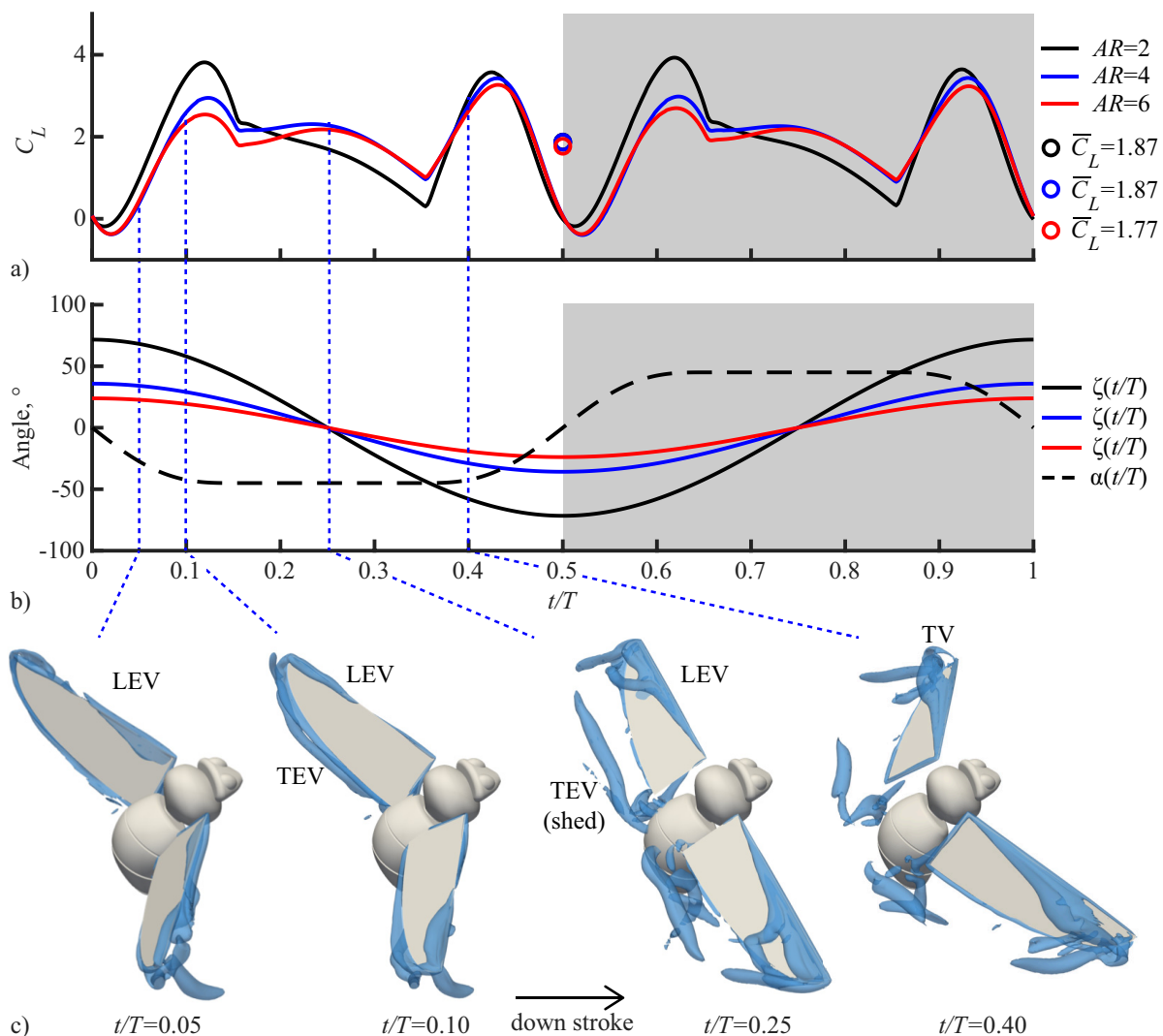
Figure 13. The resulting a) 3D NS lift coefficient and b) kinematics time history for the dynamically similar flapping wing motions generated by the zeroth-order method for 5 g flapping wing vehicles on Mars with various aspect ratio. c) Contour plots of the iso-surfaces of Q-criterion ($Q=15$) indicative of vorticity for $AR=4$.

AR=2 and 6 are similar to the lift histories of *AR*=4, it is assumed that they benefit from the same unsteady lift mechanisms seen in the case of *AR*=4.

4.6   Power and Payload Considerations

The time histories of flapping and pitching power required to hover on Mars are shown in Fig. 14 for various wing sizes corresponding to the 2D solutions shown in Section 4.4. The time history of the flap power resembles a sinusoidal profile. The peak flap power varies with *n*. On the other hand, the pitch power is zero during the midstroke, when the pitch angle is held constant as shown in Eq. (14). At the ends of the strokes, the wing rapidly rotates, leading to large peaks. Since both flapping and pitching power are functions of multiple variables (e.g. wing speed, lift and drag coefficients, and wing size), we do not see a monotonic trend in the amplitudes of the pitch power.
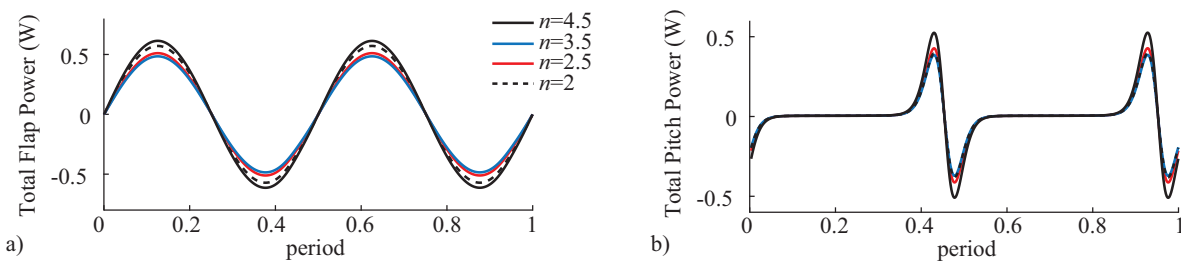
Figure 14. Time histories of the a) flap and b) pitch power for different wing sizes *n*. The curves show that there is not a direct monotonic scaling between the wing size *n* and the power amplitude for either flapping or pitching. This is because the flapping and pitching power are functions of multiple variables, such as wing speed, lift and drag coefficients, and wing size.

Additionally, both flapping and pitching power are less than zero for significant portions of the stroke. The flap and pitch power peaks are of approximately the same magnitude. However, the pitch power peaks are of much shorter duration.

Figure 15 shows the inertial and aerodynamic contributions to the required flap and pitch power. Most significantly, in both the flapping and pitching power, the inertial contribution to power is approximately two orders of magnitude larger than the aerodynamic contribution to power. The moment of inertia increases with scale factor by n^5, which significantly increases the inertial power. Also, the Martian air is so thin that the aerodynamic power is much lower than it is on Earth, all else being equal.

Figure 16 depicts the pitch, flap, and total positive power, P_{pos}, for various wing sizes. Additionally, the average power, which is averaged over one cycle, is presented. This is considered the ideal power because it assumes that all negative power can be stored and perfectly recovered, thus negating some, or all, of the positive power. In the Martian atmosphere, a bumblebee with nominal wings (*n*=1) would require approximately 0.19 W to achieve hover (Table 5), although we showed in Section 4.4.1 that a physically impossible flapping amplitude
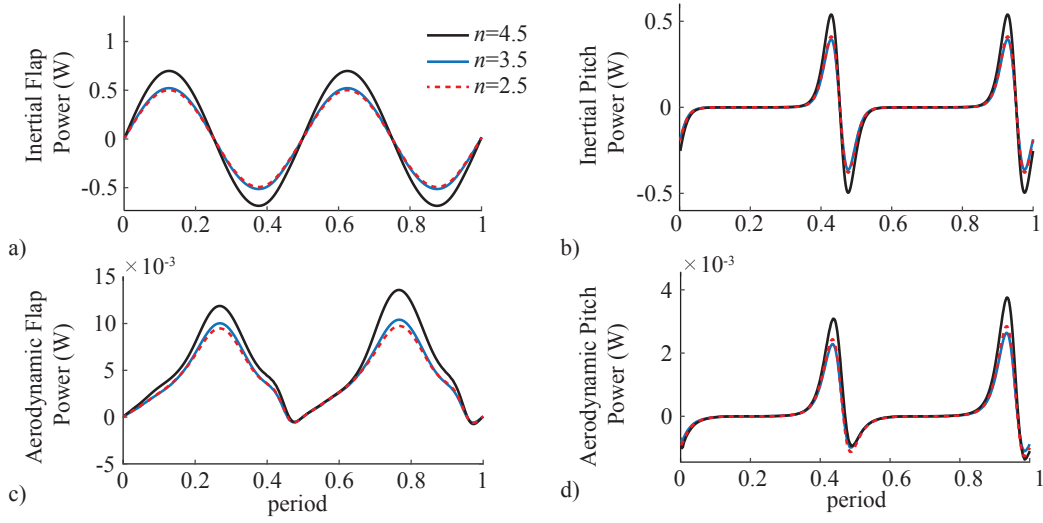
Figure 15. Power requirements for different wing sizes *n*=2.5, 3.5 and 4.5. a) Inertial flap power; b) Inertial pitch power; c) Aerodynamic flap power; d) Aerodynamic pitch power. The inertial power required is orders of magnitude larger than the resulting aerodynamic power for flapping wings on Mars. This is due to the ultra-low density of the atmosphere.

is required to do so. On the other hand, increasing the wing size by a factor of *n*=2.5 to 3.5 and reducing the flapping frequency will reduce the required power to approximately 0.17 W and 0.16 W respectively. Increasing the wing size further, however, causes an increase in the total power required. The specific power curve has a clear region where flight with minimum power is obtained between *n*=3 and *n*=4 for the given kinematics.

4.6.1 Inertial Cause of Power Required

The nonlinear trend in power with respect to a variation in the wing size *n* can be explained by considering the inertial contribution to the total power. As shown in Fig. 15, the inertial power is orders of magnitude greater than the aerodynamic power because of the ultra-low Martian density for both flap and pitch powers. As the wing size *n* varies, both the required flapping amplitude Z and flapping frequency *f* change to achieve hover equilibrium as shown in Fig. 10.

The inertial flap power for a pair of wings can be found by inserting Eq. (15) in Eq. (14), yielding

$$P_{\text{flap,inertial}} = \dot{\zeta} I_{yy} \ddot{\zeta} = 8\pi^3 I_{yy,w0} f^3 Z^2 n^5 \sin(4\pi ft) , \tag{23}$$

where the moment of inertia of the wing scales as $I_{yy}=I_{yy,0}n^5$ under a wing size variation *n*. The subscript 0 indicates the nominal wing size value.

On the other hand, the relationship between the flapping amplitude, frequency, and wing size, subject to the condition that the lift balances the weight, can be estimated from Eq. (24) as

37
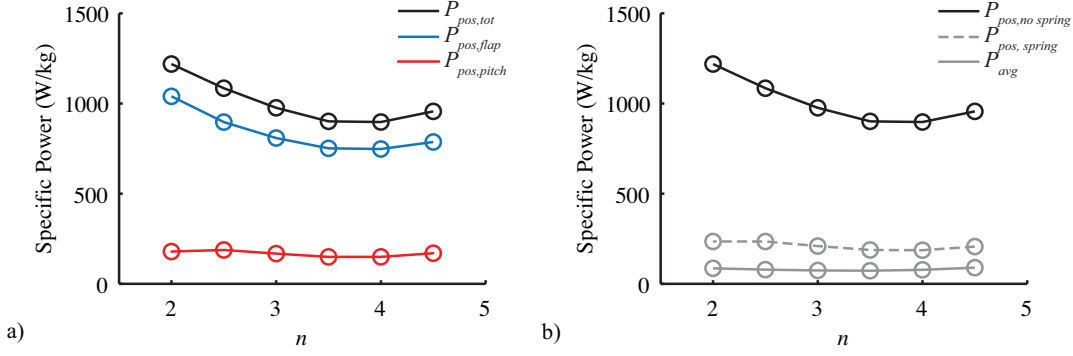
Figure 16. Specific power for different wing sizes *n* based on NS simulations, normalized by the total mass. a) Positive power for pitch, flap, and total power. b) Power comparison for positive power (with and without torsional springs) and the ideal case of average power, which assumes that all negative power can be stored and perfectly recovered. The power reduction with the torsional springs (see Section 4.6.3) is ~80% for each case. This is a direct result of the springs operating at their resonance frequency and thus negating the inertial flap power required. The resulting power for the torsional spring cases is the sum of the aerodynamic flapping power plus the aerodynamic and inertial pitching power. Note how the positive spring power curve approaches the ideal case of the average power and is slightly more than the total pitching power due to the aerodynamic flap power required.

$$f\mathrm{Z} = \frac{1}{n^2}\sqrt{\frac{mg}{4\pi^2 \hat{r}_2^2 \rho R_0^3 c_0 C_L}} \ , \tag{25}$$

where the wing area is $S=2Rc$, and wing length and mean chord vary with n as $R=R_0 n$, $c=c_0 n$, and, again, $U=2\pi f\mathrm{Z}\,\hat{r}^2 R$.

To dissect the influence of Z and f on $P_{\text{flap,inertial}}$, we first hold Z constant and adjust f to achieve equilibrium. Then we hold f constant and adjust Z. Since we consider the same wing shape, r^2 is also constant. Additionally, the change in the total weight is relatively small with respect to n as discussed before. Furthermore, our simulations indicate that the lift coefficient is close to $C_L=1$ for all cases. For simplicity, we define a parameter $\Gamma=(mg/4\pi^2 r^2 \rho R_0^3 c_0 C_L)^{1/2}$ that is held constant in the following analysis.

When Z is kept constant, the required flapping frequency becomes $f=\Gamma/\mathrm{Z}n^2$ from Eq. (25). Then Eq. (23) becomes

$$P_{\text{flap,inertial},\mathrm{Z}} = \frac{8\pi^3 I_{yyw,0}\Gamma^3}{n\mathrm{Z}}\sin\left(4\pi ft\right) \sim n^{-1} \tag{26}$$

indicating that $P_{\text{flap,inertial,Z}}$ is inversely proportional to n. The effect of f on $P_{\text{flap,inertial}}$ can be similarly determined as

$$P_{\text{flap,inertial},f} = 8\pi^3 I_{yy,w0}\Gamma fn\sin\left(4\pi ft\right) \sim n \tag{27}$$

38

which shows that $P_{\text{flap,inertial},f}$ is proportional to n. As the wing size increases, the flap amplitude contribution reduces. However, the flap frequency contribution to the inertial flap power increases with n. As a result, there is an optimal wing size as shown in Fig. 16. This is because both f and Z have a similar order of contribution to produce lift that balances the weight (Eq. (25)). However, $P_{\text{flap,inertial}} \sim f^3$ whereas $P_{\text{flap,inertial}} \sim Z^2$ (Eq. (23)), yielding the qualitatively different influences of the flap amplitude and frequency on the inertial flap power. The pitch power trends are qualitatively similar.

For illustrative purposes, scaling the wing up by $n=3.5$ in each dimension is equivalent to a bumblebee using the forewing from a cicada. Operating such a large wing is necessary to compensate for the low-density environment on Mars. However, as previously mentioned, the penalty associated with using such large wings is clearly seen in the power required to actuate them (Table 5). There are methods for optimizing the wing kinematics [103] such that power is reduced, as well as many practical methods for eliminating sources of power in flapping wing motions, as discussed in the following section.

4.6.2 Payload Considerations

The baseline case for the present study is the case where a bumblebee wing is uniformly scaled by a factor of 3.5 in all directions on a bumblebee body (Section 4.3.1) [66]. This case resulted in minimum power (Fig. 16). As only the wing size and therefore wing mass was scaled for this solution, the body remained the body size and mass of a morphological bumblebee. As such, we can now examine the effects of maintaining a constant wing size of the baseline case and increasing the body mass to simulate the payload capacity for this configuration. By investigating a case where the wing size is held constant, we will not include the effects of changing aspect ratio. Similarly, we fix the pitch amplitude to remain at A=40° for all cases as this generates the highest lift when coupled with advanced rotation of the wing [61,82]. The baseline parameters are shown in [67] which details the pertinent morphological parameters, kinematic parameters, dimensionless parameters, and required power. We first determine the maximum payload capacity while maintaining dimensional similarity.

Figure 17 shows the variation of kinematic parameters used in the computational simulations for each case of increased payload fraction Δ considered (Section 4.3.1). We consider two parametric variations: i) the flapping frequency is held constant at f=63 Hz; ii) the flapping frequency is manually increased with increasing Δ. In our computational framework, the flapping frequency is prescribed (Fig. 17a) and the stroke plane angle β, flapping amplitude Z, and stroke offset ζ_φ (Fig. 17b,c) are the resulting controls that are output by the coupled NS-flight dynamics solver. The kinematics used for each case show that as the payload fraction Δ increases, either the flapping amplitude must increase (Fig. 17a) or the flapping frequency must increase (Fig. 17c) in order to increase lift to balance the weight (Eq. (1)). This explains why the flap amplitude in Fig. 17c is not constant but is rather approximately 55° for all cases considered. As we only consider hover flight, the stroke plane angle in Fig. 17b and flapping offset angle in Fig. 17c are small relative to the flapping amplitude and differ only marginally between cases.
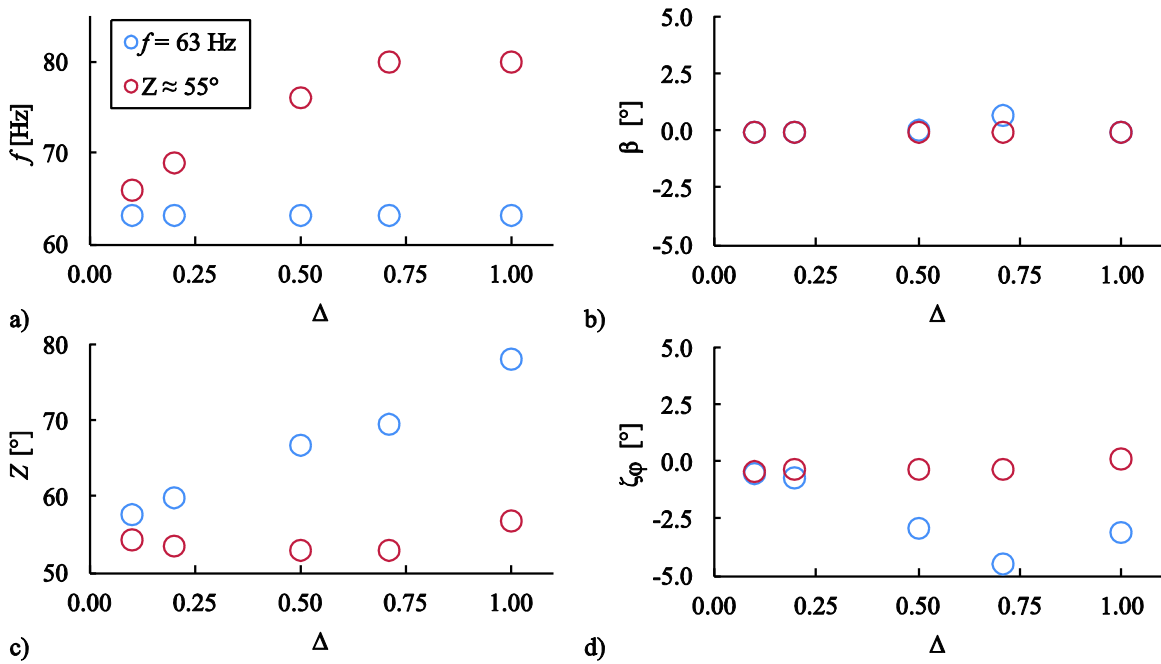
Figure 17. Values for a) the input frequency *f* and b-d) the controls solutions from the coupled NS-flight dynamics equations. The controls parameters are b) stroke plane angle β, c) flapping amplitude Z, and d) flapping offset angle ζ_φ. a-d) Are a function of increased payload fraction Δ for fixed flapping frequency (blue) and fixed flapping amplitude (red).

The dimensionless parameters found in Fig. 18 are the only ones which vary as a function of increased payload fraction. The other two parameters which govern dynamic similarity in this study, aspect ratio and angle of attack, are held constant. For the varying dimensionless parameters corresponding to increased payload fraction, Figure 18 shows that they are all within their respective ranges for typical insect flight. This affirms that the resulting solutions for the flapping wing motion with increased payload benefits from the unsteady, high lift mechanisms achieved by insects, even though the simulation is conducted in the much lower density Martian atmosphere.

Figure 19 shows the resulting power and average lift coefficient as a function of increased payload fraction. The maximum payload capacity for the present case is about 100% of the baseline body mass. The main limiter of this maximum payload value is the constraint on the wing tip Mach number (Fig. 18a). Most insects operate at a Mach number below 0.1 (Table 3). As such, the flapping speed is limited in the potential magnitude of flapping amplitude and frequency, as both scale the wing tip Mach number. Payloads above 100% would result in $M \geq$ 0.1, which would no longer guarantee that the flapping wing motion benefits from the unsteady, high lift mechanisms of typical insect flight observed in Earth. Note that in the Fig. 19a where the flapping frequency is held constant and the flapping amplitude can vary to achieve appropriate lift, the resulting wing tip Mach number extends slightly beyond the bioinspired threshold for Mach number. Conversely, in the case where flapping amplitude is held roughly

constant at 55°, there is still margin which allows for a slightly larger payload to be carried. For this case, there is a clear advantage for operating at a low flap amplitude and increasing the flapping frequency to achieve lift and maximize the total amount of payload while producing a dynamically similar solution.

However, as demonstrated in Fig. 19a, the power required for additional payload $P_{tot,\%}$ is larger for the case where Z is held approximately constant and the flapping frequency varied. This means that with respect to the variables considered, the largest payload mass can be achieved when the flap amplitude is small enough to satisfy the reduced frequency restrictions and the frequency is large enough to balance the weight and not force M_{tip} to extend beyond its typical insect range. However, as was discussed in Section 4.6.1, increasing flapping frequency scales the total power required at a faster rate than increasing the flapping amplitude and can result in very large power requirements.
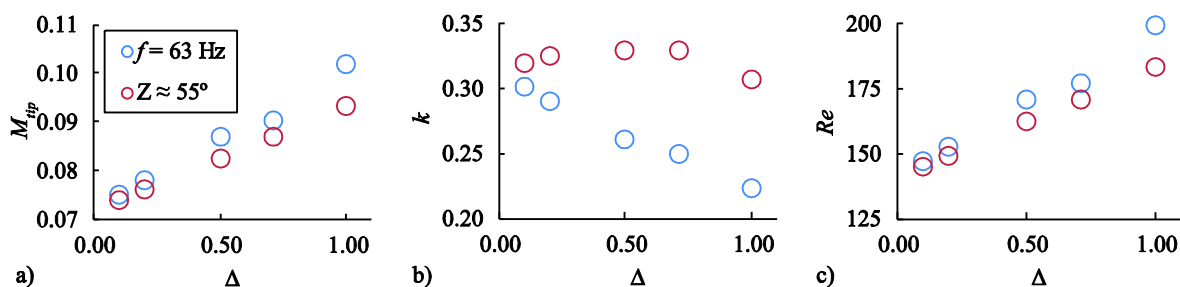
Figure 18. High-fidelity numerical solutions illustrating the resulting a) wing tip Mach number and b) reduced frequency and c) Reynolds number, when additional payload fraction is added to the flapping wing flyer for both fixed flapping frequency (blue) and fixed flapping amplitude (red). The kinematics considered for each payload amount result in dimensionless parameters (a,b) that fall within the ranges typically found in insects (Table 3). The wing tip Mach number a) scales nearly linearly for both fixed amplitude and fixed frequency but has a lower slope when frequency is fixed, allowing for a slighty larger payload while remaining dynamically similar. The reduced frequency in b) reduces for fixed frequency and remains nearly constant when the amplitude is approximately constant, as expected.

4.6.3   Energy Harvesting Method with Torsional Springs

While the low-density Mars atmosphere poses a challenge to generate lift, the proposed bioinspired flapping wing concept has the potential to benefit from the low-density environment by substantially reducing the flight power consumption, implying an improved payload margin and flight time.

Because of the ultra-low Martian density, the power consumption due to aerodynamic damping (aerodynamic power) is orders of magnitudes smaller than the power needed for
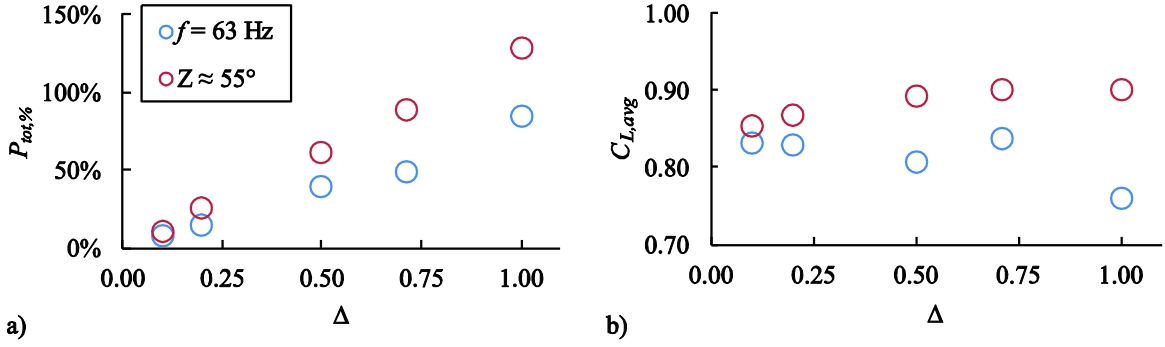
Figure 19. High-fidelity numerical solutions for a) total power as a percent of the baseline power required and b) the average lift coefficient as a function of increased payload fraction Δ. The total power a) increases nearly linear for both cases but has a smaller slope for fixed frequency. The average lift ceofficient b) is nearly constant for both cases, with the the average value being slightly higher for fixed flapping amplitude.

accelerating and decelerating the wings during flapping (inertial power). Therefore, the total power is dominated by the inertial power. A torsional spring at the wing root stores the wing kinetic energy during the decelerating half-cycle to drive the next accelerating half-cycle, reducing the inertial power when operating at resonance [34]. Whereas rotary wing concepts are more mature in both design and control, this energy harvesting mechanism is uniquely suited to flapping wing motions.

In order to reduce the total power required we propose another benefit of using the flapping motion as a propulsive mechanism on Mars. We place a torsional spring (patent pending) at the root of each wing to temporarily store otherwise wasted energy and reduce the overall inertial power when driven at resonance. The effects of a spring on the flapping wing motion are modeled by a second order ordinary differential equation as

$$I_{yy,w0}\ddot{\zeta} + T_{aero} + k_T\zeta = T_{req} \tag{28}$$

in the wing frame, where $I_{yy,w0}$ is the wing root (flap) moment of inertia, T_{aero} is the aerodynamic torque, k_T is the angular spring constant, T_{req} is the torque required from the forcing function, and φ is the instantaneous flapping angle of the wing. The dot and double dot represent the first and second time derivative, respectively. Equation (21) relates the flapping wing kinematics to the material properties of the spring and the forcing function required to impose the desired motion φ given by the trimmed solution.

According to Eq. (2), the flapping motion is sinusoidal and can therefore be written as $\zeta(t) = Z\sin(2\pi f t)$. When ζ and $\ddot{\zeta}$ are substituted into (28), the result is

$$-(2\pi f)^2 I_{yy,w0}Z\sin(2\pi f t) + T_{aero} + k_T Z\sin(2\pi f t) = T_{req} \tag{29}$$

42

We choose the spring constant to align the undamped natural frequency f_n with the flapping frequency,

$$2\pi f_n = \sqrt{\frac{k_T}{I_{yy,w0}}} \rightarrow k_T = \left(2\pi f_n\right)^2 I_{yy,w0} \tag{30}$$

When Eq. (23) is substituted into Eq. (22) the inertial and spring terms cancel out, resulting in $T_{req}=T_{aero}$. Thus, when the torsional spring is driven at its resonant frequency, the required torque for the flapping motion is only comprised of the aerodynamic torque, which is orders of magnitude lower than the inertial torque. As a result, the total power required reduces substantially. This method takes advantage of the ultra-low density environment on Mars and negates the increased inertial flap power required due to wing scaling. Where the low density was initially an obstacle to overcome, it is now a benefit when considering torsional springs placed at the wing roots.

Note that a similar, closed form analytical expression is not derived for the inertial pitching component of the total power required. This is due to the fact that the pitch motion is described in terms of a hyperbolic tangent function, as seen in Eq. (3). This limits the ability to express the derivatives required for writing Eq. (14) in a concise analytical form. Additionally, for both the aerodynamic flapping and pitching power components, we are unable to rewrite the Navier-Stokes equations in a way that captures the all of the flapping/pitching motion of the wing, as well as the body motion. However, it still stands that the most dominant source of power is the inertial flap power, as demonstrated by Figs. 15 and 16. This means that the expression for the inertial flap power in Eq. (23) captures the important kinematic/morphological parameters that drive the overall power required.

Figure 16b compares the flapping power required for Marsbees with wings that have been scaled by a factor of $2<n<4.5$ with and without torsional springs. The power required for the simulations which include the springs is composed of the aerodynamic flapping power and both the inertial and aerodynamic pitching power. For the case where $n=3.5$, the total power required is reduced by 79% from 0.19 W to 0.04 W when torsional springs are placed at the wing roots. Note that the resulting power of 0.04 W is now only 3.3 times the power required for a natural bumblebee to fly on Earth, which is 0.012 W (Table 5).

Considering the specific power for the case of $n=3.5$ on Mars, the total specific power for wings without torsional springs is 901 W/kg (Table 5). This can be compared to the $n=3.5$ case with the torsional springs which has a total specific power of 188 W/kg, and the nominal earth bumblebee specific power of 68.6 W/kg. As a measure of ideal flight endurance, where the entire body mass is comprised of a lithium-ion battery with a specific energy of 243 Wh/kg (Panasonic NCR18650B lithium-ion battery), the flight times for the case of $n=3.5$ are 16 minutes without the springs and 78 minutes with the springs. This ideal scenario assumes a 100% efficiency for the transmission of power from the battery to the MAV's wings. Even in the baseline case

without the springs, the endurance time is similar to that predicted by the Mars Scout Helicopter, which is approximately 90 seconds [24].

For a bioinspired flexible wing design with both the flapping and pitching inertial powers minimized, we expect the time to further improve to an optimal value of 348 min (5.8 hrs), a more than 40 fold increase over the rigid wing design. Assuming battery energy density increases to 400 Wh/kg by 2030 [35,36], an optimal configuration can hover for 9.5 hrs in 2030 as shown in Fig. 4. Flexible wings can also be made much lighter than a rigid wing, further enhancing the Marsbee performance.

5 PROOF-OF-CONCEPT EXPERIMENTS IN MARTIAN DENSITY CONDITIONS

Using multi-fidelity tools, we showed in Section 4 that bioinspired wing shapes and motion can yield sufficient lift to sustain a Marsbee in the Martian density condition. In order to further test the hypothesis that bioinspired flight mechanisms can produce sufficient lift to fly on Mars, a Marsbee prototype robot was designed in order to experimentally verify the ability to produce such forces. The robotic flapper was placed in vacuum chambers where the density was reduced to the Martian density level. Initial experimental tests were conducted with the hummingbird-inspired flapping mechanism (Fig. 3; Section 2). However, since this mechanism was unable to generate the high flapping frequencies required at Martian conditions, further tests were carried out with an improved version of the Marsbee robot.

5.1 Marsbee Flapper and Vacuum Chambers

The experimental setup consists of the Marsbee robotic flapper on a custom test stand that allowed for measurements of the unsteady forces produced by the Marsbee robot and of the flexible wing deformations of the Marsbee wings.

This test stand was placed inside two vacuum chambers located at UAH's Propulsion Research Center (PRC). The first vacuum chamber is located in the Large Vacuum Test Facility. This large vacuum chamber has a test section with a diameter of 1.8 m and a length of 4 m. The second chamber has a smaller test section measuring 0.3 m diameter and 0.6 m length. Both chambers use a convection vacuum gauge sensor (InstruTech CVG101 Worker Bee) and are capable of very low vacuum including the pressure and density levels required for achieving Mars atmospheric conditions. The experimental setup is shown in Figs. 20 and 21.

We used the 5 g zeroth-order solution (Fig. 9) with a single wing area of 0.0070 m^2, a peak to peak flapping amplitude of 47 deg, and a flapping frequency of 35 Hz to design the robotic Marsbee flapper (Fig. 21c). The Marsbee prototype flapper was tested in both two and four wing configurations with several different wing materials in order to determine a
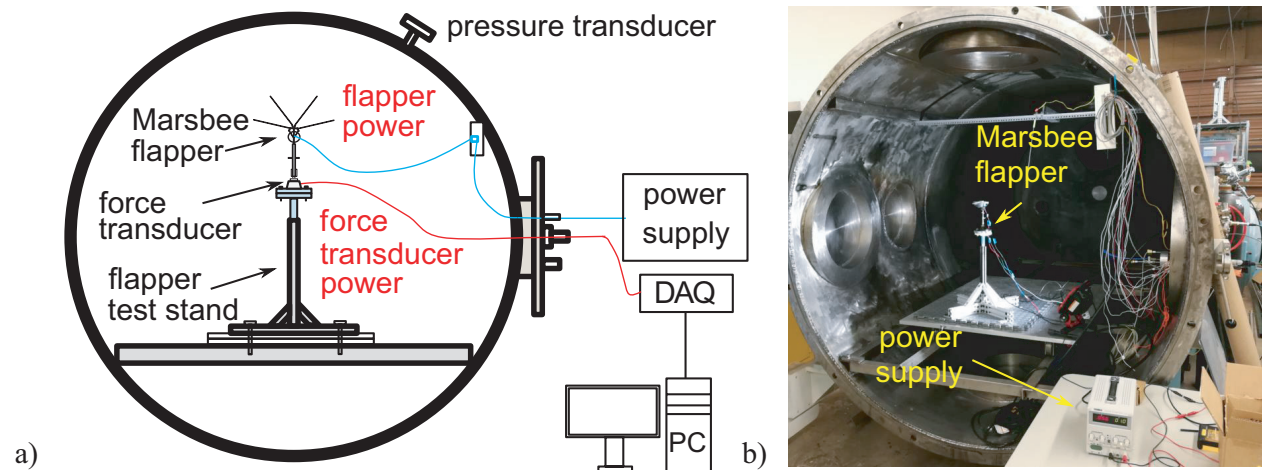
Figure 20. Marsbee experimental setup in the large vacuum chamber. a) Schematic representation and b) Marsbee test stand inside the chamber.
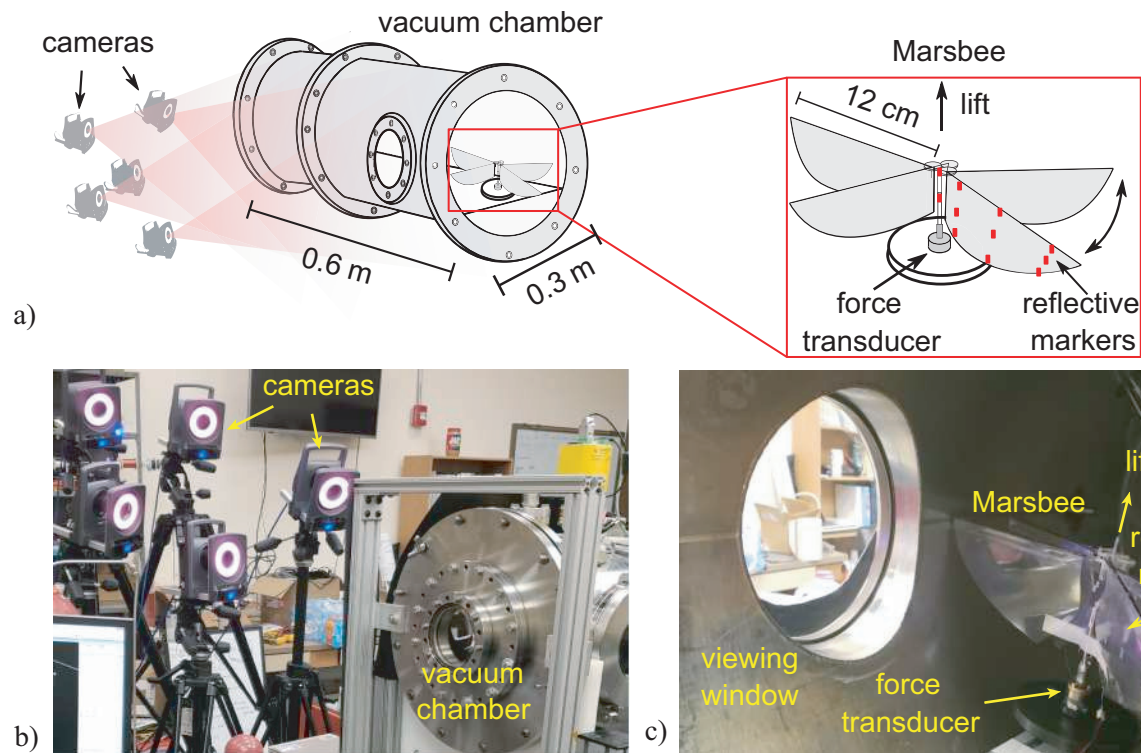
Figure 21. Marsbee experimental setup in the smaller vacuum chamber. a) Schematic of vacuum chamber and motion tracking cameras. b) Outside view of the vacuum chamber with the Vicon motion tracking cameras looking through the chamber's side viewing window. c) Interior view of the vacuum chamber housing the Marsbee test stand.

configuration suitable for testing at Martian conditions. We selected the four wing configuration similar to the hummingbird-inspired MAV (Fig. 3), using the gear system purchased from Micron Wings (Fig. 21a,c). Although the flapping mechanism is constrained to a single wing peak-to-peak flapping amplitude of about 50 deg, the reduction in the flapping amplitude is partly made up by an increase in the wing area. The robotic mechanism uses four wings, each with an area of 0.0070 m^2, resulting in the Marsbee robotic flapper having nearly double the total wing area relative to the (two-wing) zeroth-order results.

Although the total effect of wing area and flapping amplitude are closely matched to the zeroth-order results, the flapping frequency dictated by the zeroth-order method was not achieved with the robot (Fig. 25; Section 5.3) due to the lack of power in the available motor and structural integrity. Design and development of a Marsbee flapper that addresses these shortcomings are left as a future study.

Initial tests were performed in the large vacuum chamber. However, we discovered that the relatively large Marsbee wings in the Martian density conditions deform in a way that is qualitatively different than in Earth density condition. To compare how the wings deform in both density conditions, high-speed videos were taken of the Marsbee robotic flapper in both ambient Earth conditions and the reduced-density Mars conditions (Fig. 22). Because the Marsbee wings are based on a flapping wing micro-air vehicle that was designed for flying on Earth, the fluid-

a) Earth density condition
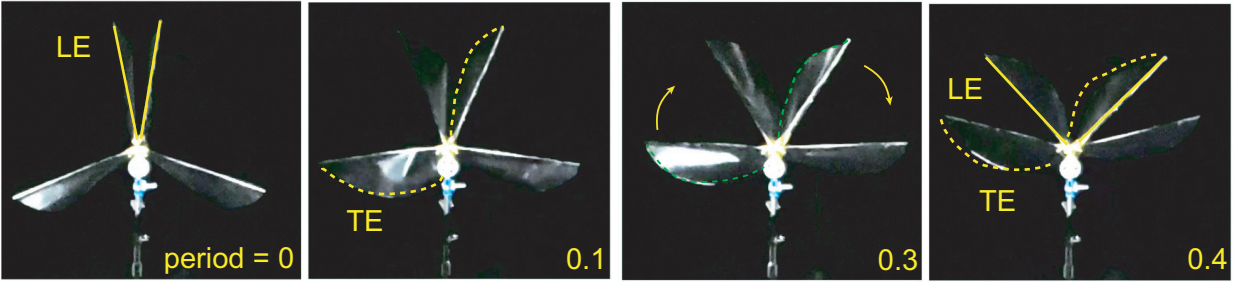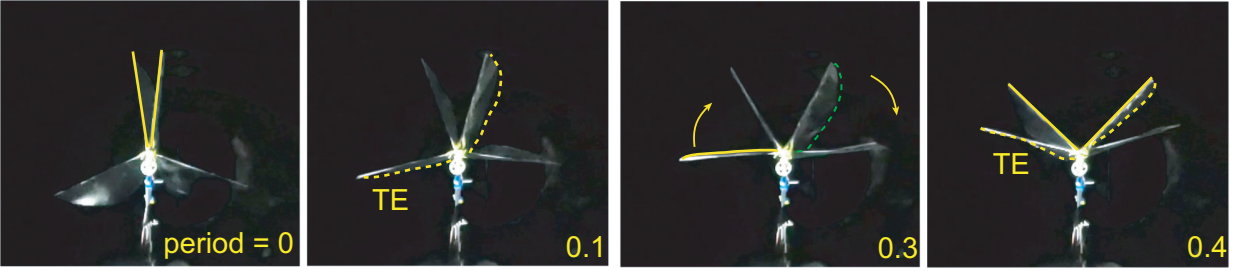
b) Martian density condition

Figure 22. Snapshots of the wing and passive pitch motion in a) ambient Earth and b) Martian atmospheric conditions. In the ambient Earth density condition, the trailing edge follows the leading edge as the pairs of upper and lower wings come together, similar to insect wing motions [10]. However, the trailing edge leads the leading edge in the Martian density conditions.

structure interaction was optimized for the Earth density condition. Similar to the wing motion of flying insects [10], the wings passively pitch with the trailing edge of the wing following the wing's leading edge. However, in Martian conditions where the density is about 1% that of Earth's, the resulting fluid-structure is qualitatively different: the trailing edge of the wing leads in front of the leading edge (Fig. 22), resulting in the wing motion in the opposite direction of what insects use.

Attempting to correct this motion in the large chamber proved to be a time-intensive task, as pumping down such a large volume of air to Martian conditions takes nearly 15 minutes. In order to speed up testing and have more viewing ability, the experimental setup was moved to the smaller vacuum chamber. This chamber is large enough to house the Marsbee robotic flapper and force transducer. Also, the pumping process is much faster, achieving Martian density conditions in about 5 minutes.

5.2   Force and Optical Wing Motion Measurement Setup

The forces were measured using the ATI-Nano-17 Titanium force transducer. Before the start of each trial, the transducer was setup such that the load due to the flapper's own weight was zeroed. The motion of the flapper was actuated by supplying a series of input voltages. For each trial, forces were recorded for five seconds. The mean lift is calculated by time-averaging the force in the lift direction over the five second interval. We separated the inertial force from

the aerodynamic force by following a well-documented procedure [104].

The wing motion was measured using an optical approach. Nine small, reflective tape markers were placed on one of the wings of the Marsbee flapper. The 3D position of each marker was recorded using Vicon T40s cameras placed outside of the small vacuum chamber (Fig. 21a,b). Each reflective marker is 3×5 mm in size and weighs approximately 3.9×10^{-3} g. The total mass of all nine markers was around 9% of the mass of the individual wing. We used this optics-based method previously to measure the wing motion of freely flying Monarch butterflies [105].

Five Vicon cameras were positioned outside the chamber (Fig. 21a,b) and calibrated such that the markers positions inside the chamber could be clearly recorded through a glass viewing window located on the side of the chamber. The marker distribution on the wing was chosen such that both chordwise deformation of the wing as well as the 3D shape of the wing could be measured. In addition to the wing markers, two more markers were placed on the flapper body as a reference line as shown in Fig. 23b. The flapping angle was determined using the position of markers A and G (Fig. 23). The pitching angle was calculated as the angle between line joining G and I with respect to longitudinal axis of the flapper formed by markers A and B. The chordwise deformation of the wing was determined using the straight line connecting wing markers G and I. The flapping frequency was obtained by taking the FFT of the time history of flapping angle.

The experimental setup enables simultaneous measurements of flapping wing kinematics and the resulting time history of forces in Earth and Martian atmospheric conditions at various flapping frequencies. The wing motion was recorded at a sampling rate of 400 Hz and the forces were recorded at a sampling rate of 2000 Hz. Both the Marsbee flapper and the force transducer were located inside the chamber and powered using externally located power supply units. The input voltage to the to the flapper was supplied using Tekpower TP3005P power supply. The force transducer output was connected to a National Instruments Data Acquisition (DAQ) board and the measured data was saved to an external computer. Any gaps in the recorded marker position data were interpolated using cubic spline interpolation. The wing motion data were smoothed using a low pass filter with a cut off frequency of 50 Hz. The recorded force data,
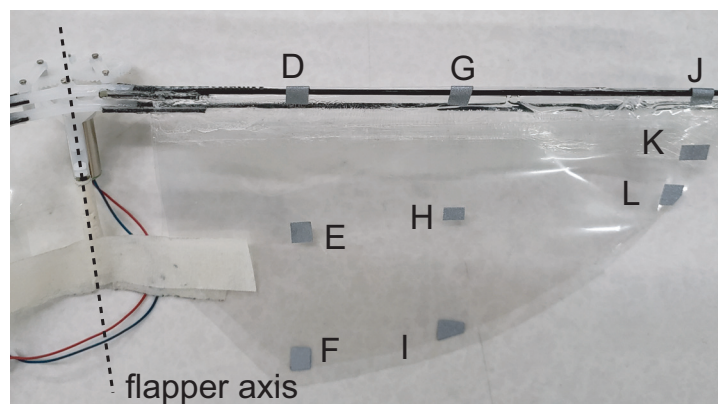
Figure 23. Position of the reflective markers on the Marsbee wing.

which included higher frequency oscillations, were filtered using a low pass filter with a cut off frequency of 100 Hz.

5.3 Lift and Wing Deformation Measurements in Martian Conditions

The temperature and pressure inside the chamber were recorded during the experimental procedure. At Earth conditions, the temperature and pressure inside the chamber were 23º C and 99325 Pa, respectively, resulting in an air density of 1.168 kg/m^3. At simulated Martian conditions, the temperature inside the chamber was 23º C for all tests. We varied the pressure between 1133.4 Pa and 1333.2 Pa, resulting in an air density of 1.333×10^{-2} kg/m^3 and 1.568×10^{-2} kg/m^3, respectively, during the tests, which is within the Martian atmospheric density range (Fig. 2).

The forces and wing motion of the flapper were first recorded at Earth conditions inside the chamber followed by Martian conditions. The wing motion and forces generated by the flapper were recorded for a range of input voltages. At Earth conditions, we varied the input voltage to the flapper between 0.5 V and 2 V in 0.5 V increments and between 2 V to 2.6 V in 0.2 V increments. The input voltage for Martian conditions was varied between 0.8 V and 2.6 V in 0.2 V increments in order to achieve a range of frequencies comparable to the frequencies achieved in Earth density conditions. Three repeated measurements were acquired at each voltage.

The mean lift recorded based on three repeated measurements is shown in Fig. 24 at Earth and Martian conditions as a function of the flapping frequency. The Marsbee flapper generates positive lift in both conditions. At 16 Hz, the mean lift normalized with Martian gravity was around 8 g. The lift at Martian condition increases between 8 Hz and 14 Hz followed by a nonlinear drop. The magnitude of lift (in grams) is similar to the lift of these Marsbee wings in Earth density condition, producing around 11 g of lift at 17 Hz. The mean lift in Earth density conditions increases with the flapping frequency. These results indicate that the Marsbee flapper
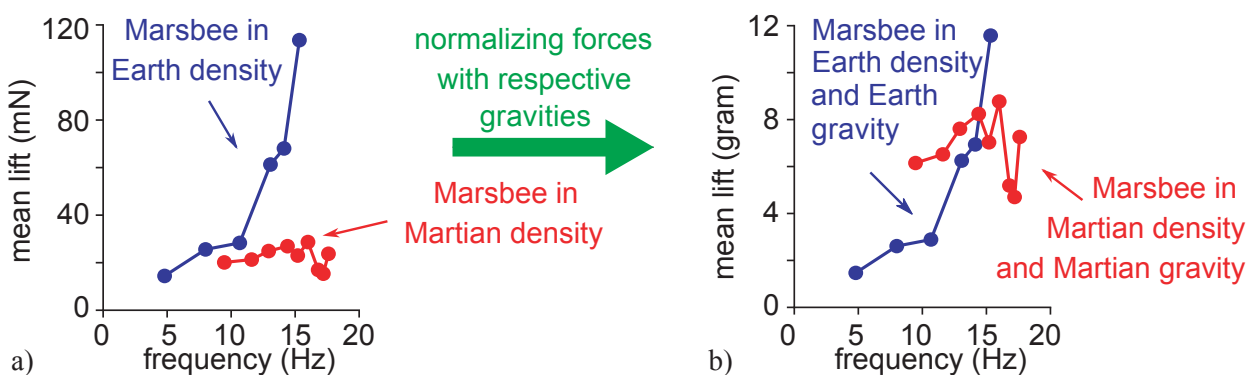
Figure 24. Experimental measurements as a function of flapping frequency at Earth and simulated Martian atmospheric conditions. a) Measured lift in mN; b) Measured lift in grams. The mean lift at Earth and Martian densities are normalized with 9.8 m/s^2 and 3.26 m/s^2, respectively.
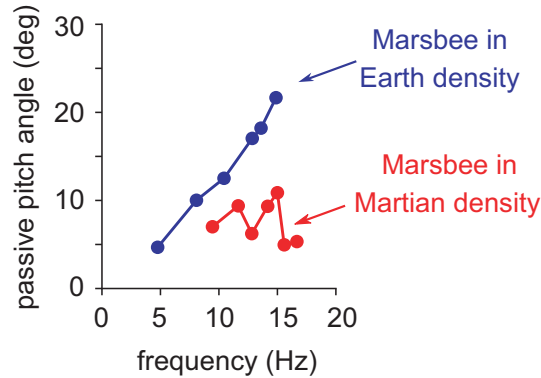
Figure 25. Comparison of passive pitch angle at Earth and Martian density conditions.

at Martian conditions is capable of producing lift comparable to its weight.

The mean lift trend in Fig. 24 can be explained with the wing deformation measurements. A key mechanism in generating positive lift is the passive pitch angle resulting from wing deformation. In dynamic balance of the wing inertia, elastic restoring force and aerodynamic force, the flexible flapping wings deform, producing passive pitch angles. For flexible wings, passive pitch angle plays the role of angle of attack. A pitch angle of 45 deg is known to produce the highest lift [106].

For the Marsbee wing in Earth density condition, the passive pitch angle increases with flapping frequency, reaching 18 deg at 15 Hz (Fig. 25). Lift increases with pitch angle in general. On the other hand, in Martian density conditions, the wing deforms in a nonlinear way, producing a mean lift trend (Fig. 24) that is qualitatively different than the trend in Earth condition. The trend of mean lift as a function of flapping frequency appears to be similar to the passive pitch angle trend (Fig. 24a and Fig. 25). With an increase in frequency, the mid-stroke passive pitch angle remains nearly constant in the Mars conditions.

The wing snapshots for a representative trial further show that pitch angle due to wing deformation during the midstroke is in the non-optimal, opposite direction (Fig. 26). As visualized in the high-speed video snapshots in Fig. 22, the trailing edge leads the leading edge in the Martian density conditions. On the other hand, in the Earth density condition, the trailing edge lags the leading edge, resulting in a motion that is similar to flying insects [10]. The pitching motion shown in the Earth condition produces high lift in an efficient manner.
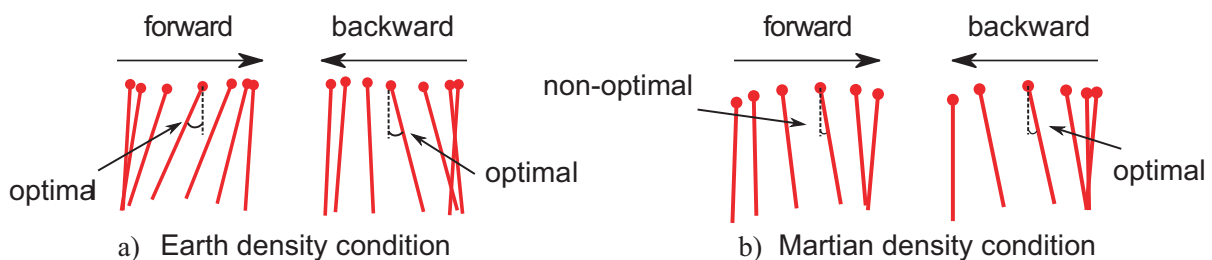
Figure 26. Representative chordwise wing shape snapshots at a) Earth and b) Martian density conditions.

50

In short, the resulting combination of the flapping and pitching motion is able to generate positive lift in the Martian density condition. However, the resulting pitch motion due to the larger wings is not optimal, suggesting that the bioinspired lift generation in Martian conditions can be improved by taking into account the fluid-structure interaction in the ultra-low Martian density conditions.

5.4   Specific Power

The resulting specific power input as a function of the flapping frequency is shown in Fig. 27. The power input is calculated as the product of the average voltage and current readings. The specific power is an order of magnitude lower in the Martian than in the Earth condition for a given frequency, suggesting that significantly less power is required to produce similar levels of lift forces. Such a low specific power input level is also consistent with the flight time estimation from the numerical simulations in Fig. 4, further illustrating the benefit of bioinspired lift generation on Mars using flexible wings.
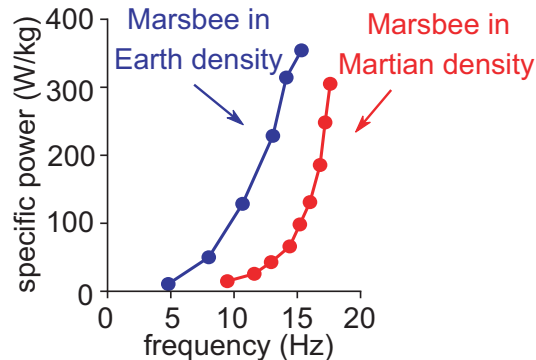
Figure 27. Specific power determined from voltage and current readings.

6   SYSTEMS ANALYSIS OF MARSBEE

It is critical in any design to understand the emergent behaviors of the system. These are the behaviors that results from subsystems interacting to produce outputs that a single subsystem is incapable of producing. For example, lift is not possible in the Marsbee system without interactions between multiple subsystems, such as the wings, motor, frame, and battery. Furthermore, the system context can be expanded to include the missions and capabilities of the system, enabling the investigation of higher level preferences of stakeholders. This section explores the Marsbee system, using mathematical methods to understand the subsystems, their interactions, and the system's emerging behaviors. Design Structure Matrices will be used to decompose the system into its subsystems. Value modeling will then be used to begin representation of stakeholder preferences and enable comparison to alternative systems. Two reviews will be performed on technologies that are identified as critical to mission success: batteries and sensors. Together, these tasks form a systems foundation founded in mathematics and evidence for the Marsbee system.

6.1   Marsbee Design Structure Matrix

6.1.1   Background and Methodology

Systems consist of multiple interacting subsystems producing emergent behaviors that are not possible without the subsystem interactions.   A traditional approach to understanding complex systems is to hierarchically decompose them into subsystems. Once a decomposition is established, then a Design Structure Matrix could be formed to represent the interactions that occur between the subsystems [50]. A Design Structure Matrix (DSM), aka. Dependency Structure Matrix/Dependency Source Matrix/N^2 Matrix is a visual representation of the subsystems and their interactions in the form of a square matrix [51]. There are four general types of DSMs [51,52], which are summarized in Table 6.

As an example of a DSM, consider a system of interest which comprises of subsystem A, B, C & D and their interactions are such that A feeds forward to C, B feeds forward to D and C feeds backward to A to form a loop. This interaction can be represented visually in the form of a DSM, as shown in Fig. 28, where A, B, C & D are subsystems and the 'x' in the off diagonal elements represents a relationship between the two. The diagonal elements are blocked off since it would be a subsystem's relationship with itself and do not have an interpretation in describing system behavior [52]. Here, we use the lower half of the DSM to represent feed forward interactions and the upper half to represent feedbacks.

The field of Multidisciplinary Design Optimization (MDO) uses this method to decompose large unwieldly systems into smaller and more manageable subsystems, coupled together by the flow of information between them [53]. A general methodology used in composing a DSM is to first decompose the system into elements (subsystems), document the interactions/couplings between elements, and finally use this information for further purposes such as sequencing to improve analysis efficiency [107]. The types of interactions or couplings

which can be captured in the DSM can be physical or spatial adjacency, energy flow, information flow, vibrations, material flow, heat transfer, force exerted, etc. The preliminary version of the Marsbee DSM uses a simple X to represent an existence of a relation between two subsystems. The relation can be decomposed into multiple boxes, each representing a different type of coupling. For example, if we were to represent four types of interactions, namely information flow, energy flow, vibrations and force, the matrix would look like Fig. 29, with each feedback or feedforward coupling box being decomposed into 4 smaller coupling boxes.

Table 6. General types of Design Structure Matrices.

type	characteristic	application
product architecture DSM	Breaks down a product into subsystems, components and their functions with increasing level of decomposition	System architecture, engineering and design
organizational architecture DSM	Breaks down the system of interest into sub-departments, teams and individuals with increasing level of decomposition	Organizational design, interface managements and team integration
process architecture DSM	Decomposes the system into its sub processes, activities and parameters.	Project scheduling, activity sequencing and process construction.
product + organization + process architecture DSM	A combination of Product + Organizational + Process Architecture DSM	Applied to a complex system which includes all the above categories.

The strength of the coupling, i.e. how strongly the two systems are connected, and the level of change it causes to the overall system, when it is modified, can be calculated in a number of ways. One method of quantifying the relationships between subsystems is by weighting the interactions relative to each other [50] in which the off diagonal elements are replaced by integer numbers which depict the strength of the coupling. The weighting information can be obtained via engineering diagrams, architectural diagrams, system schematics or by interviewing the engineers and subject matter experts. Use of a quantification scheme which sets a guideline for weighting the interactions between subsystems can also be used [107]. Some of the methodologies to identify the subsystems and their interactions include conducting interviews
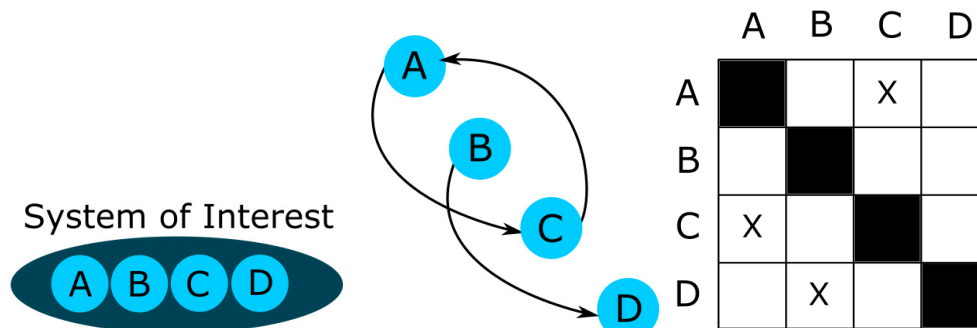
Figure 28. Progression of system into DSM form.

with engineers involved in designing the system who have a deep understanding of the system of interest, and let them identify the couplings, and their strengths by order of their importance [108,109]. Some methods also describe studying the design of a system by collecting data which is done by attending meetings, participating in the design process, and concluding it with interviewing design experts [110].

Table 7. Summary of Design Structure Matrix analysis steps.

step	purpose
sequencing	To achieve a task order with minimum number of feedback loops. It provides a smoother information flow where all prior information required for a task is available beforehand.
cycle detection	After sorting, this step helps to identify existence of information loops/iterations in the design process.
partitioning	Once the tasks that are contained in the same loop are identified, they are put in a block around the diagonal of the matrix.
tearing	Purpose is to break cycles & achieve a sequence with no loops. This reduces the likelihood of iterations in the design process.

Since the methods discussed above for identifying the couplings and their strengths do not offer a mathematical foundation it should only be used for a preliminary analysis [54]. A more efficient approach used to identify couplings and their impacts in a large system is to use the Global Sensitivity Equations method, where each subsystem is analyzed keeping in mind its interaction with all the other subsystems (local sensitivity) and its sensitivity with respect to the entire system (total sensitivity) [111]. After a DSM has been built the next step would be to use the DSM to analyze the system. The analysis of the subsystems can be modified to improve the efficiency of the system analyses. The DSM can be sequenced, partitioned and torn, and clustered [112]. A brief summary of the steps, and their purposes for the DSM is shown in Table 7.
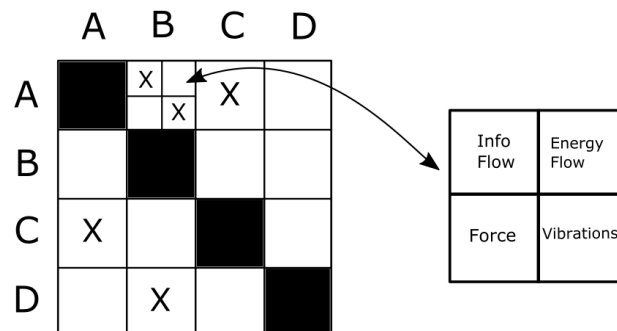
Figure 29. Decomposion of feedback or feedforward coupling boxes.

6.1.2 Results

The Marsbee system was hierarchically decomposed into its subsystems as shown in Fig. 30. The decomposition was constructed using CAD drawings, design team member inputs, and through discussions at team meetings. The system was decomposed into physical parts, following a product architecture decomposition approach. Seven high level subsystems were identified, as well as six lower level subsystems. This decomposition is preliminary and is able to characterize the current Marsbee design with flexibility to characterize minor alterations. Further decomposition of the subsystems would enable a more complete depiction of the system complexity, but would also reduce the feasible design space. In future design iterations further subsystems may be identified to enable a finer design solution.
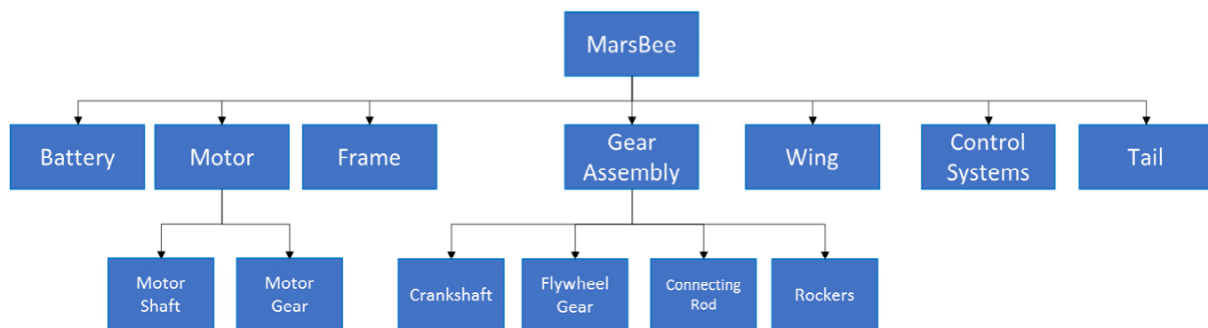
Figure 30. Decomposition of the Marsbee system.

Once a subsystem level decomposition was created, a preliminary DSM was formed to show the couplings between the subsystems. This preliminary DSM was presented to the design team and alterations were made. The preliminary DSM formed in this work is shown in Fig. 32. The subsystem couplings are decomposed into four coupling types: energy flow, vibration, information flow, and force exerted (Fig. 31). The numbers represent the team's assessment on how impactful the couplings are on the subsystem being affected. These are preliminary assumptions and will be supported by mathematical derivatives in future work.

The DSM indicates critical subsystems related to specific coupling types. The battery and control subsystems are primary subsystems in the exchange of energy, with the battery as a source of energy and the control system as a manipulator of energy. The frame is critical when analyzing forces and vibrations. Due to the low weight of the vehicles there may be significant changes in the center of mass, this will need to be consistently analyzed as changes are made to the subsystems and payloads. The motor also is a key generator of force, with a loss of coupling in one motor subsystem having a chain reaction of failures throughout the system. Future design iterations should focus on reducing the number of couplings in the motor system to reduce the risk of failure of the system. The preliminary DSM will be used in future work to increase the efficiency of analyses through techniques previously mentioned, as well as provide a guide to subsystem designers concerning what information they need from other subsystems, and what information other subsystems need from them.
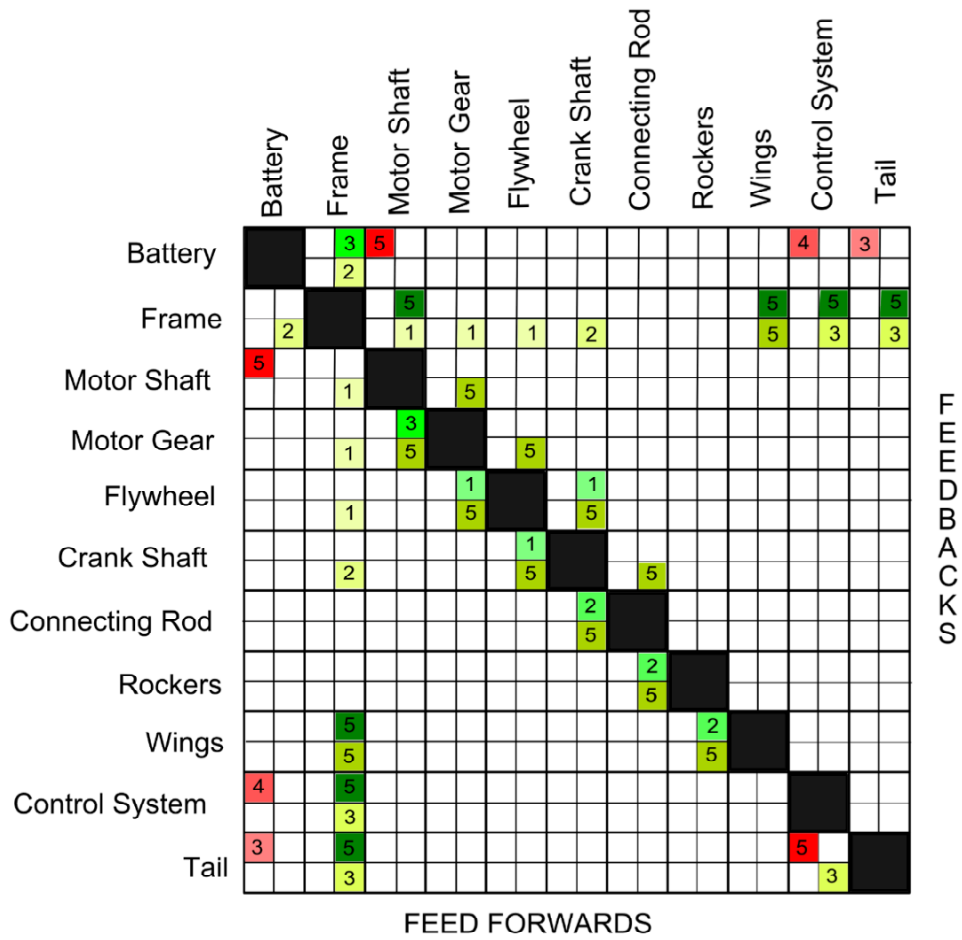
Figure 32. Design Structure Matrix of the Marsbee system.
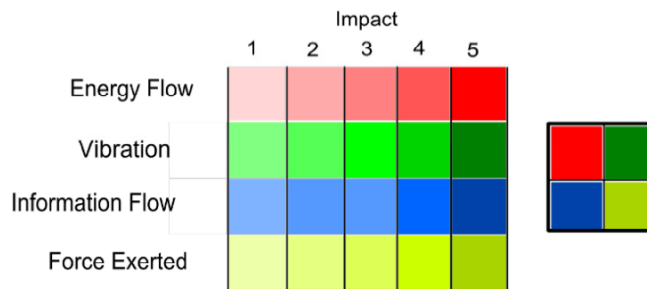
Figure 31. Marsbee subsystem coupling types.

6.2   Value Model for the Marsbee System

The formation of a value model [44–49] is a multi-step, iterative process. In Phase I of this work the research team was tasked with developing a preliminary Marsbee system model and relate the findings to previously developed NASA value models. To form the preliminary system value model, the research team employed a single iteration of a three step approach: templating, evidence and analysis, and stakeholder preferences elicitation.

The templating step involved a brainstorming session within the research team to propose system level attributes that would be of importance to the stakeholder. The system level attributes identified as key influencers on system value include: range, payload size and mass, data type and transmission, modularity, robustness, and cost.   These attributes represent important influencers on the believed missions that Marsbee will be undertaking, as the system without a mission would have negative value (equal to its cost). The templating step generated the pseudo-value model (Fig. 33).

The evidence and analysis step involved the gathering of data in order to inform the value model interactions between attributes, and between attributes and value. Data was gathered on subsystems such as the motor, battery, gear assembly, etc. The data collected involved key attributes important to that subsystem and that would impact the identified system level attributes. For example, for the motors, different COTS systems were investigated and their characteristics such as rotational speed, power draw, cost, etc. were recorded.   The motor subsystem had the most data available, while data for the other subsystems was limited due to the small mass desired for the Marsbee. Regressions were formed between the different characteristics of the Motor subsystem to determine if relationships exist, indicating that mass and cost for the alternatives examined (and where data was available) have a weak negative correlation. This weakness was likely due to the narrow band of alternatives examined. This information was used to better understand the attributes and their influences within the value model.

The final step, stakeholder preference elicitation, was performed by developing and conducting a questionnaire, found in Appendix B. The questionnaire included both scale questions and open-ended questions.   The questionnaire was open for all members of the Phase I research team to participate.
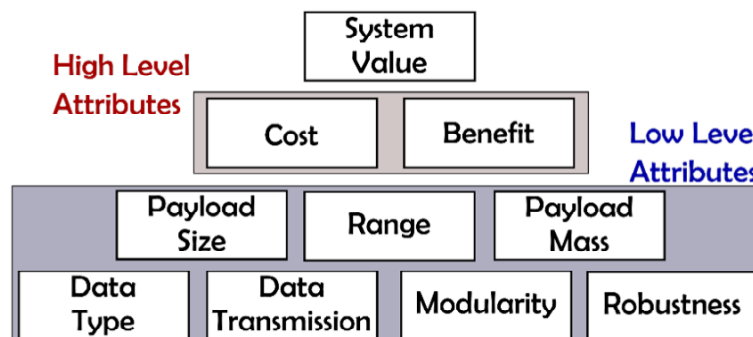
Figure 33. The pseudo-value model generated by templating step.

Four sections of the questionnaire were analyzed using SPSS25 to understand how the Marsbee team answered the questions. These sections were subsystem quality, system quality, project specific, and mission types. The statistical tests conducted were descriptives, frequencies, and non-parametric test (chi-square). Descriptives were used to observe the mean, median, mode, and standard deviation for each question. Frequencies were used to understand the distribution for each question with respect to the scales. Lastly, the non-parametric tests were used to identify statistically significant results. When using chi-square, the null hypothesis is that the population is equally distributed. Whenever the distribution varies vastly from the null-hypothesis, then that observation can be considered to be statistically significant.

6.2.1 Subsystem Quality

The subsystem quality section was composed of 13 questions (Appendix A.1). The subsystem quality focused on understanding the team's preferences in regards to the subsystem's main performance metrics, attributes, cost, and mission. The analysis showed that out of 13 questions, 4 were found to be statistically significant. Q16, on performance metrics importance, (M=2.00 and SD=1.17) shows how the responses varied across the scale, with the team selecting extremely important and very important a total of 76.5%, $X^2(4)$ =9.8, p=0.045. Q17, on subsystem attributes, (M=2.12 and SD=1.22) shows a noticeable difference between the team selecting very important compared to any of the other options, the team selected extremely important and very important a total of 82.4%, $X^2(3)$ =9.12, p=0.028. Q18, on subsystem robustness, (M=2.06 and SD=1.14) shows the same pattern as Q17, with the team selecting extremely important and very important a total of 76.5%, $X^2(4)$ =9.77, p=0.045. The last question that yielded statistically significant results was Q22. Q22, on subsystem efficiency, (M=2.24 and SD=1.09) shows the same pattern as Q16 and Q17, with the team selecting extremely important and very important a total of 70.6%, $X^2(4)$ =9.77, p=0.045. From the subsystem quality analysis, it can be inferred that the team's main concerns in regards to this portion of the questionnaire were performance metrics, attributes, robustness, and efficiency.

6.2.2 System Quality

The system quality section was composed of 13 questions, the last one being a ranking question (Appendix A.2). A total of 5 questions were found to be statistically significant. Q31, on system robustness, (M=2.00 and SD=0.791) the team selected extremely important and very important a total of 82.4%, $X^2(3)$ =11.5, p=0.009. Q32, on system reliability, (M=1.71 and SD=0.588) the team selected extremely important and very important a total of 94.1%, $X^2(2)$ =7.18, p=0.028. The team also did not select either slightly or not at all important. Q35, on system efficiency, (M=1.65 and SD=0.606) the team selected extremely important and very important a total of 94.1%, $X^2(2)$ =6.12, p=0.047. The team did not select slightly or not at all important in Q35, like Q32. Q37, on system efficacy, (M=1.88 and SD=0.600) the team selected extremely important and very important a total of 88.2%, $X^2(2)$ =7.88, p=0.019. The team did not select slightly or not at all important in Q37.

Q41 was the ranking question, where the team was asked to "rank order the following system characteristics (robustness, reliability, maintainability, availability, efficiency, profitability, efficacy, and resilience), with the top characteristic being most important to you and the bottom characteristic being the least important". Out of the characteristics listed, two were found to be statistically significant: robustness and profitability. Robustness, Q41_1, (M=2.20 and SD=1.61) was ranked in the top 3 a total of 80.0%, X^2(5) =12.6, p=0.027. Profitability, Q41_6, (M=6.93 and SD=2.19) was ranked in the top 3 a total of 13.3%, X^2(4) =26.7, p=0.00. Profitability was ranked 8th by the majority of the team, 73.3%. From the system quality analysis, it can be inferred that the team's main concerns were reliability, efficiency, efficacy, and robustness. The system qualities, efficiency and robustness, were preferred in the subsystem quality section as well. The characteristic that was found to have the least importance to the team, at this point in the design, was found to be profitability.

6.2.3 Project Specific

The project specific section was composed of 32 questions (Appendix A.3). These questions focused on understanding the team's preferences in regards to the design of the system. Four questions were found to be statistically significant. Q65, on constant communication between the rover and all of the Marsbees, (M=2.82 and SD=0.951) the team selected extremely important and very important a total of 35.3% compared to selecting moderately important 47.1% of the time, X^2(4) =10.9, p=0.027. Q73, on the Marsbee having 2 wings, (M=4.24 and SD=0.970) the team selected extremely important and very important a total of 5.9% compared to the selection of not at all important 52.9% of the time, X^2(3) =8.17, p=0.043. Q81, on the Marsbee equipped with chemical composition sensors, (M=3.24 and SD=0.752) the team selected extremely important and very important a total of 11.8% compared to selecting moderately important 58.8% of the time, X^2(3) =11.5, p=0.009. Q86, on the Marsbee equipped with magnetometer, (M=3.24 and SD=0.752) the team selected extremely important and very important a total of 11.8% compared to selecting moderately important 58.8% of the time, X^2(4) =9.77, p=0.045. This analysis showed more about what the team does not prefer in regards to the system and what they seem to be neutral about. The responses highlight that the team does not prefer having two wings on the Marsbee. This response may be due to design fixation since the team has only tested 4-winged flappers at the time of the questionnaires. The other statistically significant responses showed that the team seemed to not have preferences in regards to constant communication between the rover and all of the Marsbees as well as preferences for chemical composition sensors, and magnetometer. This may be due to the heavily aerospace engineering discipline working on the project and the disciplines focusing on their specific task.

6.2.4 Mission Types

The mission types section was composed of 11 questions (Appendix A.4). This section focused on identifying the team's preferences in regards to the types of missions the Marsbee will perform. Four questions were found to be statistically significant. Q88, on the mission to

map the local terrain (within 50 yards from the rover), (M=2.12 and SD=0.781) the team selected extremely important and very important a total of 76.5%, $X^2(3)$ = 11.0, p= 0.012. Q90, on the mission to learn more about the Martian atmospheric structure (winds, pressure, etc.), (M=2.47 and SD=0.624) the team selected extremely important and very important a total of 47.1% compared to selecting moderately important a total of 52.9%, $X^2(2)$ =6.12, p=0.047. The team did not select slightly or not at all important. Q91, on the mission to learn more about the Martian atmospheric composition (chemistry), (M=3.06 and SD=0.659) the team selected very important a total of 11.8% compared to selecting moderately important a total of 76.5%, $X^2(3)$ = 24.2, p= 0.000. The team did not select extremely important. Q92, on the mission to learn more about the Martian geology (land surface structure), (M=2.06 and SD=827) the team selected extremely important and very important a total of 76.5 %, $X^2(3)$ = 8.18, p= 0.043. The team did not select not all important. The team seemed to be interested in the missions to map the local terrain and to learn more about the Martian geology. The team seemed to not have strong preferences in regards to the mission to learn more about the Martian atmospheric structure and the mission to learn more about the Martian atmospheric composition. This may be due to the heavily aerospace engineering disciplines working on the project and the team members focusing on their specific task and related missions.

6.2.5 Summary

The Phase I questionnaire served two purposes: inform the researchers of areas to address in the next value model iteration, and to act as a pilot study for the Phase II questionnaire that will include higher level stakeholders, such as NASA. The results indicate that the pseudo value model formed in the templating step has many of the attributes necessary to capture the preferred missions suggested in the questionnaire results.

6.3   Evaluation of Alternative Systems to the Marsbee Concept

The findings from the three step process relate highly to the NASA Mission value models [55,113,114] previously researched in work funded by the NASA Systems Engineering Research Consortium. In the NASA Mission value model [113], three key benefit-side system attributes were identified: knowledge, prestige, and avoidance of catastrophes. The evidence and questionnaire findings have a strong emphasis on knowledge. This is seen in the rover path monitoring, flight duration, and high sensor capabilities. All of these desires relate to gathering knowledge directly, or enabling quicker knowledge gathering through another system. This also indicates the need to form a multi-system, mission-driven value model that includes a rover to interact with.

With Phase I indicating the primary benefit-side value of the Marsbee related to knowledge, more information is needed to form a mathematically useful value model. In particular, the worth of the data that the Marsbee will gather needs to be quantified, which will be an emphasis in the proposed Phase II work. Surveying of NASA stakeholders is necessary to determine this benefit-side value, due to the low amount of data available for path planning and atmospheric analysis on non-Earth planet missions.

6.4 Review of Lithium-Ion Battery Technologies for Mars Aerial Missions

Lithium-ion (Li-ion) batteries have been successfully used in Mars surface missions (Landers and Rovers) with excellent reliability [115–117] and will also be used for Mars aerial missions (e.g. Mars helicopter) [24,115]. They provide uninterrupted electric energy during launch, cruise or operation when external energy is not available [115,116]. Li-ion batteries are the dominant battery technologies for such missions mainly due to their high specific energy (Wh/kg), high energy density (W/L), low self-discharge and high efficiency [115,116]. However, big gaps still exist between currently used battery technologies and future Mars aerial mission needs. This report briefly summarizes the challenges for Mars aerial mission battery needs and reviews progress in addressing the challenges.

6.4.1 Challenges for Mars Aerial Mission Battery Needs

According to a recent assessment report on Energy Storage Technologies for Future Planetary Science Missions [115], future Mars missions would need rechargeable batteries to have high specific energy, long cycle life, long calendar life and low temperature operation capability. Mars aerial missions would also need batteries to have high specific power (3000 W/kg). Table 8 summarizes these key parameters of battery technologies for future Mars aerial mission (>2025). The parameters of batteries used in the Mars helicopter technology demonstrator (2018) and those used in the Mars Science Laboratory (MSL) Curiosity Rover (2011) are also listed for comparison. From the comparison, it is clear that big gaps exist in specific energy, specific power and low temperature operation capability. Indeed, the Mars helicopter demonstrator can only fly for 90 seconds at 0° C in worst case scenario [24], which is primarily due to limitations of its Li-ion battery.

Table 8. Future Mars aerial missions (>2025) battery needs and current status.

	specific energy (Wh/kg)	specific power (W/kg)	low temp. operation (^{o}C)	cycle life (cycles)	calendar life (years)
future Mars aerial mission (>2025) [115]	>250	3000	<-40	>1000 @>70% DOD	>5
Mars helicopter demonstrator (2018) [24]	131	1318 -1868	0	~500	>5 (estimate)
MSL Curiosity Rover (2011) [115–117]	97 - 141	<100 (estimate)	-20	>1500 @60% DOD	>5
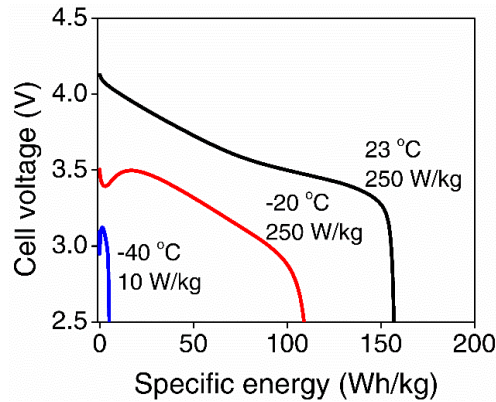
Figure 34. Specific energy of a high power 18650 Li-ion cell (Sony US18650VTC4) during constant specific power discharge at various temperatures.

Two characteristics of Li-ion batteries make it challenging to fill the gaps simultaneously. First, specific energy, specific power and life of Li-ion batteries decrease at subfreezing operating temperatures [118,119,128,129,120–127]. Figure 34 shows testing results of a high power 18650 Li-ion cell (Sony US18650VTC4, same type as those used in Mars helicopter demonstrator [24]). The specific energy is nearly 160 Wh/kg at 23 °C for specific power of 250 W/kg, but it drops to 109 Wh/kg at -20 °C for same specific power. It further drops to only 5.1 Wh/kg at -40 °C for specific power of 10 W/kg and doesn't work for specific power of 20 W/kg or higher. Earlier studies show that the specific energy could be 20 times lower at -40 °C than that at 25 °C [118,123] and the specific power could be 80 times lower [118]. Reduced specific power at low temperatures also makes charging difficult [130–138]. As shown in Figure 35 by Waldmann et al. [134], lithium deposition is much easier to occur during charging at lower temperatures, leading to shorter life and higher risk of safety failures. A study by Smart et al. [116] showed that the MSL 43 Ah Li-ion cells degrade 4-5 times faster at -20 °C than that at 20 °C.
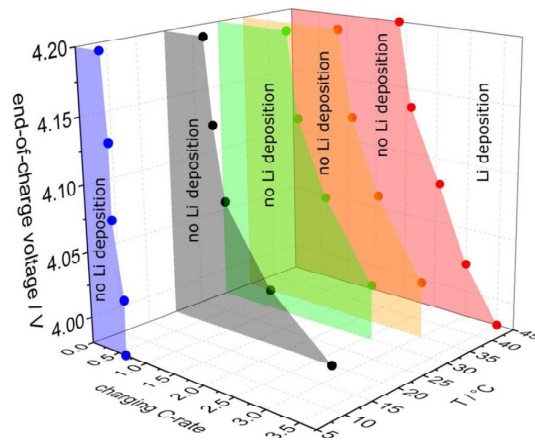
Figure 35. Experimental results by Waldmann et al. [134] **on effects of temperatures, charging C-rates and end-of-charge voltages on lithium deposition (plating) (Used with permission under the terms of the Creative Commons Attribution 4.0 License, CC BY.**

62

Second, specific energy and specific power are competing against each other as typically described in Ragone plots. Figure 36 shows Ragone plots of an 18650 cylindrical Li-ion cell at 20 ℃ and -20 ℃ measured by Zhang, Xu and Jow [122]. It can be seen that the Li-ion cell's specific energy significantly drops as its specific power increases, especially at low temperatures. When operating at -20 ℃, the Li-ion cell could deliver usable specific energy of more than 170 Wh/kg for specific power of ~5 W/kg, but it failed to deliver usable energy when the specific power increased to ~213 W/kg. The specific energy and specific power of a state-of-art Li-ion cell, Panasonic NCR-18650BF, at 20 ℃ and -40 ℃ are also shown in Figure 36. Compared with the cells tested by Zhang, Xu and Jow in 2006 [122], the state-of-art Li-ion cell has a much more enhanced performance at 20 ℃, with rated specific energy of 248 Wh/kg for specific power of ~250 W/kg [139]. However, its low temperature performance at -40 ℃ is still poor according to our preliminary testing. Its specific energy at was less than 5 Wh/kg when specific power was 5 W/kg and cutoff voltage of 2.5 V. It failed to work for specific power of 10 W/kg or higher.
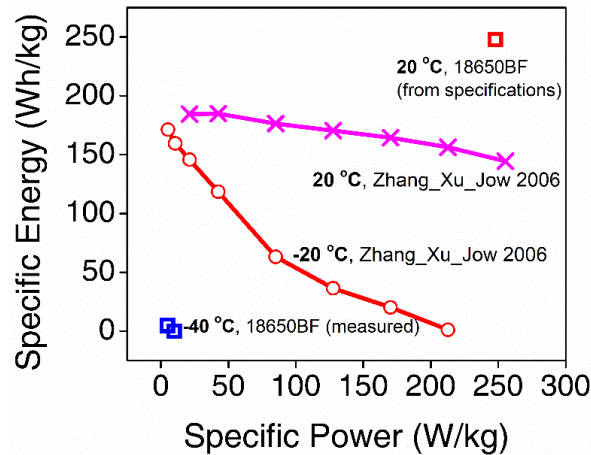
Figure 36. Specific energy vs. specific power of an early generation 18650 cell at 20 ℃ and −20 ℃ [122] and a state-of-art 18650 cell at 20 ℃ [139] and -40 ℃.

6.4.2   Progress in Addressing Li-Ion Battery Low Temperature Challenge

As described above, significantly reduced specific energy, specific power and cycle life at low temperatures is a critical challenge for Mars aerial mission batteries. It is also a challenge for automotive applications in which high energy, high power, and long life in a wide range of temperatures are desired [140]. Therefore, great efforts have been made in addressing the low temperature challenge for both applications. Two main approaches have been actively taken: (1) development of low temperature electrolyte, (2) preheating of Li-ion battery. Hybridization of Li-ion battery with high power supercapacitors are also explored for automotive applications [141], but may not be suitable for Mars aerial missions due to system and control complexity.

The poor performance of Li-ion batteries is attributed to sluggish reaction kinetics, slow lithium diffusion, reduced electrolyte conductivity, and increased solid-electrolyte interface (SEI) resistance at low temperatures [118,120,123,124,126,129,142–145]. Electrolyte plays a

role in most of these factors. Therefore, developing electrolyte for low temperature operation has been actively proposed in the past decades [119,125,153–162,130,163–170,146–152] with significant achievements.

Jet Propulsion Laboratory (JPL) has developed several generations of low-temperature electrolytes with continuous publications in the past two decades [130,146,155–159,147–154]. It is recently reported [115] that JPL has demonstrated specific energies of ~150 Wh/kg at −40°C and over 100 Wh/kg at −60°C to −70°C in commercial 18650-size cells with the JPL electrolytes. It is noted [115] that these tests are at low discharge rates which means low specific power.

Zhang, Xu and Jow et al. [119,125,160,161] also did extensive work on low-temperature electrolytes such as using $LiBF_4$ salt instead of $LiPF_6$ and adding ester/carbonate solvents. In addition, they extensively characterized performance of Li-ion cells [120–122,171,172] at low temperatures, in particular using electrochemical impedance spectroscopy (EIS) to analyze the limiting factors. Jow et al. [173,174] also investigated factors limiting charge transfer kinetics in Li-ion batteries, including the effects of electrolyte additives on low temperature performance.

Rustomji et al. [168] recently reported novel liquefied gas electrolytes based on fluoromethane (CH_3F) and demonstrated a high discharge capacity retention of 60.6% at –60°C on a Li cobalt oxide ($LiCoO_2$) cathode, yet the discharge rate is still quite low (C/10).

More recently Dong et al. [170] reported an ethyl acetate-based electrolyte with ionic conductivity of 0.2 mS cm^{-1} at −70 °C and demonstrated feasibility with organic polymer electrodes, but conventional Li-ion battery electrodes don't work with such electrolytes at −70 °C due to sluggish solvation/desolvation of lithium ions.

Because Li-ion batteries perform quite well around room temperatures, their performance would recover if they are preheated from low temperatures before operation. Indeed, this preheating strategy has been widely used in automotive applications [175,176], even in early generation hybrid electric vehicles using NiMH batteries [177,178]. But it may take 50 minutes for the core temperature of a large EV battery pack to reach 25 °C from 0 °C [175]. Therefore, the challenge of this strategy is how to preheat batteries quickly, efficiently and safely. With active research on this topic, great progress has been made.

First of all, various heating strategies have been proposed and investigated through modeling [178,179]. It is found that internal heating is more effective than external heating [178,179], which can be attributed to the low thermal conductivity of battery materials [180–183].

Second, different internal heating methods, including internal core heating through alternating currents (AC) [178,184–188] and mutual pulse heating [189], are experimentally investigated. It is confirmed that these methods are effective in recovering Li-ion battery performance at low temperatures. To warm up a Li-ion cell from around -20 °C to above 0 °C, the AC internal heating would typically take 10-15 minutes and the mutual pulse heating takes 2-3 minutes [189].

Recently Wang et al. [190–196] reported a novel Self-Heating Li-ion Battery (SHLB)

structure that has an embedded nickel foil heater as shown in Figure 37a [191]. At a low temperature the switch is turned on and electrical current flows through the nickel foil to generate heat to warm up the cell (heating mode). When warm enough, the switch turns off and the SHLB cell operates like a normal Li-ion cell. It takes ~12 seconds for an SHLB cell to warm up from -20 °C to above 0 °C and ~37 seconds to warm up from -40 °C [191]. This method works much faster than previously reported internal heating methods because the nickel foil greatly enhances the heat generation rate, especially as the cells warm up and less heat is generated from reactions. The self-heating process consumes 5.4% of energy to warm up from -40 °C for experimental SHLB cells with specific energy of 170 Wh/kg, but it could significantly increase specific power of Li-ion cells as shown in Figure 37b and the energy consumption for self-heating would be only 2.3% for future Li-ion cells with specific energy density of 400 Wh/kg. Such high specific power performance could not only enable high utilization of Li-ion cell specific energy for longer driving range [193], but also enable 3.5C fast charging at temperatures as low as -50 °C [196].

Figure 37. a) Schematic of SHLB cell structure with embedded nickel foil and a switch between positive terminal and activation terminal [191] (used with permission from Elsevier), b) Comparison of specific power between SHLB cell and baseline case [190] (Reproduced with permission from Springer Nature).

While great progress has been made in preheating Li-ion batteries to recover performance for low temperature operation, applications of the strategies to Mars aerial vehicles would require novel and great efforts due to extra hardware needs for thermal control.

6.4.3 Progress in Addressing Li-Ion Battery Energy-Power Tradeoff Challenge

Batteries for Mars aerial missions would require simultaneous high specific energy (for long operation time) and high specific power (for acceleration and speed). In conventional designs, electrodes are made thicker to increase the amount of active materials in Li-ion cells for higher specific energy, but their specific power performance becomes lower than thinner

electrodes [197]. Electrodes can be made thinner for higher specific power, then the specific energy would be lower. Therefore, it is impossible to achieve simultaneous high specific energy and high specific power by simply optimizing electrode thickness.

The power or rate performance of a Li-ion cell is essentially limited by its internal resistance. The internal resistance comes from multiple sources including ionic transport in electrolyte through porous and tortuous electrodes, electronic transport through electrodes and current collectors, solid-state lithium diffusion in electrode particles, and interfacial kinetics [121,126,197,198]. Modeling results [126,198] show that ionic transport in electrolyte and solid-state diffusion play important roles in power performance of Li-ion cells, especially at low temperatures.

Various strategies and methods have been proposed in recent years to achieve simultaneous high specific energy and high specific power. Reducing electrode particle size, such as using nanostructured materials [199–202] to reduce solid-state diffusion length, has been extensively explored. Enhancing interfacial kinetics by improving electrolytes and/or electrodes is also found effective [145,173,174]. Using carbon nanotubes to form a three-dimensional conductive network [203] is reported as very effective in reducing electronic resistance and enhancing rate/power performance.

More notably, great efforts have been made to reduce ionic transport resistance in recent years [204,205].

First of all, reducing electrode tortuosity is found to be an important strategy by both modeling [206] and experiments. In conventional Li-ion cells, electrode particles are randomly packed forming porous and tortuous channels in which liquid electrolyte is filled for ionic transport. The tortuosity of such electrodes is measured to be up to 5 for cathodes and 6-8 for graphite anodes [207–209]. Such high tortuosity makes effective transport length of ionic transport much longer than electrode thickness, execrating the mass transport limitation in thick electrodes. Developing electrodes with low tortuosity, such as making straight channels, could therefore significantly reduce ionic transport resistance and enhance power performance. Various novel methods have been reported, such as using structured binder network during electrode extrusion and then removing the binder network by burning out to form straight channels [210], using a magnetic field to align magnetized rods as straight channel formers [211], using laser to perforate straight channels through electrodes [212], using co-extruding electrode fabrication technology [213], or by directly carbonizing the multi-channeled natural wood as highly conductive, lightweight and low-tortuosity 3D carbon framework [214].

Secondly, modeling studies show that the transference number of electrolyte salt has important effects on Li-ion battery power performance. Widely used $LiPF_6$ has a transference number of less than 0.4 [143]. This number being less than 1 would cause very non-uniform distribution of salt concentration during high C rate discharge and charge [126,215], which would further cause higher overall ionic transport resistance. Therefore, increasing the transference number is proposed as a promising approach to enhanced power performance by a recent modeling study [215]. But it is noted that enhancing the transference number of

electrolytes is very challenging as other important properties like conductivity could be influenced [215,216].

Thirdly, optimized porosity distribution has been proposed to reduce ionic transport resistance by modeling studies [217–219], yet the effectiveness is still under debate [206].

While most of the novel methods are still in early stages and may cause challenges in large scale manufacturing, they provide promising ways to achieving simultaneous high specific energy and high specific power in the future.

6.4.4 Progress in Other Aspects of Li-Ion Batteries Related to Mars Aerial Missions

In addition to the low temperature challenge and the energy-power tradeoff challenge, progress in many other aspects of Li-ion batteries could contribute to Mars aerial missions.

First, significant progress has been made in increasing specific energy of Li-ion batteries. The main approach is through innovations in materials, including silicon-based anodes [220,221], lithium metal-based anodes [222,223] and high capacity cathodes [224–226] to increase specific capacity (mAh/g) of electrodes, as well as high voltage electrolytes [227,228] to increase operating voltage of Li-ion cells. With such approaches, the specific energy of Li-ion batteries could increase to 400 Wh/kg [35] or even 500 Wh/kg [229].

Second, the concept of a multifunctional structural battery has been explored and demonstrated [230–233]. In this approach, a Li-ion battery not only stores energy, but also works as a structural component of the system, or even works as a sensor [234]. While the specific energy of the Li-ion battery itself in this approach may be not very high due to the need of structural strength, the specific energy from the system perspective could be advantageous due to mass savings through integration of a battery within the system.

Third, wireless charging of Li-ion batteries has been increasingly explored and demonstrated in both electric vehicles [235–240] and unmanned aerial vehicles [241–244]. Analysis of an all-electric bus system shows that a wirelessly charged battery can be downsized to 27–44% of a plug-in charged battery [235]. Compared with plug-in charging or battery swap, wireless charging would make automatic charging much more convenient, especially for Mars aerial missions in which automation is needed. Therefore, wireless charging could play a very important role in efficient and reliable Mars aerial missions.

Fourth, direct solar charging of Li-ion batteries has been explored, such as by combining dye-synthesized solar cell technology with lithium-ion materials [220,245,246]. The total energy conversion efficiency is still very low (less than 1%) [245,246], making it not suitable for short term applications, but research is in this area is very active [247,248] which could possibly lead to much greater increase of energy efficiency. If direct solar charging could be made efficient, combinations of this concept with the structural battery concept, as mentioned above, could free aerial vehicles from base charging stations, thus offering more autonomy to individual or group aerial vehicles.

Last, it is worth noting that a recent study [249] showed that some commercially-off-the-shelf (COTS) 18650 Li-ion cells survived temperatures as low as −160 °C for 14 days,

demonstrating the robustness of Li-ion battery technologies. With further progress in the other techniques mentioned above, Li-ion battery technologies can be expected to work under extreme cold environments in Mars.

6.4.5 Discussion on Mars Aerial Mission Battery Needs from System Perspective

As briefly reviewed above, great efforts have been made to enhance specific energy, specific power, cycle life, calendar life, and low temperature operation capability of Li-ion batteries. Great achievements have been obtained in the past two decades and greater ones can be expected in the years and decades to come [115,140,205]. But achieving targets in all five parameters simultaneously would be challenging due to the fundamental challenges of low temperature effects and energy-power tradeoff. While it is critically important to directly address the challenges from the battery perspective, it is worth discussing the challenges from an aerial vehicle system perspective. The specific energy of Li-ion cells decreases significantly with the specific power at low temperatures, as shown in Figure 36 [122]. Reducing the specific power need of aerial vehicles could therefore make much better use of Li-ion battery specific energy. Our preliminary testing of Sony US18650VTC4 Li-ion cell at -20 °C showed that the cell failed to work for a specific power of 1000 W/kg and above, but could deliver more than 60% of available energy for specific energy of 750 W/kg and below. Alternative vehicle concepts that are less demanding in specific power needs, such as nature-inspired Marsbee [66,67,98], could enable operation at lower temperatures and longer flight time with similar battery technologies.

Li-ion batteries have been successfully used in Mars surface missions with excellent reliability due to their many advantages, including high specific energy, long cycle, and long calendar life. But as they are to be used in future Mars aerial missions, which also demands extremely low temperature operation (<-40 °C) and high specific power (3,000 W/kg), their characteristics of reduced performance at low temperatures and energy-power tradeoff would make it very challenging to meet all the technical targets simultaneously.

As reviewed, great achievements have been made to address the challenges in the past two decades. In particular, development of low-temperature electrolytes and preheating methods have enhanced low temperature performance significantly, and engineering electrode designs to minimize transport limitations shows promising approaches to simultaneous high specific energy and high specific power. Progress in other aspects of Li-ion batteries, such as high specific energy materials, multifunctional structural battery, wireless charging and direct solar charging would also help future Mars aerial missions. However, further efforts are needed to meet the technical targets of future Mars aerial mission battery needs, especially in enhancing specific power performance at low temperatures (<-40 °C).

Based on specific energy and specific power behaviors of Li-ion batteries at low temperatures, it is proposed to address the battery challenges also from the Mars aerial vehicle system perspective. Alternative Mars aerial vehicle designs that are less demanding on battery specific power could make much better use of battery specific energy at low temperatures, thus significantly increasing flight time with similar battery technologies.

6.5 Review of Sensors for Atmospheric Data Collection

In this section, we describe existing small-scale sensors and sensing approaches within the weight, volume, and power limitations of the Marsbee system. Given mass considerations especially (<5 g), the number of commercially-off-the-shelf (COTS) solutions is minimal. This section describes those sensor options, identifies some likely areas of development in the next decade, and outlines some considerations for implementation and subsequent data processing. This section is broken down by presumed remote sensing goal: land surface structure, land surface composition, and atmospheric composition.

6.5.1 Land Surface Structure

Commonly employed approaches to determine the three-dimensional structure of surfaces, particularly using satellite, airborne, and unmanned aerial system (UAS) platforms, include: interferometric synthetic aperture radar (C/X/L-band SAR), light detection and ranging (LIDAR), and photogrammetric manipulation of optical imagery. Given the considerations of weight, power, and volume listed above, focus here is on the use of photogrammetric techniques using optical imagery. For Marsbee this is made possible because of the small scale of optical sensors with options for wide and narrow fields of view. Moreover, most CMOS sensors can capture a portion of the near-infrared electromagnetic spectrum. This allows for some composition studies (described in the next section) using the same sensor that is simultaneously capturing data for terrain characterization. Some examples of such sensors include:

- ON Semiconductor Python 2000 series, for NIR
- ON Semiconductor AR1820HS, for RGB

The other solution in this realm is to use a "time of flight" proximity and distance sensor which essentially consists of two cameras doing real-time 3D rendering or distance estimations. One product which is an example of this is:

- Texas Instruments, OPT3101

Considerations here include the desired pixel size or spatial resolution, which can be determined by typical Marsbee flight altitude paired with appropriate sensor choice (FOV). Additionally, video (instead of still frame) option would likely have some benefits and would still make image stitching easy in post-processing.

6.5.2 Land Surface Composition

After review of the current state of hyperspectral imaging spectrometers, it is evident that they are not currently applicable for use on a Marsbee system, due primarily to weight limitations. Most solutions under development commercially are aimed at integration onto larger UAS platforms like quad- and hex-copters [250]. Some examples of these types of systems include Resonon, HySpex, and BaySpec.

The above noted COTS systems have a minimum weight of 100 g and range upwards to several kg in weight. Most of these systems record 10-150 channels in the VNIR (450-950 nm) range. It is likely that these imaging sensors will continue to shrink in mass over the next decade and thus may be appropriate solutions in the future.

A more feasible current approach is to use a hyperspectral spectrometer and to composite the readings into a surface. This would require flight at a known altitude to correspond to the field of view of the spectrometer, and significant post-processing to create the multi-dimensional hyperspectral image. The benefit to this approach is the reduced mass of the sensor, down to approximately 5 grams in the sensor (e.g. Hamematsi C12880MA), which continues to record in the VNIR at down to 14 nm bins.

Thermal sensors can provide an additional level of information for land surface composition. Most cooled thermal sensors have too great a mass for use on the Marsbee platform. An uncooled option such as the FLIR Lepton is a mass-conservative option which records in the longwave LWIR (8-14 microns). This system has a mass of 0.9 g, making it easily within the Marsbee mass specifications.

6.5.3   Atmospheric Structure

Barometric pressure and temperature are the two most critical sensors in this category and are also both relatively light in mass and commonly integrated into UAS, IoT, and a variety of micro applications. Bosch pressure sensors are compact, lightweight (<0.10 gram), and dependable. One item to note in selecting the exact sensor to be used is that it must be sensitive to lower atmospheric pressures than on Earth. Commonly sensors developed for applications operate in the 50-150 kPa range but the sensor to be chosen for Marsbee should operate much lower, perhaps in the 0.25-1 kPa range and with sub-Pa accuracy. Examples from Bosch (pressure) and Texas Instruments (temperature) are some key examples of appropriate types of sensors to integrate.

Finally, to model atmospheric structure well, information is required about wind speed and direction. Typically anemometers are used to estimate these parameters fairly accurately, but such instruments are generally not appropriate for most UAS and certainly not Marsbee. Recent developments in digital anemometers and miniaturization have made advances (e.g. by Apptech TriSonica Mini), however at 50 g such sensors remain unable to be integrated into the Marsbee system.

A more effective solution to the question of wind speed and direction is to use the IMU and power distribution data from the Marsbee itself. Following Tomic *et al.* [251] and others, multiple groups including MeteoMatics have been working on using such internal data already being collected to post-process and generate wind field data. The ultimate accuracy of this approach is yet unclear, however this area of research is very promising and stands to eliminate the need for separate sensors for these wind measurements.

7   PATH-PLANNING AND CONTROL ALGORITHMS FOR 3D TOPOGRAPHIC MAPPING

The topography of Mars has several benefits in future mission planning for landing spacecraft and image distortion correction, among other research objectives. The Mars Orbiting Laser Altimeter (MOLA) mission greatly improved the topography map of the surface but was limited to an uncertainty of roughly eight meters [252]. The only precise topography knowledge about the surface comes from four rovers, two of which are inactive, and have covered only a small portion of the surface area of Mars.

Mapping and exploring Mars presents several challenges. Existing rovers are ground vehicles, incapable of traversing steep or dangerous terrain. Flying vehicles avoid this restriction, but special attention must be placed on their motion planning in this uncertain environment. Humans cannot directly give commands to the vehicles due to the signal time delay between Mars and Earth. Even if humans are present on Mars, they can only provide sub-optimal motion commands on a small scale. These challenges motivate an autonomous approach to 3D mapping and exploration in uncertain and complex environments for a flying vehicle near the surface of Mars.

The study of 3D mapping and autonomous exploration has received substantial attention for applications on Earth. Occupancy grid mapping in 3D is a popular approach where an environment is decomposed into evenly-spaced cubic grid cells, where each cell is assumed as occupied or free [253,254]. The goal is finding the probability of each cell being occupied. An exact solution of this probability was recently found by the CO-I Lee and his group using the stochastic properties of onboard sensors directly [255,256]. Using an exact occupancy grid mapping algorithm in 3D, the topological information of the surface of Mars can be accurately computed in real-time.

Next, the robot must determine motions based on how much mapping knowledge it expects to gain, known as autonomous exploration. The most popular approach to this problem is known as frontier-based exploration [257–259]. The main idea is that the robot moves through previously-mapped free space toward the boundary between free space and uncertain space, known as a frontier. The robot takes measurements of this frontier, thereby pushing back the boundary. This process is repeated until the map is well-known. Despite the intuitive nature of this approach, there is no measure or prediction of how these robotic actions improve map information. Thus, frontier-based approaches rely on a heuristic rule, and are inherently suboptimal.

In contrast, entropy-based autonomous exploration approaches seek to minimize future map uncertainty. Shannon's entropy is a measure of map uncertainty; since minimizing future map uncertainty is equivalent to maximizing map information gain, these approaches select robotic actions to minimize entropy [260]. In [261], an exact solution to expected entropy was developed, and in [262], this concept is extended to 3D office-like environments assuming the environment can be approximated as vertically-uniform. Similarly, [263] simplifies tasks by decomposing the 3D space into rooms.

While these approaches can be effective for buildings, they are incompatible with the surface of Mars, which has complicated geological features that require careful consideration. Here, we propose a 3D autonomous exploration algorithm that considers the 3D probabilistic occupancy grid map and sensor properties explicitly. The complicated and uncertain geometry of the surface of Mars is captured by aerial mapping because this approach can cover a large area effectively. An onboard depth sensor, such as a 3D laser scanner, gathers range measurements to determine the occupancy probabilities of 3D grid cells. Then, collision-free future pose candidates are considered. The predicted negative entropy changes from measurements passing through 3D space are maximized while also considering travel costs. The aerial vehicle then uses Dijkstra's search in 3D for collision-free motion planning, and the complete process follows a receding-horizon framework for consistently using updated information. The proposed optimal approach is designed specifically for real-time exploration of the surface of Mars, where the flying robot mostly maps occupied space below the vehicle but is also capable of looking ahead to capture steep and quickly-changing terrain. In short, the proposed autonomous exploration approach predicts future map uncertainty in 3D space to determine optimal actions that maximize map information gain while avoiding collisions.

7.1   Problem Definition

In this section, we define the 3D occupancy grid map probability and expected map entropy from a future measurement.

7.1.1   Probabilistic Occupancy Grid Mapping in 3D

First we define the map, measurements, and poses as follows. Let 3D map m be composed of n_m evenly-spaced cubic grid cells with edge length α. For index $i \in \{1, 2, \ldots, n_m\}$, let $\mathbf{m}_i$ and $\bar{\mathbf{m}}_i$ be the events that the i-th grid cell are occupied and free, respectively, where each cell occupancy is assumed static, binary, and independent of other cells. At the t-th time step, we assume a known current pose $X_t = \{x_t, R_t\}$ such that $x_t \in \mathbb{R}^3$ is a 3D location and $R_t \in \mathrm{SO}(3)$ is the 3D attitude, and history of poses $X_{1:t-1}$ is assumed known as well. The configuration space of the attitude corresponds to the special orthogonal group, or SO(3), and it is composed of 3 by 3 orthogonal matrices with a determinant of one. Considering that most modern sensors return scans with multiple measurement rays, let measurement ray z be a single depth measurement belonging the most recent scan Z_t, and let $Z_{1:t-1}$ be the history of measurement scans.

Next, we present recent contributions to occupancy probability determination from [255,256], which uses a simplified result of a complicated Bayesian probability. Let a temporary reduced map $r \subset m$ be composed of n_r cells along measurement z, indexed by increasing distance from the current pose X_t. The cells of r are easily acquired through 3D ray casting: the measurement ray vector from x_t intersects 3D grid cells, and the associated depths are calculated with Euclidean distance. Let $\mathbf{r}_{k+}$ be the event that the k-th cell of reduced map r is the closest occupied space, and the *forward sensor model* $p(z \mid \mathbf{r}_{k+}, X_t)$ is known from the

stochastic properties of the depth sensor (e.g. a Gaussian distribution). Then, the probability of $\mathbf{r}_k$ based on z is commonly referred to as the inverse sensor model, which can be written compactly as

$$P(\mathbf{r}_k \mid z, X_{1:t}, Z_{1:t-1}) = \eta \tilde{P}(\mathbf{r}_k \mid z, X_{1:t}, Z_{1:t-1}) \tag{31}$$

where η serves as a normalizer,

$$\eta = \left[\sum_{i=1}^{n_r+1} \left\{ \prod_{j=0}^{i-1} \bar{\mathbf{P}}_j^- \right\} p(z \mid \mathbf{r}_{i+}, X_t) \mathbf{P}_i^- \right]^{-1}, \tag{32}$$

and the probability before normalizing is

$$\tilde{P}(\mathbf{r}_k \mid z, X_{1:t}, Z_{1:t-1}) = \mathbf{P}_k^- \left[\sum_{i=1}^{k-1} \left\{ \prod_{j=0}^{i-1} \bar{\mathbf{P}}_j^- \right\} p(z \mid \mathbf{r}_{i+}, X_t) \mathbf{P}_k^- \right] + \left\{ \prod_{j=0}^{k-1} \bar{\mathbf{P}}_j^- \right\} p(z \mid \mathbf{r}_{k+}, X_t) \mathbf{P}_k^-, \tag{33}$$

where a priori probability is $\mathbf{P}_k^- = P(\mathbf{r}_k \mid X_{1:t-1}, Z_{1:t-1})$, its complement is $\bar{\mathbf{P}}_k^- = 1 - \mathbf{P}_k^-$, $P(\bar{\mathbf{r}}_0 \mid X_{1:t-1}, Z_{1:t-1}) = P(\mathbf{r}_{n_r+1} \mid X_{1:t-1}, Z_{1:t-1}) = 1$ for convenience, and $p(z \mid \mathbf{r}_{(n_r+1)+}, X_t)$ represents the forward sensor model of a maximum sensor reading. By using repeated terms in Eqs. (32) and (33), this equation has linear complexity with n_r for all cells in reduced map r, amortized to $\mathcal{O}(1)$ for each cell, which is easily computed in real-time.

In short, an exact solution to occupancy probability can be computed from the most recent measurement in real time provided the stochastic sensor properties and a priori probabilities. This solution avoids common approximations or machine learning, and simplifies future measurement predictions, described next with expected entropy calculation.

7.1.2 Expected Measurement Ray Entropy

Here we define entropy as a measure of 3D occupancy grid map uncertainty. Shannon's entropy [260] for the i-th cell and the complete map are

$$H(P(\mathbf{m}_i)) = -P(\mathbf{m}_i)\log P(\mathbf{m}_i) - P(\bar{\mathbf{m}}_i)\log P(\bar{\mathbf{m}}_i)$$

$$H(P(m)) = \sum_{i=1}^{n_m} H(P(\mathbf{m}_i)) \tag{34}$$

respectively. This serves as an effective measure because Eq. (34) is minimized as $P(\mathbf{m}_i)$

approaches 0 or 1 (smallest uncertainty), but is maximized when $P(\mathbf{m}_i) = 0.5$ (largest uncertainty).

Next, we define a candidate future pose. Let candidate location $x_c \in \mathbb{R}^3$ be the 3D location of a future pose, and $R_c \in \mathsf{SO}(3)$ be the candidate attitude, such that the candidate future pose is $X_c = \{x_c, R_c\}$. Consider measurement z_c, which is a possible measurement from pose X_c. Since candidate location x_c and the grid cell locations are known, the distance from the robot to the k-th cell, namely $z_{c,k}$ is easily solved with 3D ray casting.

Finally, we present the fundamental equations to predict map information gain from a potential future measurement based on [261]. The measurement ray z_c can only change the cell entropies along its ray, and therefore the reduced map $r \subset m$ is used, similar to mapping. The history of poses and measurements is required for subsequent equations as they affect a priori probabilities, but are removed below for simplicity. The entropy after z_c updates the map is predicted as

$$\mathrm{E}[H(P(r \mid x_c, z_c))] = \sum_{k=1}^{n_r+1} \left\{ H(P(\mathbf{r}_k \mid x_c, z_{c,k})) P(z_{c,k} \mid x_c) \right\} \tag{35}$$

The first term of the summand, namely $H(P(\mathbf{r}_k \mid x_c, z_{c,k}))$, is simply the entropy Eq. (34) of the inverse sensor model Eqs. (31-33). The second term of the summand, namely $P(z_{c,k} \mid x_c)$, can be solved by combining Eq. (32) as

$$P(z_{c,k} \mid x_c) = \frac{p(z_{c,k} \mid x_c)}{\sum\limits_{i=1}^{n_r+1} p(z_{c,i} \mid x_c)} = \frac{\eta_{c,k}^{-1}}{\sum\limits_{i=1}^{n_r+1} \eta_{c,i}^{-1}} \tag{36}$$

where $\eta_{c,k}$ refers to the normalizer based on the measurement $z_{c,k}$.

In short, the expected entropy along a ray is calculated by decomposing the measurement into possible range values with 3D ray casting. Then, we find the entropy from each range value, multiplied by the probability of that outcome using terms from the inverse sensor model. The computational complexity is $\mathcal{O}(n_r^2)$, but this can be reduced substantially by neglecting highly-improbable measurement outcomes, shown in [261].

7.2 Autonomous Exploration in Complex 3D Environments

In this section, we propose how multiple measurement rays in 3D can determine map information gain from a pose candidate. Then, we show how a collision-free trajectory is determined with a 3D Dijkstra's search. Finally, we combine 3D information gain and travel costs into a single optimization.

7.2.1 Map Information Gain in 3D

The expected entropy for an arbitrary 1D ray spanning 3D space can be calculated with Eq. (35) and Eq. (36) in a computationally tractable manner. However, computing the expected entropy from multiple rays simultaneously has exponential complexity, and is therefore computationally intractable. Additionally, numerous rays of a single scan commonly intersect the same grid cells, making consideration of every measurement ray unnecessary.

Instead of considering expected entropy from a complete scan, we propose a real-time solution that selects sample measurements to determine an optimal attitude at each candidate pose and the associated map information gain. We assume the vehicle is capable of level flight, so the third axes of the world and body are aligned (Fig. 38), so R_c can be expressed as

$$R_c = \begin{bmatrix} \cos\psi & -\sin\psi & 0 \\ \sin\psi & \cos\psi & 0 \\ 0 & 0 & 1 \end{bmatrix}, \quad 0 \leq \psi < 2\pi \tag{37}$$

where ψ represents the angle about the third body-fixed axis. The direction of a 3D measurement may also have a nonzero component in the vertical direction. This is achieved by rotating the sensor frame angle θ about the second sensor-fixed axis,

$$R_{c,\text{sensor}} = \begin{bmatrix} \cos\theta & 0 & \sin\theta \\ 0 & 1 & 0 \\ -\sin\theta & 0 & \cos\theta \end{bmatrix}, \quad -\frac{\pi}{2} \leq \theta \leq \frac{\pi}{2} \tag{38}$$

Combining these two rotation matrices, the measurement z with depth $\|z\|$ is expressed with respect to a frame fixed to Mars as

$$z(\psi,\theta) = \begin{bmatrix} \cos\theta\cos\psi & -\sin\psi & \cos\psi\sin\theta \\ \cos\theta\sin\psi & \cos\psi & \sin\psi\sin\theta \\ -\sin\theta & 0 & \cos\theta \end{bmatrix} \begin{bmatrix} \|z\| \\ 0 \\ 0 \end{bmatrix} = \begin{bmatrix} \cos\theta\cos\psi \\ \cos\theta\sin\psi \\ -\sin\theta \end{bmatrix} \|z\| \tag{39}$$

In short, unit vectors are acquired via Euler angles within certain sensor limits.

75

a.) General View   b.) ψ Rotation   c.) θ Rotation
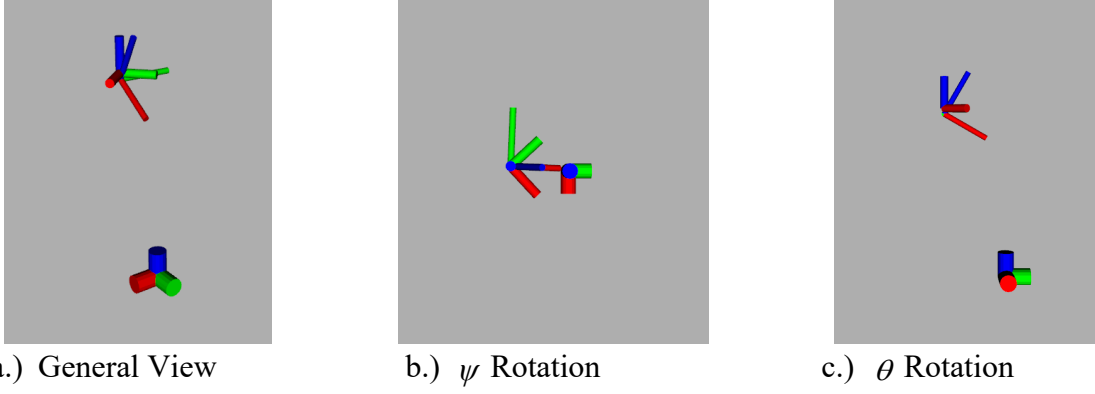
Figure 38. The three frames are shown with three axes (red: first axis, green: second axis, blue: third axis). The Mars frame (short and thick) is fixed to the planet. The body-fixed frame (medium thickness and length) is fixed to the camera frame (long and narrow). The rotation of ψ (b) represents the fixed camera yaw rotation and θ (c) represents the downward angle of the camera to capture the surface of Mars below the flying robot.

Next, we show how multiple 3D measurements provide an estimate for information gain. Let Ψ and Θ be the angular ranges for sensor field-of-view (FOV) in the horizontal and vertical directions, respectively. Within the sensor FOV, we select sample measurements for evaluating their expected information gains. Let the number of sample measurements be n_ψ and n_θ for horizontal and vertical rotations, respectively. Since R_c and the FOV are known, the set of sample measurement rays, namely $\mathcal{Z}(R_c)$, is known as well. Then, the expected information gain for a single measurement ray z from candidate position x_c and attitude R_c is the negative expected entropy change,

$$\mathcal{I}_{\text{ray}}(x_c, R_c, \psi, \theta) = \begin{cases} H(P(r)) - \mathrm{E}[H(P(r \mid x_c, z(\psi+\tilde{\psi}, \theta+\tilde{\theta})))], & \text{if } z(\psi+\tilde{\psi}, \theta+\tilde{\theta}) \in \mathcal{Z}(R_c), \\ 0, & \text{otherwise,} \end{cases} \quad (40)$$

where the mounting yaw $\tilde{\psi}$ and pitch $\tilde{\theta}$ of the sensor is a fixed rotation in the horizontal and vertical directions, respectively in that order, such that $-\pi < \tilde{\psi} \le \pi$ and $-\pi/2 + \Theta/2 \le \tilde{\theta} \le \pi/2 - \Theta/2$. A positive $\tilde{\theta}$ corresponds to rotating the depth sensor from a forward direction to a downward direction toward the surface of Mars. The expected information gain for the full scan is the summation of expected information gains for individual rays

$$\mathcal{I}_{\text{scan}}(x_c, R_c) = \sum_{i_\psi=1}^{n_\psi} \sum_{i_\theta=1}^{n_\theta} \mathcal{I}_{\text{ray}}\left(x_c, R_c, \frac{(2i_\psi - n_\psi - 1)\Psi}{2n_\psi}, \frac{(2i_\theta - n_\theta - 1)\Theta}{2n_\theta}\right). \quad (41)$$

Finally, Eq. (41) is computed for n_ψ possible attitudes when the robot is at location x_c,

76

one corresponding to each yaw angle ψ. Then, the optimal attitude at x_c is

$$R_c^* = \underset{R_c}{\mathrm{argmax}} \, \mathcal{I}_{\mathrm{scan}}(x_c, R_c).$$

(42)

In short, the expected information gain from each possible measurement ray is obtained using predicted entropy from Eq. (35) and Eq. (36). Then the expected information gain from all possible scans at a candidate location is calculated from Eqs. (40,41). Finally, the optimal attitude at this candidate location is found using Eq. (42).

7.2.2 Collision-free Trajectory in 3D

Next, we present a fairly straightforward application of Dijkstra's search to 3D occupancy grid mapping. First we reduced the number of grid cells to cubic blocks large enough for a robot to fit completely inside. Based on the occupancy probability of these blocks and their neighbors, we determine which cells are reachable, and what are their travel costs by building a cost map based on Dijkstra's algorithm.

Here we describe how a reduced map is generated for collision avoidance and motion planning. If the largest edge-to-edge distance of the robot, namely ρ, is not larger than the 3D grid cell size α, this step is unnecessary. Let $k \geq 1$ be an integer such that $k\alpha \geq \rho$ and $(k-1)\alpha < \rho$, i.e., k is the minimum number of grid cells in each dimension capable of fully-enclosing the robot inside this cube. Then, we decompose the complete probabilistic 3D into map m_{reduced}, which is composed of larger cubic cells that encompass k^3 cells from map m. Let $\mathbf{m}_{\mathrm{reduced},k}$ denote the k-th cell of m_{reduced} being occupied, and let $a_k \subset m$ be those k^3 cells from m composing this larger cell. Then, we apply an effective rule for collision-avoidance from [262] to obtain the probability of $\mathbf{m}_{\mathrm{reduced},k}$,

$$P(\mathbf{m}_{\mathrm{reduced},k}) = \begin{cases} \max_{i \in a_k} P(\mathbf{m}_i), & \text{if } \max_{i \in a_k} P(\mathbf{m}_i) \geq P_{\mathrm{thresh}}, \\ \min_{i \in a_k} P(\mathbf{m}_i), & \text{otherwise,} \end{cases}$$

(43)

where initial probability is $0 < P_{\mathrm{init}} < 1$ and the threshold probability is constrained to $P_{\mathrm{init}} < P_{\mathrm{thresh}} < 1$. This approach uses probabilities that have changed from P_{init}, and favors occupied cells to avoid risking collisions.

Next, we show how $\mathbf{m}_{\mathrm{reduced},k}$ is used in Dijkstra's search [264] for collision avoidance and motion planning. Defining $0 < P_{\mathrm{coll}} < 1$ as the acceptable probability of collision, every grid cell of m_{reduced} is considered a safe and unvisited node if its occupancy probability, and the occupancy probabilities of its neighbors (sharing a face, edge, or corner), are below P_{coll}. A cost map is built from the starting robot location by neighboring nodes, where the cost to travel to another node is based on Euclidian distance: a cell sharing a face is α away, a cell sharing an

edge is $\sqrt{2}\alpha$ away, and a cell sharing a corner is $\sqrt{3}\alpha$ away. Generating a cost map for all reachable cells in $\mathbf{m}_{\text{reduced},k}$ provides a collision-free travel cost for all reachable candidate pose locations. Once an optimal pose is selected, the path is easily found from the cost map using steepest descent.

7.2.3 Optimal 3D Pose

Here we present how an optimal pose is selected based on information gains at optimal attitudes and known collision-free travel costs. First, we show a function to account for travel costs, and then we account for these costs inside the optimization.

The proposed autonomous exploration follows a receding-horizon framework, meaning that optimal poses and trajectories are computed as quickly as possible, even if the robot has not reached the prior optimal pose. However, the computation is not instantaneous; let the distance d_{opt} denote the distance that the robot can travel between optimal pose updates. Then, we define a *bump function* loosely based on [265], defined as

$$\mathcal{B}(d) = \begin{cases} f_{\max}, & \text{if } 0 \leq d \leq d_{\text{opt}} \\ (f_{\max} - f_{\text{far}})\exp\{-\beta(d_{\text{opt}} - d)^2\} + f_{\text{far}}, & \text{if } d > d_{\text{opt}} \end{cases}, \tag{44}$$

where d is a travel distance along the cost map, $f_{\max} > f_{\text{far}} > 0$, and $\beta > 0$ is an exponential decay rate of the bump, which is illustrated in Fig. 39. The main idea is that when travel costs are low, the bump function is large, but the bump decreases with increasing travel cost.

Finally, we incorporate expected information gain and travel costs into a unified optimization. Given $d(x_c)$ from Dijkstra's cost map, the optimal candidate location is

$$x_c^* = \underset{x_c}{\operatorname{argmax}} \, \mathcal{I}_{\text{scan}}(x_c, R_c^*)\mathcal{B}(d(x_c)), \tag{45}$$

and therefore the optimal pose is $X_c^* = \{x_c^*, R_c^*\}$.

In conclusion, every reachable candidate pose is considered for its optimal attitude. The travel costs, acquired from Dijkstra's search, serve as input for the bump function, which prioritizes local trajectories to avoid costly map traversals. Then, the optimal candidate location is selected to maximize a combination of expected information gain and travel cost.
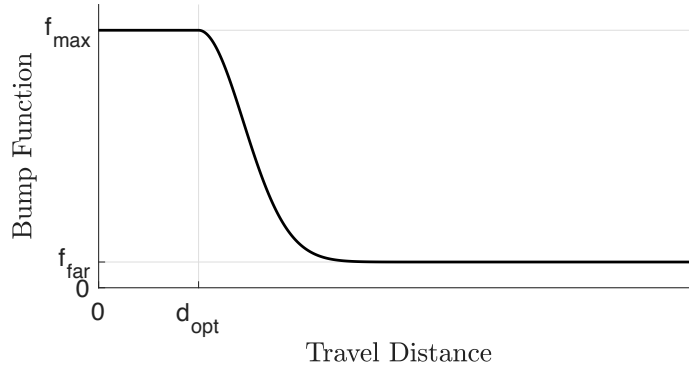
Figure 39. The bump function is multiplied to the objective function of Eq. (45) to prioritize local trajectories to avoid traversals across the map, where travel costs are determined using Dijkstra's algorithm. However, there is no time wasted up to d_{opt} because this distance may be achieved in the minimum exploration computation time.

7.3 Numerical Examples

In this section, we demonstrate the efficacy of the proposed 3D mapping and autonomous exploration with a simulated Mars environment. First we cover the software structure and parameters, then compare results using two different maps for entropy prediction.

7.3.1 Software

The mapping, exploration, and visualization processes communicate over the Robot Operating System (ROS) framework (Kinetic distribution), and Gazebo 8 serves as the simulator for the physical objects and measurements. There are two major programs, referred to as nodes in ROS, used during the simulation: mapping and exploration. The mapping node takes measurements from a 3D laser scanner and pairs those with the sensor transformation relative to Mars using the ROS Transform Message Filters package. Then, it builds a 3D probabilistic map using ray casting and the inverse sensor model Eqs. (31-33). The mapping node sends updates from the probabilistic map to the exploration node, which decomposes the full map m into $m_{reduced}$ according to Eq. (43), and builds a cost map based on Dijkstra's search to determine collision-free trajectory costs for all pose candidates. Finally, the exploration node applies Eqs. (42,44,45) to update the desired robot trajectory on a receding-horizon. An overview of the process is illustrated in Fig. 40.
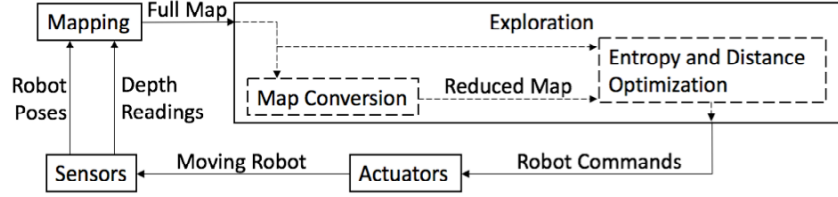
Figure 40. The diagram of the 3D probabilistic mapping and autonomous exploration nodes shows the primary processes and communication lines. These ROS nodes (boxes) operate together in real-time.

7.3.2   Results

A 3D environment of Mars is simulated in Gazebo. A height map [266] is used to generate a contoured surface, and the corresponding picture of Mars is draped over this contour, shown in Fig. 41. A 3D laser scanner is also simulated in Gazebo. In the horizontal direction, the sensor has limits $\Psi = 120°$ with a total of 1000 measurement rays inside, the sensor is fixed at angle $\tilde{\psi} = 45°$, and $n_\psi = 16$ sample measurements are used. In the vertical direction, the sensor also has limits $\Theta = 120°$ with a total of 1000 measurement rays inside, but the sensor is fixed at angle $\tilde{\theta} = 30°$, and $n_\psi = 7$ sample measurements are used. These ray samples are taken from each candidate location, which are separated 1 m apart in each of the 3 dimensions.

The map parameters are also important to the success of the exploration. The full map has dimensions 20 m × 20 m × 5 m in the Mars-fixed frame, with cell edge length $\alpha = 0.075$ m. The reduced map for collision-avoidance and motion planning has cells $k = 3$ times the size (0.225 m), so $k^3 = 27$ cells are considered in Eq. (43). The bump functions use $f_{max} = 1.0$, $f_{far} = 0.1$, and $\beta = 0.1$ to account for travel costs with Eq. (44). The receding horizon optimal time d_{opt} is based on a fixed robot velocity of 0.25 m/s and the computation time varies from 1.8 sec to 2.5 sec.

The simulation was run twice. Case 1 was as described in this section. Case 2 was identical to Case 1, except the reduced map $m_{reduced}$ is used when computing Eq. (41). Case 2 is largely inspired by the promising results of [262], where a projected map based on the same criteria as Eq. (43) proved effective for level flight. The resulting occupancy grid maps for Cases 1 and 2 are shown in Figs. 42 and 43, respectively. A video of Case 1 can be found at [267] and close-up pictures from Case 2 are shown in Fig. 44. The complete map entropy is illustrated in Fig. 45.

In both cases, the robot built the 3D probabilistic map of the 2000 cubic meter space composed of 4.74×10^6 grid cells. The maps were mostly complete within 10 minutes. The $\tilde{\theta} = 30°$ downward viewing angle captured the ground nicely, as candidate attitudes tended to direct the onboard sensor toward uncertain regions on the surface of Mars. The proposed approach provided collision-free mapping and autonomous exploration in real-time.

However, the choice of occupancy grid map used for entropy predictions introduced an

interesting tradeoff. In Case 1, when the full probabilistic map m was used in Eq. (41), regions where the grid cells were partially-known were frequently reconsidered until the space was well-known. Conversely in Case 2, when $m_{reduced}$ was used instead, the robot repeatedly left spaces that were missing a few grid cells to visit new terrain. This is because $m_{reduced}$ contained some cells with large occupancy probabilities based on Eq. (43), which allowed some grid cells of m enclosed within a cell of $m_{reduced}$ to be uncertain. The exploration policy of Case 2 incorrectly assumed these regions were well-known. Ironically, this false assumption actually led to greater information gains when the vehicle moved on to unvisited terrain. Conversely with Case 1, which used m for computing expected entropy, the total map entropy decreased more steadily and generated a more-complete 3D occupancy grid of the surface of Mars.

In short, the proposed 3D probabilistic occupancy grid mapping and autonomous exploration were simulated successfully in real-time over the surface of Mars using ROS and Gazebo. Choosing m for entropy predictions produced a more-complete map but choosing $m_{reduced}$ was sometimes beneficial for exploring new terrain faster, while forgoing map completeness.

a.) Height Map   b.) Color Map   c.) Gazebo Environment
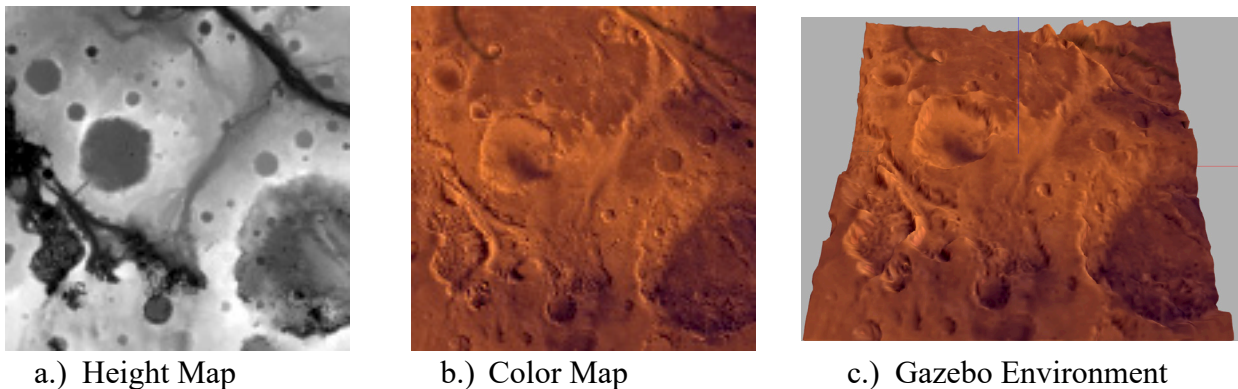
Figure 41. The height map (a) and color map (b) are combined in the Gazebo simulator (c) to model a Mars environment. The robot captures the simulated environment to generate an occupancy grid map.
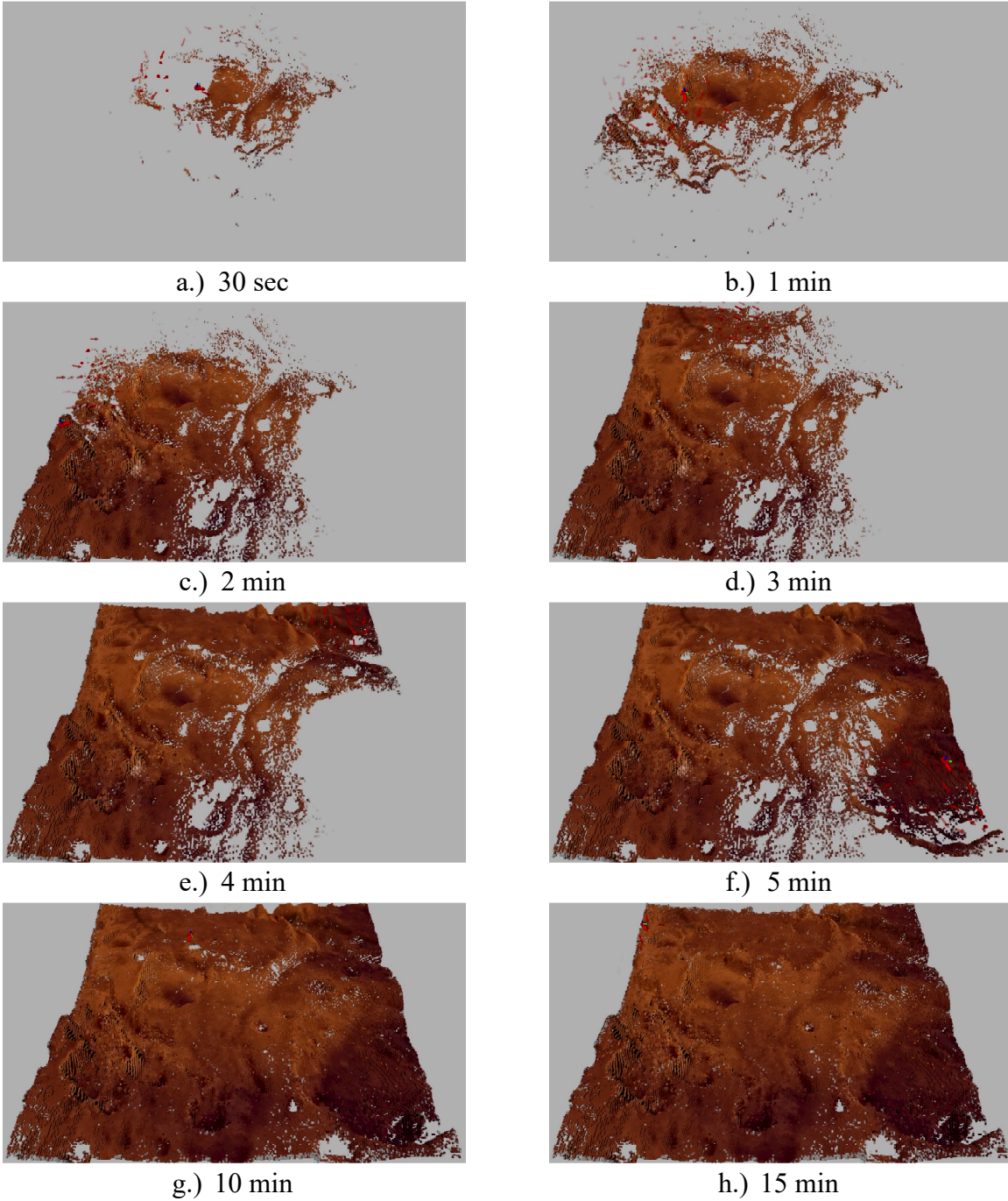
Figure 42. In Case 1, the robot (red disk with arrow indicating laser direction) moves toward candidate poses (red arrows, more opaque for greater reward) based on expected entropy change of the 3D probabilistic occupancy grid map m **(cubes: greater opacity for greater occupancy probability) of the surface of Mars.**
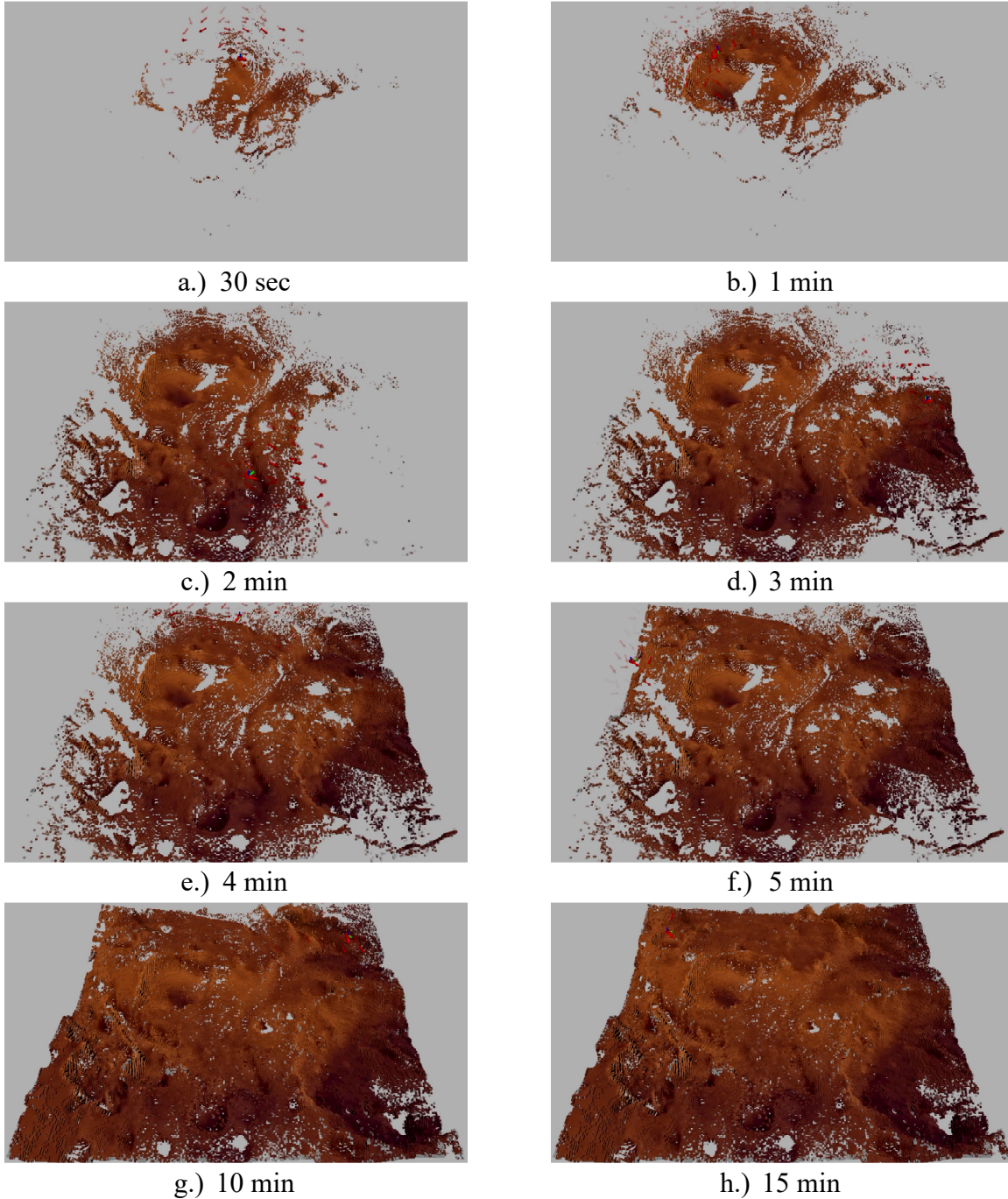
Figure 43. In Case 2, the robot (red disk with arrow indicating laser direction) generates a 3D probabilistic occupancy grid map m **(cubes: greater opacity for greater occupancy probability), which is used to generate a reduced map** m_{reduced} **based on Eq. (43). The robot moves toward candidate poses (red arrows, more opaque for greater reward) based on expected entropy change of** m_{reduced}**. Using** m_{reduced} **instead of** m **for entropy calculation leads to faster exploration of new terrain, but this leaves some grid cells missing.**
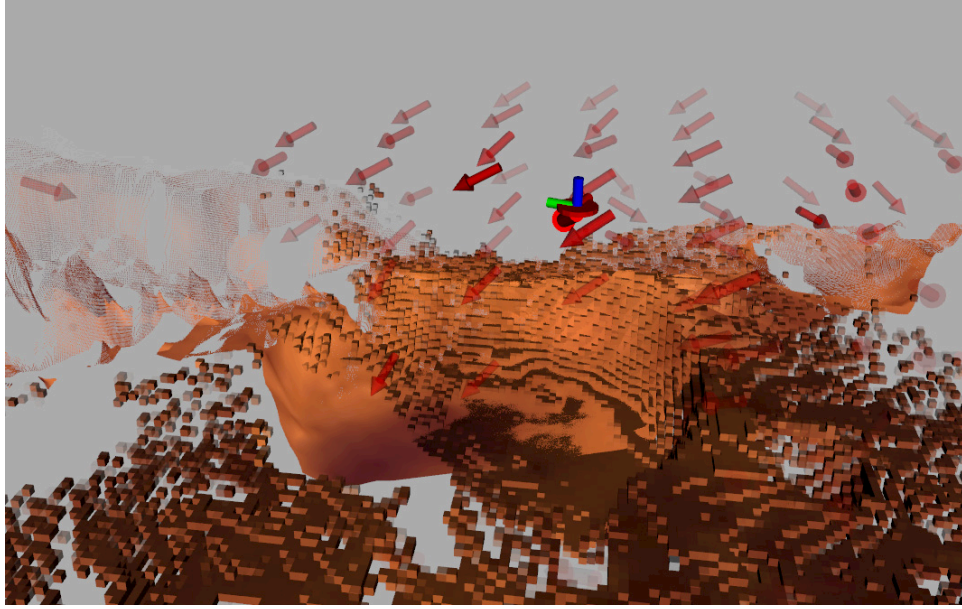
a.) Full map cells and sensor scan
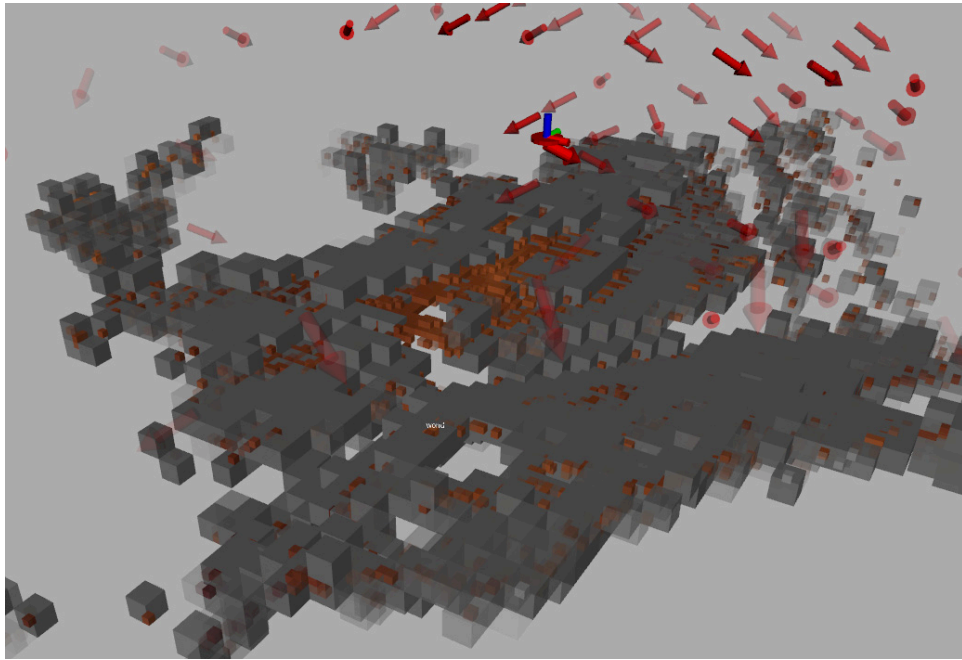
b.) Full map and reduced map cells

Figure 44. The close-up images from the Case 2 trial show the candidate future poses (red arrows), where greater opacity represents a larger objective function of Eq. (45). In (a), we show the 3D scan with color corresponding to the surface of Mars. In (b), we overlay the full map m (colored) with the reduced map m_{reduced} (gray) from Eq. (43).
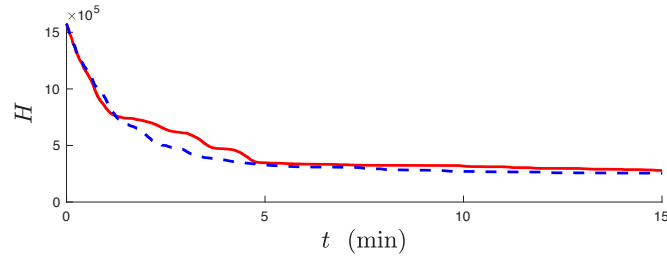
Figure 45. The complete map entropy for Case 1 (red solid line) decreases at roughly the same rate as the reduced map entropy for Case 2 (dashed blue line) toward the beginning. However, the expected entropy in Case 2 promotes actions toward unexplored territory, while the policy of Case 1 yields a more complete map before moving on to unexplored spaces.

7.4   Summary

We developed an approach to autonomously explore the complex and uncertain terrain of Mars. The exploration strategy is designed for flying vehicles near the surface of Mars, where the exploration policy is based on expected information gain from Shannon's entropy of a probabilistic map, and travel costs from Dijkstra's algorithm. The autonomous exploration scheme is applied in real-time, following a receding-horizon framework, so the map could be generated as quickly as possible. Numerical simulations demonstrated the efficacy of the approach, showing two possible versions of the 3D exploration with differing behavior in probabilistic map accuracy and exploration speed.

8   TECHNOLOGY ROADMAP AND ALTERNATIVE OPPORTUNITIES

8.1   Technology Roadmap

The Marsbee concept offers a number of favorable features for enhancing Martian exploration, especially through extending the capabilities of current rovers. Although the Marsbee concept looks feasible, there are a number of enabling technologies that must be advanced for full realization and fielding of this concept.

The immediate obstacle is the understanding of the interaction of thin, flexible structures with unsteady aerodynamics. Only after this fundamental question is positively answered can one consider developing other components such as controllers, sensors, and power sources to actuate and sustain the motion for exploration.

We envision that Marsbees should be designed with lightweight, multifunctional materials and structures, designated as one of the highest priorities in the 2016 NASA Space Technologies Roadmap [268]. Battery, circuit board, and gearbox can provide primary structural frame to further improve performance.

Advancements in sensors miniaturization and thin film electronics are crucial for successful Marsbee development. For example, antennas or radiators can be embedded in the large surface area wings. The majority of available GNC schemes rely on GPS. Efficient, vision-based methods are required for increased levels of vehicle autonomy as well as swarm collaboration in an environment without GPS [268].

Onboard power source is another challenge that must be addressed. Significant advances in battery technology to increase energy and power densities, and methods of thermal control in the extremely varying Martian atmosphere are expected in the next 10 years. For example, solid state batteries are being developed to operate in the extreme temperature environment on the lunar surface, which can be applied on Mars as well. Novel structured batteries like self-heating Lithium-ion batteries can improve performance at low Martian temperatures [269–272].

The development of the guidance and control methods of bioinspired vehicles with flexible wings will be important as well. Wind gusts up to 10 m/s are common on Mars [5]. Data-driven control methods show promising progress to address this challenging problem of the flight control in an unsteady environment [273,274] including the Coriolis effect on Mars. Bioinspired intermittent flight modes - hover, forward flight, and gliding – can potentially lead to a reduction in overall mission energy consumption by conducting energy intensive tasks, such as data transmission, during gliding flight.

The long-term vision is to integrate the Marsbees with sensors and wireless communication devices to provide a reconfigurable and resilient architecture of a swarm of Marsbees in combination with a rover.

9   OTHER BENEFITS OF THE STUDY

The spin-offs of the proposed Marsbee architecture can lead to successful bio-inspired design for MAVs on Earth: Bumblebees can both hover and fly at high speeds with heavy

payloads [10]. Millions of Monarch butterflies annually migrate, travelling up to 4000 km over the course of three months [275–280]. Dynamically scaling the physical mechanisms behind the long-range migration and agile maneuverability of insects has the potential to overcome the main challenges in the development of MAVs. Understanding the fluid-structure interaction of flexible flapping wings can elucidate the key mechanisms in biolocomotion of flying and swimming animals that can inspire development of aerial and underwater vehicles. Developed physics based model and control algorithms can be applied to autonomous aerial and underwater vehicles.

Value models have been recognized in many different NASA and NSF sponsored workshops [281–283] as an improvement over decision analysis approaches of the past, and could provide a basis for how systems engineering should be conducted in the future. Enhancing the performance of batteries at Martian temperatures can guide the future design of batteries for cold terrestrial environments, e.g. high-altitude drones and electric vehicles in Polar regions on Earth and other planets with cold climates.

10   PUBLICATIONS

Journal publication

- Bluman, J. E., Pohly, J., Sridhar, M. K., Kang, C., Landrum, D. B., Fahimi, F. & Aono, H. "Achieving bioinspired flapping wing hovering flight solutions on Mars via wing scaling," *Bioinspir. Biomim.*, Vol. 13, 046010, 2018 (doi: 10.1088/1748-3190/aac876)

Conference papers

- Bluman, J. E., Kang, C.-K., Landrum, D. B., Fahimi, F. & Mesmer, B. "Marsbee - Can a Bee Fly on Mars?," *AIAA-2017-0328*, 55th AIAA Aerospace Sciences Meeting, Grapevine, Texas, January 9-13, 2017 (http://arc.aiaa.org/doi/10.2514/6.2017-0328)
- Pohly, J. A., Kang, C.-K., Sridhar, M., Landrum, D. B., Fahimi, F., Bluman, J. E., Aono, H. & Liu, H. "Payload and Power for Dynamically Similar Flapping Wing Hovering Flight on Mars," *AIAA-2018-0020*, 1–11. 56th AIAA Aerospace Sciences Meeting, Kissimmee, Florida, January 8-12, 2018 (https://arc.aiaa.org/doi/10.2514/6.2018-0020)
- Pohly, J. A., Kang, C., Sridhar, M., Landrum, D. B., Fahimi, F., Mesmer, B., Bluman, J. E., Aono, H. & Lee, T. "Scaling Bioinspired Mars Flight Vehicles for Hover," *AIAA-2019-0567*, 1–13. 57th AIAA Aerospace Sciences Meeting, San Diego, California, January 7-11, American Institute of Aeronautics and Astronautics, 2019 (https://arc.aiaa.org/doi/10.2514/6.2019-0567)
- Kaufman, E. T. & Lee, T. "Autonomous Aerial Exploration for Topological Mapping of Mars Environments," AIAA 2019-1915, AIAA 2019 Scitech Forum, San Diego, California, January 7 - 11, 2019, 2019

Poster presentations

- Doneshwar, S., Mesmer, B., "Systems Approach for the NASA Marsbee Mission", Society of Reliability Engineers RAM Training Summit XI, Huntsville, AL, October 24th, 2018
- Doneshwar, S., Palma, G., Mesmer, B., "Using Value Modeling and Design Structure Matrices for the NASA Marsbee Project", 11th Wernher von Braun Memorial Symposium, Huntsville, AL, October, 2018

APPENDIX A. SYSTEM VALUE STATISTICS

A.1 Subsystem Quality Statistics

Table A.1. Subsystem quality questions descriptive statistics

	N	Mean	Median	Mode	Std. Deviation	Minimum	Maximum
Q16	17	2.0000	2	1	1.17260	1.00	5.00
Q17	17	2.1176	2	2	1.21873	1.00	5.00
Q18	17	2.0588	2	2	1.14404	1.00	5.00
Q19	17	2.0000	2	2	1.06066	1.00	5.00
Q20	17	2.6471	3	2*	1.05719	1.00	5.00
Q21	17	2.1765	2	2	1.01460	1.00	5.00
Q22	17	2.2353	2	2	1.09141	1.00	5.00
Q23	17	3.5882	4	3*	1.22774	1.00	5.00
Q24	17	1.9412	2	1	1.08804	1.00	5.00
Q25	17	2.7059	3	3	1.10480	1.00	5.00
Q26	17	3.2353	3	3	.90342	2.00	5.00
Q27	17	3.4706	3	3	1.06757	2.00	5.00
Q28	17	1.6471	2	1	.70189	1.00	3.00

*multiple modes exist. The smallest value is shown.

Table A.2. Subsystem quality questions null hypothesis test summary. Asymptotic significances are displayed. The significance level is 0.05

Question	Sig.	Decision
16	.045	Reject the null hypothesis
17	.028	Reject the null hypothesis
18	.045	Reject the null hypothesis
19	.148	Retain the null hypothesis
20	.146	Retain the null hypothesis
21	.121	Retain the null hypothesis
22	.045	Reject the null hypothesis
23	.422	Retain the null hypothesis
24	.148	Retain the null hypothesis
25	.121	Retain the null hypothesis
26	.065	Retain the null hypothesis
27	.470	Retain the null hypothesis
28	.161	Retain the null hypothesis

Q16. Performance metrics are important for the specific part of the Marsbee system I am working on (such as thrust of a rocket, range of an electric vehicle, bass quality of headphones, etc.)
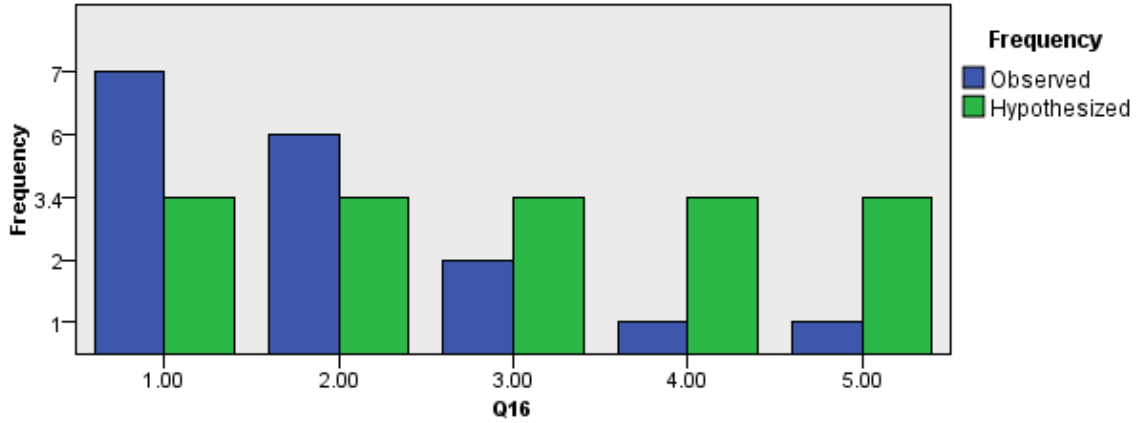
Figure A.1. Q16 One sample chi-square test.

Table A.3. Q16 One sample chi-square test results

Total N	17
Test Statistic	9.765
Degrees of Freedom	4
Asymptotic Sig. (2-sided test)	.045

Table A.4. Q16 statistics.

		Frequency	Percent	Valid Percent	Cumulative Percent
Valid	1.00	7	41.2	41.2	41.2
	2.00	6	35.3	35.3	76.5
	3.00	2	11.8	11.8	88.2
	4.00	1	5.9	5.9	94.1
	5.00	1	5.9	5.9	100.0
	Total	17	100.0	100.0	

Q17. Attributes are important for the specific part of the Marsbee system I am working on
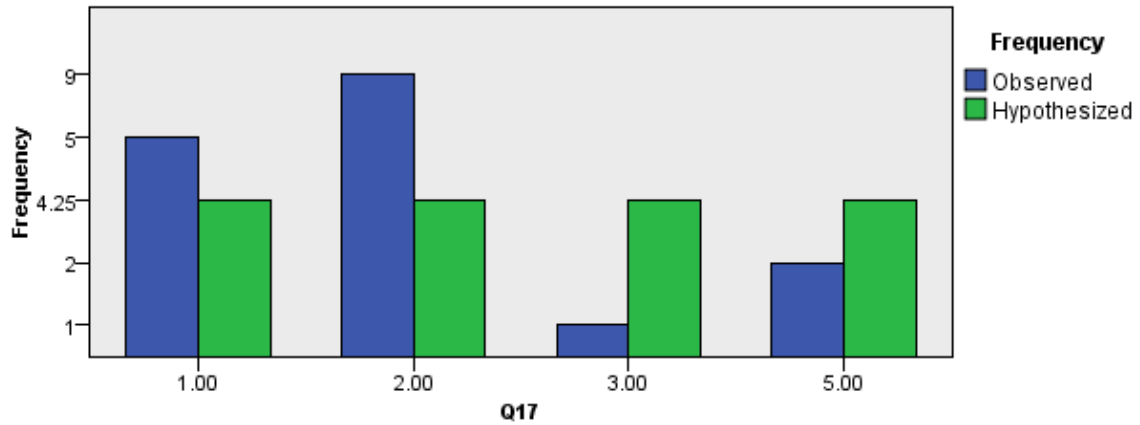
Figure A.3. Q17 One sample chi-square test.

Table A.5. Q17 One sample chi-square test results.

Total N	17
Test Statistic	9.118
Degrees of Freedom	3
Asymptotic Sig. (2-sided test)	.028

Table A.6. Q17 statistics.

		Frequency	Percent	Valid Percent	Cumulative Percent
Valid	1.00	5	29.4	29.4	29.4
	2.00	9	52.9	52.9	82.4
	3.00	1	5.9	5.9	88.2
	5.00	2	11.8	11.8	100.0
	Total	17	100.0	100.0	

Q18. Robustness   - The thing of interest should not produce radical departures from its expected behavior is response to small changes to its operating input, internal state, or external environment. Robustness is important for the specific part of the Marsbee system I am working on.
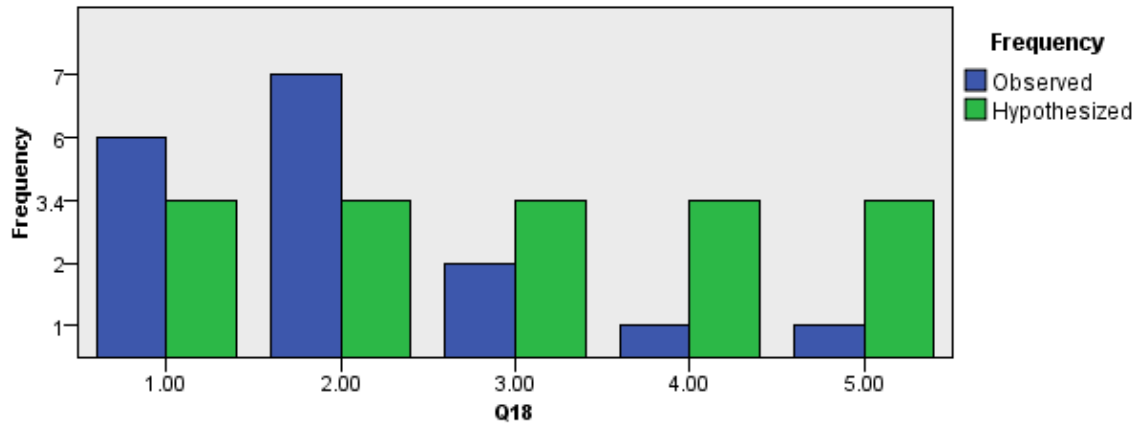
Figure A.4. Q18 One sample chi-square test.

Table A.7. Q18 One sample chi-square test results.

Total N	17
Test Statistic	9.765
Degrees of Freedom	4
Asymptotic Sig. (2-sided test)	.045

Table A.8. Q18 statistics.

		Frequency	Percent	Valid Percent	Cumulative Percent
Valid	1.00	6	35.3	35.3	35.3
	2.00	7	41.2	41.2	76.5
	3.00	2	11.8	11.8	88.2
	4.00	1	5.9	5.9	94.1
	5.00	1	5.9	5.9	100.0
	Total	17	100.0	100.0	

Q22. Efficiency - The thing of interest produces the desired results with lesser expenditure of resources compared to competing alternatives. Efficiency is important to the specific part of the Marsbee system I am working on
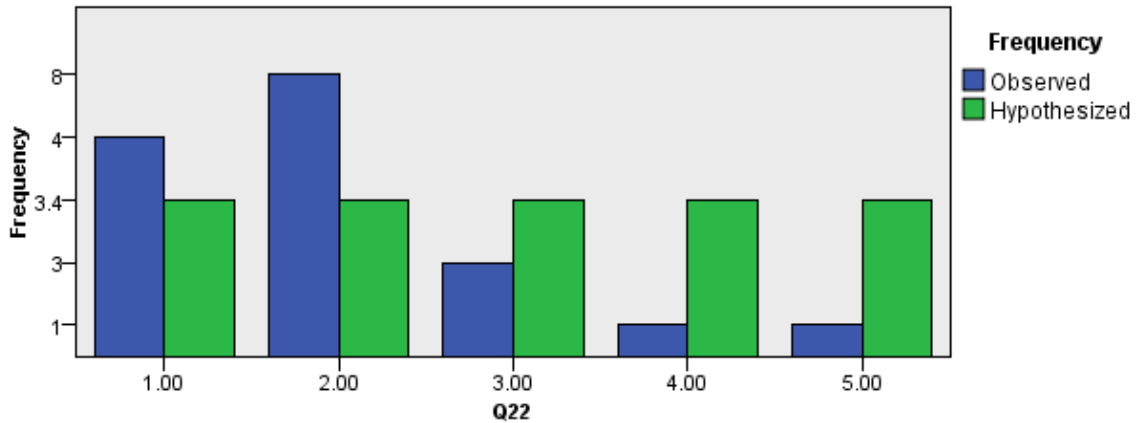
Figure A.5. Q22 One sample chi-square test.

Table A.9. Q22 One sample chi-square test results.

Total N	17
Test Statistic	9.765
Degrees of Freedom	4
Asymptotic Sig. (2-sided test)	.045

Table A.10. Q22 statistics.

		Frequency	Percent	Valid Percent	Cumulative Percent
Valid	1.00	4	23.5	23.5	23.5
	2.00	8	47.1	47.1	70.6
	3.00	3	17.6	17.6	88.2
	4.00	1	5.9	5.9	94.1
	5.00	1	5.9	5.9	100.0
	Total	17	100.0	100.0	

A.2   System Quality Statistics

Table A.11. System quality questions descriptive statistics.

	N	Mean	Median	Mode	Std. Deviation	Minimum	Maximum
Q29	17	1.5294	2	2	.51450	1.00	2.00
Q30	17	1.5882	2	1*	.61835	1.00	3.00
Q31	17	2.0000	2	2	.79057	1.00	4.00
Q32	17	1.7059	2	2	.58787	1.00	3.00
Q33	17	2.4118	2	2*	.79521	1.00	4.00
Q34	17	2.0588	2	2	.65865	1.00	3.00
Q35	17	1.6471	2	2	.60634	1.00	3.00
Q36	17	3.3529	3	3	1.36662	1.00	5.00
Q37	17	1.8824	2	2	.60025	1.00	3.00
Q38	17	2.3529	2	2	.78591	1.00	4.00
Q39	17	3.1176	3	3	1.16632	1.00	5.00
Q40	16	1.6875	1.5	1	.79320	1.00	3.00
Q41_1	15	2.2000	2	1	1.61245	1.00	6.00
Q41_2	15	2.8000	3	2	1.20712	1.00	5.00
Q41_3	15	5.3333	6	7	1.54303	3.00	7.00
Q41_4	15	5.2000	5	5*	1.42428	3.00	7.00
Q41_5	15	3.0667	2	2	1.98086	1.00	7.00
Q41_6	15	6.9333	8	8	2.18654	1.00	8.00
Q41_7	15	5.2667	5	5	2.21897	1.00	8.00

*Multiple modes exist. The smallest value is shown

Table A.12. Subsystem quality questions null hypothesis test summary. Asymptotic significances are displayed. The significance level is 0.05.

Question	Sig.	Decision
30	.056	Retain the null hypothesis
31	.009	Reject the null hypothesis
32	.028	Reject the null hypothesis
33	.065	Retain the null hypothesis
34	.080	Retain the null hypothesis
35	.047	Reject the null hypothesis
36	.346	Retain the null hypothesis
37	.019	Reject the null hypothesis
38	.052	Retain the null hypothesis
39	.227	Retain the null hypothesis
40	.305	Retain the null hypothesis
41.1	.027	Reject the null hypothesis
41.2	.504	Retain the null hypothesis
41.3	.504	Retain the null hypothesis
41.4	.856	Reject the null hypothesis
41.5	.467	Retain the null hypothesis
41.6	.000	Reject the null hypothesis
41.7	.467	Retain the null hypothesis

Q31. Robustness - The thing of interest should not produce radical departures from its expected behavior is response to small changes to its operating input, internal state, or external environment. How important is the Marsbee system's robustness to me?
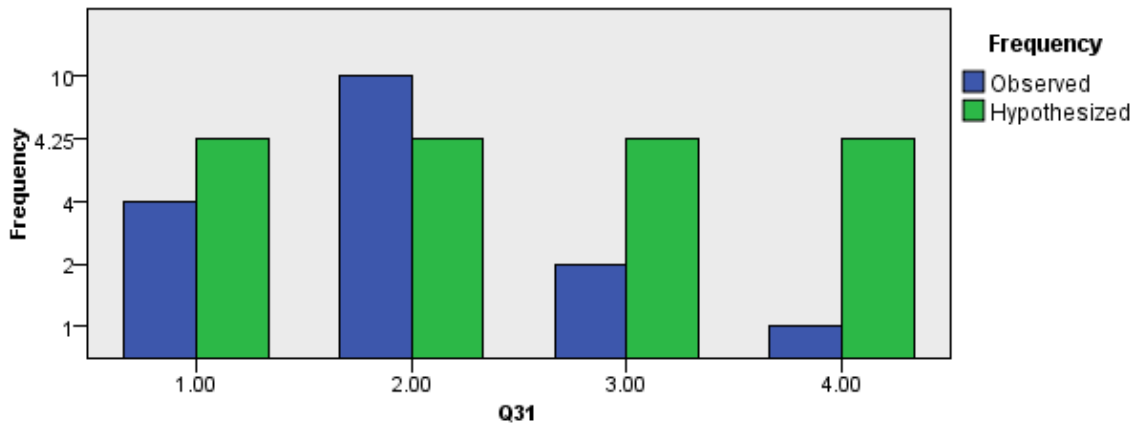
Figure A.6. Q31 One sample chi-square test.

Table A.13. Q31 One sample chi-square test results.

Total N	17
Test Statistic	11.471
Degrees of Freedom	3
Asymptotic Sig. (2-sided test)	.009

Table A.14. Q31 statistics.

		Frequency	Percent	Valid Percent	Cumulative Percent
Valid	1.00	4	23.5	23.5	23.5
	2.00	10	58.8	58.8	82.4
	3.00	2	11.8	11.8	94.1
	4.00	1	5.9	5.9	100.0
	Total	17	100.0	100.0	

Q32. Reliability - The ability of a thing of interest to perform as intended (i.e. without failure and within specified performance limits) for a specified time, in its life cycle conditions. It is a measure of how often the thing of interest fails. How important is the Marsbee system's reliability to me?
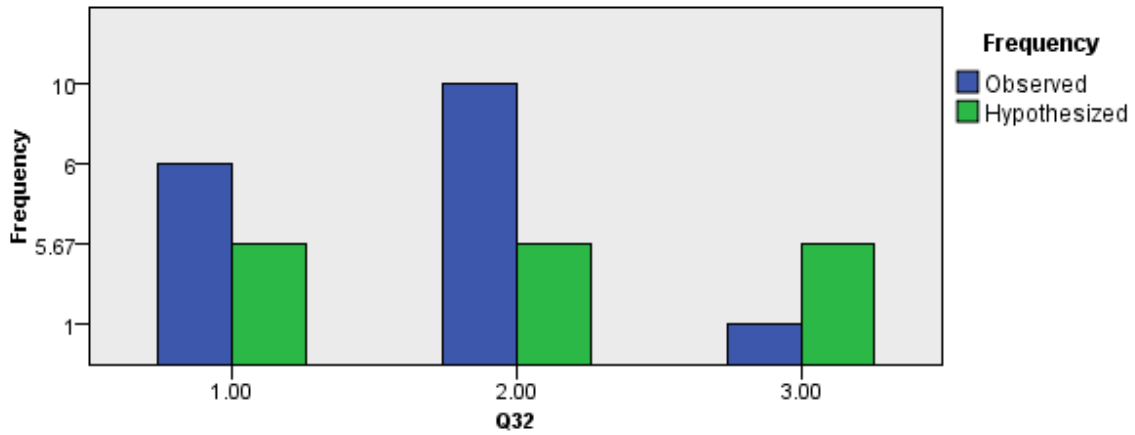
Figure A.7. Q32 One sample chi-square test.

Table A.15. Q32 One sample chi-square test results.

Total N	17
Test Statistic	7.176
Degrees of Freedom	2
Asymptotic Sig. (2-sided test)	.028

Table A.16. Q32 statistics.

		Frequency	Percent	Valid Percent	Cumulative Percent
Valid	1.00	6	35.3	35.3	35.3
	2.00	10	58.8	58.8	94.1
	3.00	1	5.9	5.9	100.0
	Total	17	100.0	100.0	

Q35. Efficiency - The thing of interest produces the desired results with lesser expenditure of resources compared to competing alternatives. How important is the Marsbee system's efficiency to me?
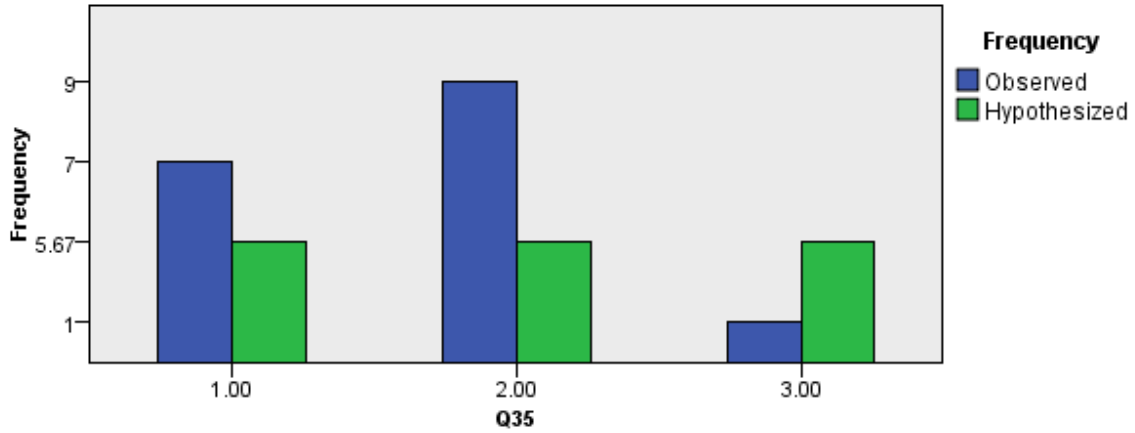
Figure A.8. Q35 One sample chi-square test.

Table A.17. Q35 One sample chi-square test results.

Total N	17
Test Statistic	6.118
Degrees of Freedom	2
Asymptotic Sig. (2-sided test)	.047

Table A.18. Q35 statistics.

		Frequency	Percent	Valid Percent	Cumulative Percent
Valid	1.00	7	41.2	41.2	41.2
	2.00	9	52.9	52.9	94.1
	3.00	1	5.9	5.9	100.0
	Total	17	100.0	100.0	

Q37. Efficacy - The thing of interest produces the anticipated behavior (or the expected output) over the expected range of input conditions, control variations, etc. How important is the Marsbee system's efficacy to me?
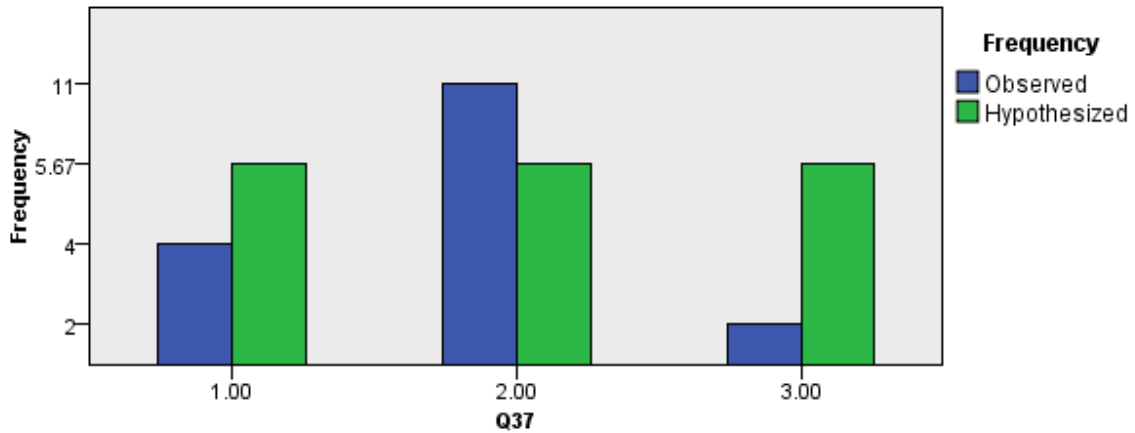
Figure A.9. Q37 One sample chi-square test.

Table A.19. Q37 One sample chi-square test results.

Total N	17
Test Statistic	7.882
Degrees of Freedom	2
Asymptotic Sig. (2-sided test)	.019

Table A.20. Q37 statistics.

		Frequency	Percent	Valid Percent	Cumulative Percent
Valid	1.00	4	23.5	23.5	23.5
	2.00	11	64.7	64.7	88.2
	3.00	2	11.8	11.8	100.0
	Total	17	100.0	100.0	

Q41. Rank order the following system characteristics, with the top characteristic being most important to you and the bottom characteristic being the least important. – 1-8

Q41.1 Robustness
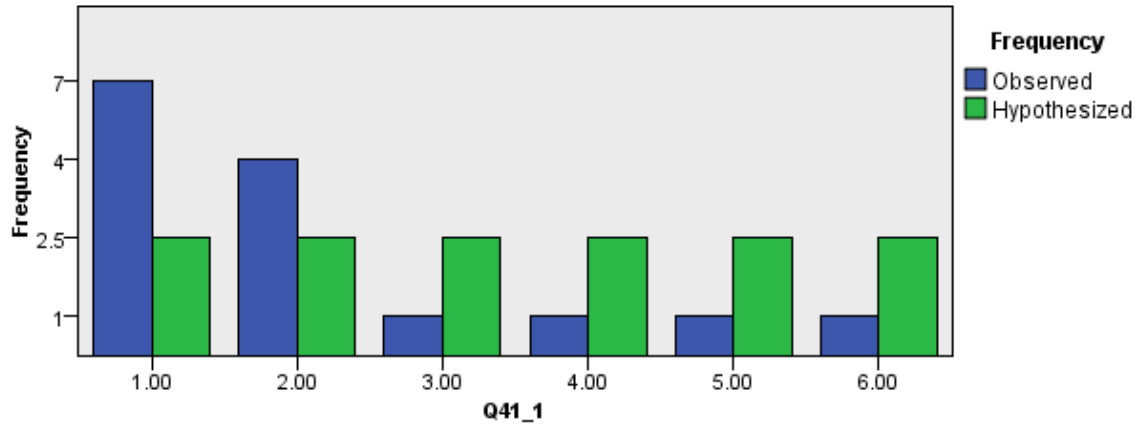
Figure A.10. Q41.1 One sample chi-square test.

Table A.21. Q41.1 One sample chi-square test results.

Total N	15
Test Statistic	12.6
Degrees of Freedom	5
Asymptotic Sig. (2-sided test)	.027

Table A.22. Q41.1 statistics.

Q41_1

		Frequency	Percent	Valid Percent	Cumulative Percent
Valid	1.00	7	41.2	46.7	46.7
	2.00	4	23.5	26.7	73.3
	3.00	1	5.9	6.7	80.0
	4.00	1	5.9	6.7	86.7
	5.00	1	5.9	6.7	93.3
	6.00	1	5.9	6.7	100.0
	Total	15	88.2	100.0	
Missing	System	2	11.8		
Total		17	100.0		

Q41.6. Profitability
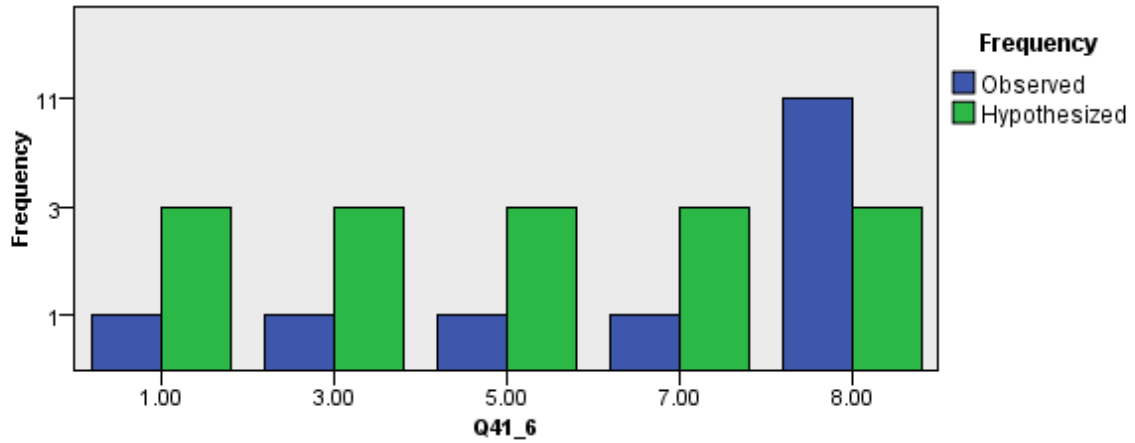
Figure A.11. Q41.6 One sample chi-square test.

Table A.23. Q41.6 One sample chi-square test results.

Total N	15
Test Statistic	26.667
Degrees of Freedom	4
Asymptotic Sig. (2-sided test)	.000

Table A.24. Q41.6 statistics.

		Frequency	Percent	Valid Percent	Cumulative Percent
Valid	1.00	1	5.9	6.7	6.7
	3.00	1	5.9	6.7	13.3
	5.00	1	5.9	6.7	20.0
	7.00	1	5.9	6.7	26.7
	8.00	11	64.7	73.3	100.0
	Total	15	88.2	100.0	
Missing	System	2	11.8		
Total		17	100.0		

A.3   Project Quality Statistics

Table A.25. Project specific questions descriptive statistics.

	N	Mean	Median	Mode	Std. Deviation	Minimum	Maximum
Q56	17	2.6471	3	3	1.72993	-2.00	5.00
Q57	17	2.4118	2	1*	1.22774	1.00	5.00
Q58	17	2.8824	3	3	1.49509	-2.00	5.00
Q59	17	2.5294	3	3	1.17886	1.00	5.00
Q60	17	2.7647	3	3	.66421	2.00	4.00
Q61	17	2.0000	2	1*	.93541	1.00	4.00
Q62	17	2.0588	2	2	.96635	1.00	4.00
Q63	17	2.5294	2	2	.94324	1.00	4.00
Q64	17	2.8235	3	3	.88284	1.00	4.00
Q65	17	2.8235	3	3	.95101	1.00	5.00
Q66	17	2.7059	3	3	.84887	1.00	4.00
Q67	17	2.5882	2	2	.87026	1.00	4.00
Q68	17	2.4118	2	2	1.37199	1.00	5.00
Q69	17	2.1765	2	2	.95101	1.00	4.00
Q70	17	1.8824	2	2	.69663	1.00	3.00
Q71	17	3.2941	3	2*	1.35852	1.00	5.00
Q72	17	2.4118	2	2	1.37199	1.00	5.00
Q73	17	4.2353	5	5	.97014	2.00	5.00
Q74	17	3.8235	4	5	1.28624	2.00	5.00
Q75	17	3.1765	3	2*	1.18508	2.00	5.00
Q76	17	3.1176	3	3	.92752	2.00	5.00
Q77	17	2.8824	3	3	1.05370	1.00	5.00
Q78	17	3.0000	3	3	1.00000	1.00	5.00
Q79	17	3.4706	3	3	.94324	2.00	5.00
Q80	17	2.2941	2	2	.84887	1.00	4.00
Q81	17	3.2353	3	3	.75245	2.00	5.00
Q82	17	3.0588	3	3	1.56007	-2.00	5.00
Q83	17	3.4706	3	3	.94324	2.00	5.00
Q84	17	3.6471	4	3	.86177	2.00	5.00
Q85	17	3.5882	4	3	1.12132	1.00	5.00
Q86	17	3.4118	3	3	1.06412	1.00	5.00
Q87	17	2.8235	3	3	1.62924	-2.00	5.00

*Multiple modes exist. The smallest value is shown

Table A.26. Project specific questions null hypothesis test summary. Asymptotic significances are displayed. The significance level is 0.05.

Question	Sig.	Decision
57	.422	Retain the null hypothesis
59	.346	Retain the null hypothesis
60	.113	Retain the null hypothesis
61	.268	Retain the null hypothesis
62	.121	Retain the null hypothesis
63	.325	Retain the null hypothesis
64	.220	Retain the null hypothesis
65	.027	Reject the null hypothesis
66	.148	Retain the null hypothesis
67	.098	Retain the null hypothesis
68	.346	Retain the null hypothesis
69	.181	Retain the null hypothesis
70	.193	Retain the null hypothesis
71	.422	Retain the null hypothesis
72	.346	Retain the null hypothesis
73	.043	Reject the null hypothesis
74	.181	Retain the null hypothesis
75	.268	Retain the null hypothesis
76	.325	Retain the null hypothesis
77	.072	Retain the null hypothesis
78	.116	Retain the null hypothesis
79	.181	Retain the null hypothesis
80	.148	Retain the null hypothesis
81	.009	Reject the null hypothesis
83	.181	Retain the null hypothesis
84	.148	Retain the null hypothesis
85	.182	Retain the null hypothesis
86	.045	Reject the null hypothesis

Q65. To me constant communication between the rover and all of the Marsbees is important
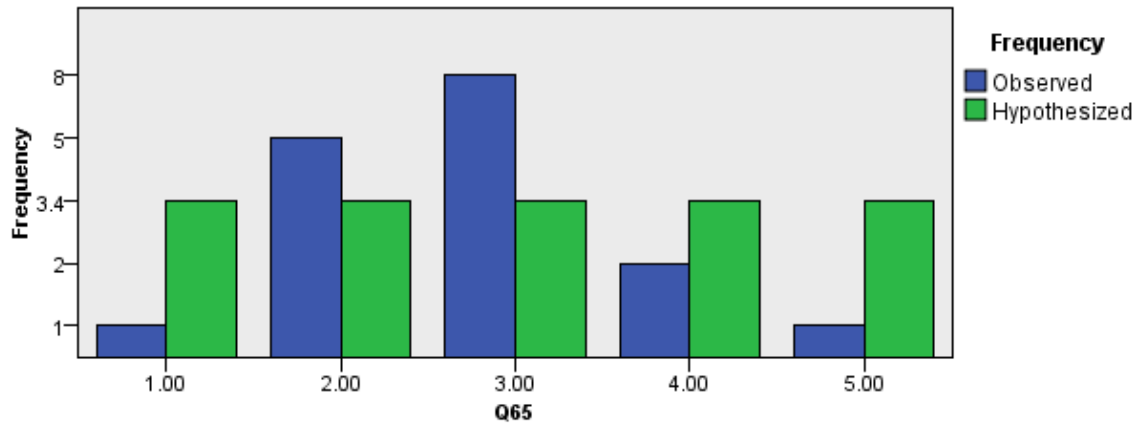
Figure A.12. Q65 One sample chi-square test

Table A.27. Q65 One sample chi-square test results

Total N	17
Test Statistic	10.941
Degrees of Freedom	4
Asymptotic Sig. (2-sided test)	.027

Table A.28. Q65 statistics

		Frequency	Percent	Valid Percent	Cumulative Percent
Valid	1.00	1	5.9	5.9	5.9
	2.00	5	29.4	29.4	35.3
	3.00	8	47.1	47.1	82.4
	4.00	2	11.8	11.8	94.1
	5.00	1	5.9	5.9	100.0
	Total	17	100.0	100.0	

Q73. To me the Marsbee having 2 wings is important
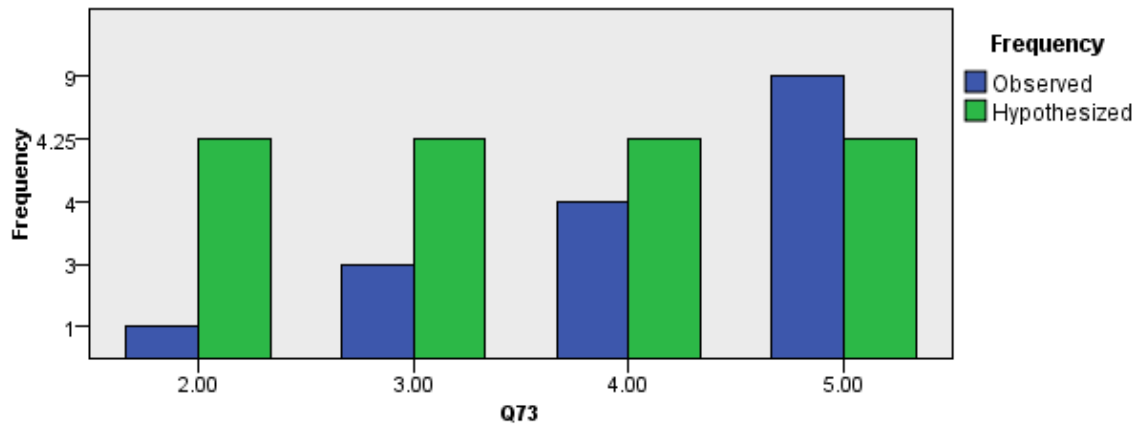
Figure A.13. Q73 One sample chi-square test

Table A.29. Q73 One sample chi-square test results

Total N	17
Test Statistic	8.176
Degrees of Freedom	3
Asymptotic Sig. (2-sided test)	.043

Table A.30. Q73 statistics

		Frequency	Percent	Valid Percent	Cumulative Percent
Valid	2.00	1	5.9	5.9	5.9
	3.00	3	17.6	17.6	23.5
	4.00	4	23.5	23.5	47.1
	5.00	9	52.9	52.9	100.0
	Total	17	100.0	100.0	

Q81. To me it is important that the Marsbee be equipped with chemical composition sensors
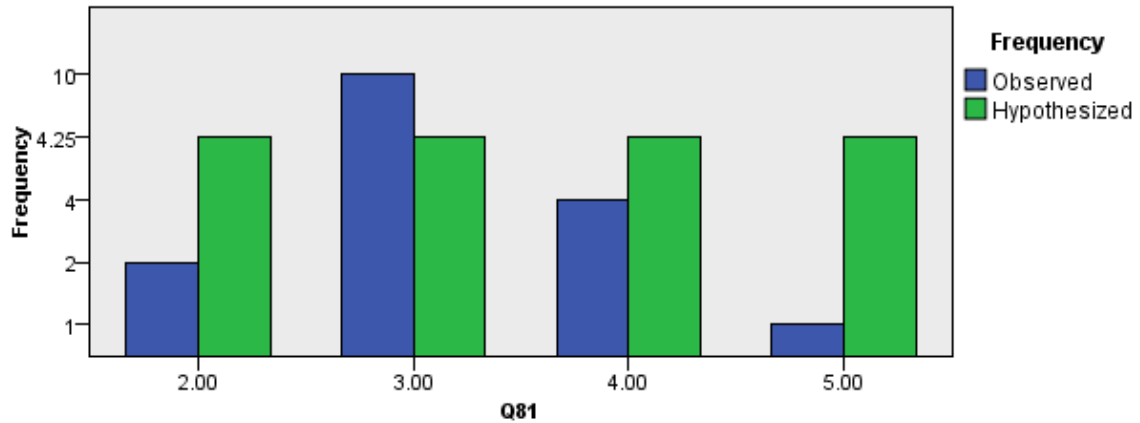
Figure A.14. Q81 One sample chi-square test

Table A.31. Q81 One sample chi-square test results

Total N	17
Test Statistic	11.471
Degrees of Freedom	3
Asymptotic Sig. (2-sided test)	.009

Table A.32. Q81 statistics

		Frequency	Percent	Valid Percent	Cumulative Percent
Valid	2.00	2	11.8	11.8	11.8
	3.00	10	58.8	58.8	70.6
	4.00	4	23.5	23.5	94.1
	5.00	1	5.9	5.9	100.0
	Total	17	100.0	100.0	

Q86. To me it is important that the Marsbee be equipped with a magnetometer
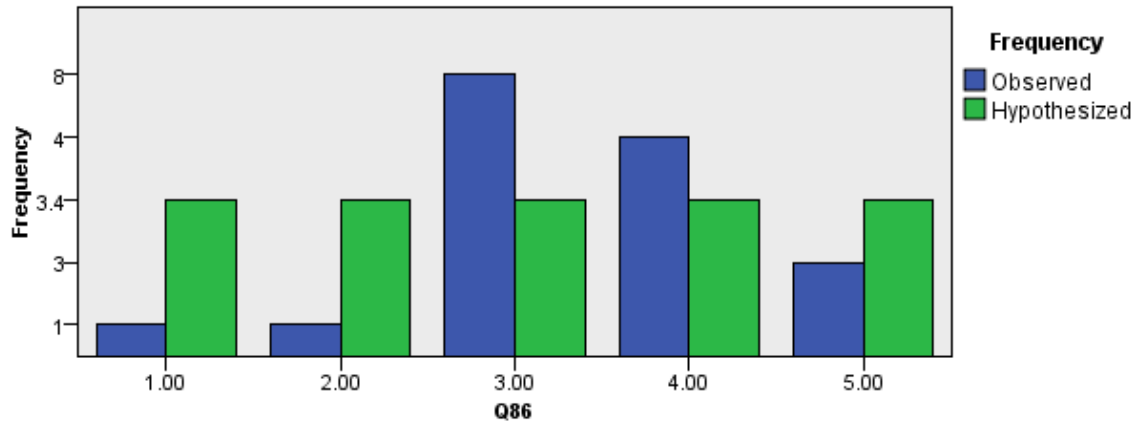
Figure A.15. Q86 One sample chi-square test.

Table A.33. Q86 One sample chi-square test results.

Total N	17
Test Statistic	9.765
Degrees of Freedom	4
Asymptotic Sig. (2-sided test)	.045

Table A.34. Q86 statistics.

		Frequency	Percent	Valid Percent	Cumulative Percent
Valid	1.00	1	5.9	5.9	5.9
	2.00	1	5.9	5.9	11.8
	3.00	8	47.1	47.1	58.8
	4.00	4	23.5	23.5	82.4
	5.00	3	17.6	17.6	100.0
	Total	17	100.0	100.0	

A.4   Mission Quality Statistics

Table A.35. Mission types questions descriptive statistics.

	N	Mean	Median	Mode	Std. Deviation	Minimum	Maximum
Q88	17	2.1176	2	2	.78121	1.00	4.00
Q89	17	2.1765	2	2	.88284	1.00	4.00
Q90	17	2.4706	3	3	.62426	1.00	3.00
Q91	17	3.0588	3	3	.65865	2.00	5.00
Q92	17	2.0588	2	2	.82694	1.00	4.00
Q93	17	3.1176	3	3	.99262	2.00	5.00
Q94	17	3.0000	3	4	1.76777	-2.00	5.00
Q95	17	1.8824	2	1*	1.05370	1.00	5.00
Q96	17	1.6471	1	1	.78591	1.00	3.00
Q97	17	1.8235	2	2	.72761	1.00	3.00
Q98	17	2.2353	2	2*	.90342	1.00	4.00

Table A.36. Mission types questions null hypothesis test summary. Asymptotic significances are displayed. The significance level is 0.05.

Question	Sig.	Decision
88	.012	Reject the null hypothesis
89	.220	Retain the null hypothesis
90	.047	Reject the null hypothesis
91	.000	Reject the null hypothesis
92	.043	Reject the null hypothesis
93	.325	Reject the null hypothesis
95	.065	Retain the null hypothesis
96	.193	Retain the null hypothesis
97	.327	Retain the null hypothesis
98	.268	Retain the null hypothesis

Q88. The primary mission of the Marsbee is to map the local terrain (within 50 yards from the rover)
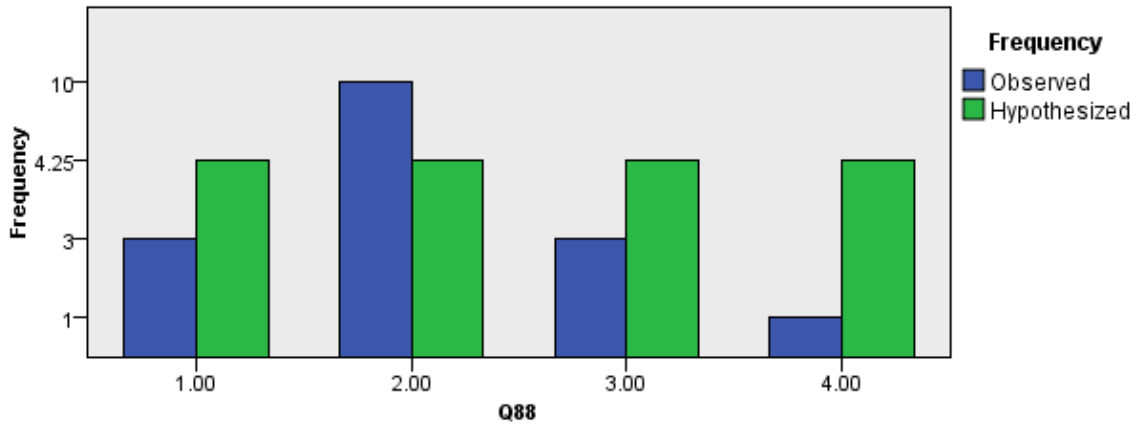
Figure A.16. Q88 One sample chi-square test

Table A.37. Q88 One sample chi-square test results

Total N	17
Test Statistic	11.0
Degrees of Freedom	3
Asymptotic Sig. (2-sided test)	.012

Table A.38. Q88 statistics

		Frequency	Percent	Valid Percent	Cumulative Percent
Valid	1.00	3	17.6	17.6	17.6
	2.00	10	58.8	58.8	76.5
	3.00	3	17.6	17.6	94.1
	4.00	1	5.9	5.9	100.0
	Total	17	100.0	100.0	

Q90. The primary mission of the Marsbee is to learn more about the Martian atmospheric structure (winds, pressure, etc.)
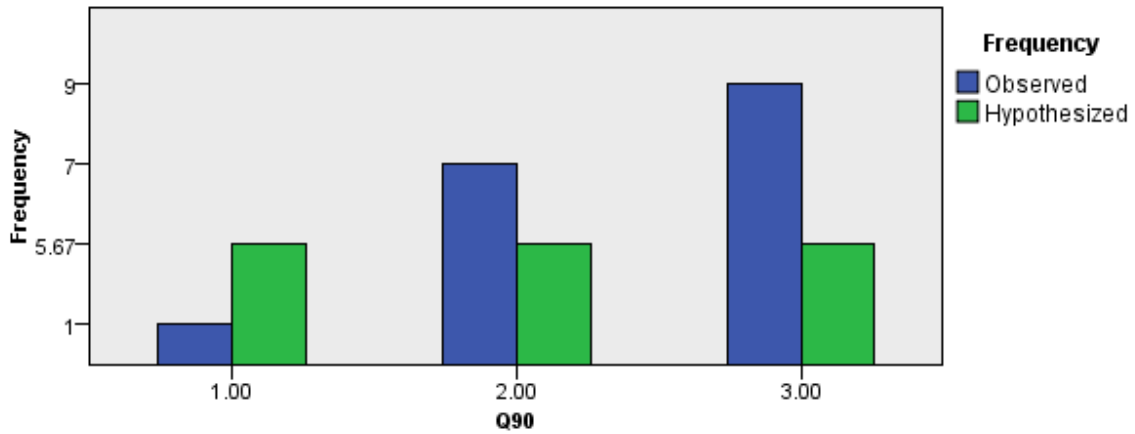
Figure A.17. Q90 One sample chi-square test

Table A.39. Q90 One sample chi-square test results

Total N	17
Test Statistic	6.118
Degrees of Freedom	2
Asymptotic Sig. (2-sided test)	.047

Table A.40. Q90 statistics

		Frequency	Percent	Valid Percent	Cumulative Percent
Valid	1.00	1	5.9	5.9	5.9
	2.00	7	41.2	41.2	47.1
	3.00	9	52.9	52.9	100.0
	Total	17	100.0	100.0	

Q91. The primary mission of the Marsbee is to learn more about the Martian atmospheric composition (chemistry)
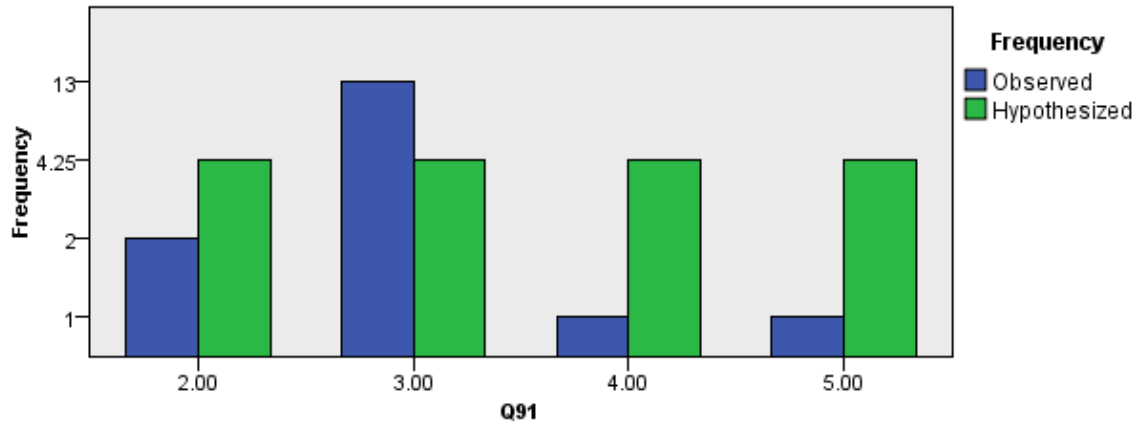
Figure A.18. Q91 One sample chi-square test

Table A.41. Q91 One sample chi-square test results

Total N	17
Test Statistic	24.176
Degrees of Freedom	3
Asymptotic Sig. (2-sided test)	.000

Table A.42. Q91 statistics

		Frequency	Percent	Valid Percent	Cumulative Percent
Valid	2.00	2	11.8	11.8	11.8
	3.00	13	76.5	76.5	88.2
	4.00	1	5.9	5.9	94.1
	5.00	1	5.9	5.9	100.0
	Total	17	100.0	100.0	

Q92. The primary mission of the Marsbee is to learn more about the Martian geology (land surface structure)
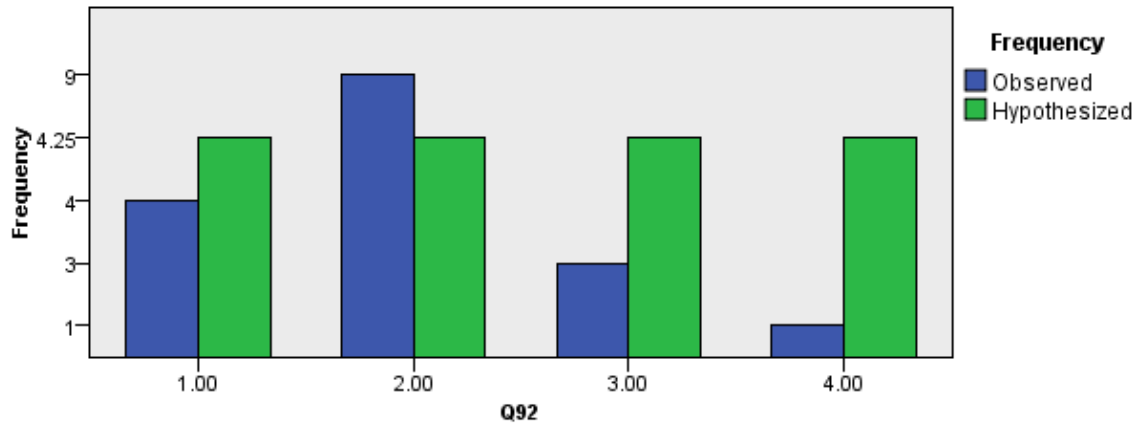
Figure A.19. Q92 One sample chi-square test

Table A.43. Q92 One sample chi-square test results

Total N	17
Test Statistic	8.176
Degrees of Freedom	3
Asymptotic Sig. (2-sided test)	.043

Table A.44. Q92 statistics

		Frequency	Percent	Valid Percent	Cumulative Percent
Valid	1.00	4	23.5	23.5	23.5
	2.00	9	52.9	52.9	76.5
	3.00	3	17.6	17.6	94.1
	4.00	1	5.9	5.9	100.0
	Total	17	100.0	100.0	

APPENDIX B. MARSBEE - QUESTIONNAIRE

Please answer all questions honestly.

Transactive Memory System Scale Items

Note. Items below use a 5-point disagree–agree response format, in which 1 strongly disagree, 2 disagree, 3 neutral, 4 agree, and 5 strongly agree.

Specialization

1. Each team member has specialized knowledge of some aspect of our project.

    Strongly   1   2   3   4   5   Strongly
    Disagree   Agree

2. I have knowledge about an aspect of the project that no other team member has.

    Strongly   1   2   3   4   5   Strongly
    Disagree   Agree

3. Different team members are responsible for expertise in different areas.

    Strongly   1   2   3   4   5   Strongly
    Disagree   Agree

4. The specialized knowledge of several different team members was needed to complete the project deliverables.

    Strongly   1   2   3   4   5   Strongly
    Disagree   Agree

5. I know which team members have expertise in specific areas.

    Strongly   1   2   3   4   5   Strongly
    Disagree   Agree

Credibility

6. I am comfortable accepting procedural suggestions from other team members.

    Strongly   1   2   3   4   5   Strongly
    Disagree   Agree

7. I trust that other members' knowledge about the project is credible.

    Strongly   1   2   3   4   5   Strongly
    Disagree   Agree

8. I am confident relying on the information that other team members brought to the discussion.

    Strongly   1   2   3   4   5   Strongly
    Disagree   Agree

9. When other members give information, I want to double-check it for myself.

    Strongly   1   2   3   4   5   Strongly

| | | Disagree | | | | | Agree | |

10. I do not have much faith in other members' "expertise."

| | Strongly | 1 | 2 | 3 | 4 | 5 | Strongly |
| | Disagree | | | | | | Agree |

Coordination

11. Our team works together in a well-coordinated fashion.

| | Strongly | 1 | 2 | 3 | 4 | 5 | Strongly |
| | Disagree | | | | | | Agree |

12. Our team has very few misunderstandings about what to do.

| | Strongly | 1 | 2 | 3 | 4 | 5 | Strongly |
| | Disagree | | | | | | Agree |

13. Our team needs to backtrack and start over a lot.

| | Strongly | 1 | 2 | 3 | 4 | 5 | Strongly |
| | Disagree | | | | | | Agree |

14. We accomplish the task smoothly and efficiently.

| | Strongly | 1 | 2 | 3 | 4 | 5 | Strongly |
| | Disagree | | | | | | Agree |

15. There is much confusion about how we would accomplish the task.

| | Strongly | 1 | 2 | 3 | 4 | 5 | Strongly |
| | Disagree | | | | | | Agree |

Adapted form of PERVAL questionnaire

Note. Items below use a 5-point important-not important response format, in which 1 not at all important, 2 slightly important, 3 moderately important, 4 very important, and 5 extremely important.

Subsystem Quality

16. Performance metrics are important for the specific part of the Marsbee system I am working on (such as thrust of a rocket, range of an electric vehicle, bass quality of headphones, etc.)

| | Not at all | 1 | 2 | 3 | 4 | 5 | Extremely |
| | Important | | | | | | Important |

17. Attributes are important for the specific part of the Marsbee system I am working on

| | Not at all | 1 | 2 | 3 | 4 | 5 | Extremely |
| | Important | | | | | | Important |

18. *Robustness - The thing of interest should not produce radical departures from its expected behavior is response to small changes to its operating input, internal state, or external environment.*

116

Robustness is important for the specific part of the Marsbee system I am working on

  Not at all   1 2 3 4 5 Extremely
  Important   Important

19. *Reliability - The ability of a thing of interest to perform as intended (i.e. without failure and within specified performance limits) for a specified time, in its life cycle conditions. It is a measure of how often the thing of interest fails.*

  Reliability is important to the specific part of the Marsbee system I am working on

  Not at all   1 2 3 4 5 Extremely
  Important   Important

20. *Maintainability - The ease with which a thing of interest can be modified to correct faults, improve performance or other attributes, or adapt to a changed environment*

  Maintainability is important to the specific part of the Marsbee system I am working on

  Not at all   1 2 3 4 5 Extremely
  Important   Important

21. *Availability – The probability that a thing of interest will work as required when required during the period of a mission.*

  Availability is important to the specific part of the Marsbee system I am working on

  Not at all   1 2 3 4 5 Extremely
  Important   Important

22. *Efficiency - The thing of interest produces the desired results with lesser expenditure of resources compared to competing alternatives.*

  Efficiency is important to the specific part of the Marsbee system I am working on

  Not at all   1 2 3 4 5 Extremely
  Important   Important

23. *Profitability – The degree to which a business or activity yields profit or financial gain related to the thing of interest.*

  Profitability is important to the specific part of the Marsbee system I am working on

  Not at all   1 2 3 4 5 Extremely
  Important   Important

24. *Efficacy - The thing of interest produces the anticipated behavior (or the expected output) over the expected range of input conditions, control variations, etc.*

        Efficacy is important to the specific part of the Marsbee system I am working on

Not at all	1	2	3	4	5	Extremely
Important						Important

25. *Resilience - The ability of a thing of interest to recover from adverse consequences.*

        Resilience is important to the specific part of the Marsbee system I am working on

Not at all	1	2	3	4	5	Extremely
Important						Important

26. The overall Marsbee system's cost is important to me.

Not at all	1	2	3	4	5	Extremely
Important						Important

27. The cost of the specific part of the Marsbee system I am working on is important to me.

Not at all	1	2	3	4	5	Extremely
Important						Important

28. *Mission - refers to the tasks that the system performs after development.*

        The mission success of the specific part of the Marsbee system I am working on is important to me

Not at all	1	2	3	4	5	Extremely
Important						Important

System Quality

29. How important are the Marsbee system's performance metrics (such as thrust of a rocket, range of an electric vehicle, bass quality of headphones, etc.) to me?

Not at all	1	2	3	4	5	Extremely
Important						Important

30. How important are the Marsbee system's attributes to me?

Not at all	1	2	3	4	5	Extremely
Important						Important

31. *Robustness - The thing of interest should not produce radical departures from its expected behavior is response to small changes to its operating input, internal state, or external environment.*

How important is the Marsbee system's robustness to me?

Not at all	1	2	3	4	5	Extremely
Important						Important

32. *Reliability - The ability of a thing of interest to perform as intended (i.e. without failure and within specified performance limits) for a specified time, in its life cycle conditions. It is a measure of how often the thing of interest fails.*

How important is the Marsbee system's reliability to me?

| Not at all Important | 1 | 2 | 3 | 4 | 5 | Extremely Important |

33. *Maintainability - The ease with which a thing of interest can be modified to correct faults, improve performance or other attributes, or adapt to a changed environment.*

How important is the Marsbee system's maintainability to me?

| Not at all Important | 1 | 2 | 3 | 4 | 5 | Extremely Important |

34. *Availability – The probability that a thing of interest will work as required when required during the period of a mission.*

How important is the Marsbee system's availability to me?

| Not at all Important | 1 | 2 | 3 | 4 | 5 | Extremely Important |

35. *Efficiency - The thing of interest produces the desired results with lesser expenditure of resources compared to competing alternatives.*

How important is the Marsbee system's efficiency to me?

| Not at all Important | 1 | 2 | 3 | 4 | 5 | Extremely Important |

36. *Profitability – The degree to which a business or activity yields profit or financial gain related to the thing of interest.*

How important is the Marsbee system's profitability to me?

| Not at all Important | 1 | 2 | 3 | 4 | 5 | Extremely Important |

37. *Efficacy - The thing of interest produces the anticipated behavior (or the expected output) over the expected range of input conditions, control variations, etc.*

How important is the Marsbee system's efficacy to me?

| Not at all Important | 1 | 2 | 3 | 4 | 5 | Extremely Important |

38. *Resilience - The ability of a thing of interest to recover from adverse consequences.*

How important is the Marsbee system's resilience to me?

		1	2	3	4	5	
Not at all		1	2	3	4	5	Extremely
Important							Important

39. How important is the Marsbee system's cost to me?

		1	2	3	4	5	
Not at all		1	2	3	4	5	Extremely
Important							Important

40. Mission refers to the tasks that the system performs after development.

How important is the Marsbee system's mission success to me?

		1	2	3	4	5	
Not at all		1	2	3	4	5	Extremely
Important							Important

41. Rank order the following system characteristics, with the top characteristic being most important to you and the bottom characteristic being the least important.
- Robustness   _____
- Reliability   _____
- Maintainability   _____
- Availability   _____
- Efficiency   _____
- Profitability   _____
- Efficacy   _____
- Resilience   _____

Note. Items below use a 5-point disagree–agree response format, in which 1 strongly disagree, 2 disagree, 3 neutral, 4 agree, and 5 strongly agree.

Personal

42. My personal preferences align with that of the team

	1	2	3	4	5	
Strongly	1	2	3	4	5	Strongly
Disagree						Agree

43. My personal preferences align with my role in the project

	1	2	3	4	5	
Strongly	1	2	3	4	5	Strongly
Disagree						Agree

44. My personal preferences align with the project's mission

	1	2	3	4	5	
Strongly	1	2	3	4	5	Strongly
Disagree						Agree

45. My personal preferences align with that of my superior

	1	2	3	4	5	
Strongly	1	2	3	4	5	Strongly
Disagree						Agree

46. I have clear goals for my job with regards to this project

	1	2	3	4	5	
Strongly	1	2	3	4	5	Strongly

| | Disagree | | | | | | Agree |

47. I know exactly what is expected of me with regards to this project

| | Strongly | 1 | 2 | 3 | 4 | 5 | Strongly |
| | Disagree | | | | | | Agree |

48. I understand my role in the team

| | Strongly | 1 | 2 | 3 | 4 | 5 | Strongly |
| | Disagree | | | | | | Agree |

Role clarity and ambiguity

49. I have clear, planned goals and objectives for my job with regards to this project

| | Strongly | 1 | 2 | 3 | 4 | 5 | Strongly |
| | Disagree | | | | | | Agree |

50. I know what my responsibilities with regards to this project are

| | Strongly | 1 | 2 | 3 | 4 | 5 | Strongly |
| | Disagree | | | | | | Agree |

51. I know exactly what is expected of me with regards to this project

| | Strongly | 1 | 2 | 3 | 4 | 5 | Strongly |
| | Disagree | | | | | | Agree |

52. I feel certain about how much responsibility I have on my job with regards to this project

| | Strongly | 1 | 2 | 3 | 4 | 5 | Strongly |
| | Disagree | | | | | | Agree |

53. Explanation is clear of what is to be done with regards to this project

| | Strongly | 1 | 2 | 3 | 4 | 5 | Strongly |
| | Disagree | | | | | | Agree |

54. I have to do things that should be done differently under different conditions

| | Strongly | 1 | 2 | 3 | 4 | 5 | Strongly |
| | Disagree | | | | | | Agree |

55. I have received assignments without the manpower to complete them with regards to this project

| | Strongly | 1 | 2 | 3 | 4 | 5 | Strongly |
| | Disagree | | | | | | Agree |

Project Specific

56. To me payload volume is important

| | Not at all | 1 | 2 | 3 | 4 | 5 | Extremely |
| | Important | | | | | | Important |

57. To me the distance Marsbee can travel on one charge is important

| | Not at all | 1 | 2 | 3 | 4 | 5 | Extremely |
| | Important | | | | | | Important |

58. To me data storage capacity is important

    Not at all   1   2   3   4   5   Extremely
    Important   Important

59. To me the overall size of Marsbee is important

    Not at all   1   2   3   4   5   Extremely
    Important   Important

60. To me the altitude the Marsbee can reach is important

    Not at all   1   2   3   4   5   Extremely
    Important   Important

61. To me flight duration is important

    Not at all   1   2   3   4   5   Extremely
    Important   Important

62. To me payload mass is important

    Not at all   1   2   3   4   5   Extremely
    Important   Important

63. To me the number of Marsbees sent to Mars in a single mission is important

    Not at all   1   2   3   4   5   Extremely
    Important   Important

64. To me the speed that a Marsbee acquires data is important

    Not at all   1   2   3   4   5   Extremely
    Important   Important

65. To me constant communication between the rover and the swarm of Marsbees is
    important

    Not at all   1   2   3   4   5   Extremely
    Important   Important

66. To me a direct/constant communication between every Marsbee and the rover is
    important

    Not at all   1   2   3   4   5   Extremely
    Important   Important

67. To me communication/interaction between the swarm of Marsbees is important

    Not at all   1   2   3   4   5   Extremely
    Important   Important

68. To me the wing flapping frequency is important

    Not at all   1   2   3   4   5   Extremely
    Important   Important

69. To me the ability of Marsbee to function with different sensors is important

    Not at all   1   2   3   4   5   Extremely
    Important   Important

70. To me battery capacity is important

    Not at all   1   2   3   4   5   Extremely

Important   Important

71. To me having the total mass of the Marsbee be under 6 grams is important

               Not at all   1   2   3   4   5   Extremely

               Important   Important

72. To me the ability of Marsbee to hover is important

               Not at all   1   2   3   4   5   Extremely

               Important   Important

73. To me the Marsbee having 2 wings is important

               Not at all   1   2   3   4   5   Extremely

               Important   Important

74. To me the Marsbee having 4 wings is important

               Not at all   1   2   3   4   5   Extremely

               Important   Important

75. To me it is important that the Marsbee be equipped with a radio

               Not at all   1   2   3   4   5   Extremely

               Important   Important

76. To me it is important that the Marsbee be equipped with pressure sensors

               Not at all   1   2   3   4   5   Extremely

               Important   Important

77. To me it is important that the Marsbee be equipped with RGB (red, green, blue) color sensors

               Not at all   1   2   3   4   5   Extremely

               Important   Important

78. To me it is important that the Marsbee be equipped with temperature sensors

               Not at all   1   2   3   4   5   Extremely

               Important   Important

79. To me it is important that the Marsbee be equipped with gas emission sensors

               Not at all   1   2   3   4   5   Extremely

               Important   Important

80. To me it is important that the Marsbee be equipped with a camera

               Not at all   1   2   3   4   5   Extremely

               Important   Important

81. To me it is important that the Marsbee be equipped with chemical composition sensors

               Not at all   1   2   3   4   5   Extremely

               Important   Important

82. To me it is important that the Marsbee be equipped with humidity sensors

               Not at all   1   2   3   4   5   Extremely

               Important   Important

83. To me it is important that the Marsbee be equipped with a spectrometer

               Not at all   1   2   3   4   5   Extremely

Important   Important

84. To me it is important that the Marsbee be equipped with an acoustic radar

        Not at all   1   2   3   4   5   Extremely
        Important   Important

85. To me it is important that the Marsbee be equipped with lidar

        Not at all   1   2   3   4   5   Extremely
        Important   Important

86. To me it is important that the Marsbee be equipped with a magnetometer

        Not at all   1   2   3   4   5   Extremely
        Important   Important

87. To me it is important that the Marsbee be equipped with temperature (thermal) sensors

        Not at all   1   2   3   4   5   Extremely
        Important   Important

Mission types

88. The primary mission of the Marsbee is to map the local terrain (within 50 yards from the rover)

        Strongly   1   2   3   4   5   Strongly
        Disagree   Agree

89. The primary mission of the Marsbee is to map distant terrain (over 100 yards from the rover)

        Strongly   1   2   3   4   5   Strongly
        Disagree   Agree

90. The primary mission of the Marsbee is to learn more about the Martian atmospheric structure (winds, pressure, etc.)

        Strongly   1   2   3   4   5   Strongly
        Disagree   Agree

91. The primary mission of the Marsbee is to learn more about the Martian atmospheric composition (chemistry)

        Strongly   1   2   3   4   5   Strongly
        Disagree   Agree

92. The primary mission of the Marsbee is to learn more about the Martian geology (land surface structure)

        Strongly   1   2   3   4   5   Strongly
        Disagree   Agree

93. The primary mission of the Marsbee is to learn more about the Martian soil's biochemistry (land surface composition)

        Strongly   1   2   3   4   5   Strongly
        Disagree   Agree

94. The primary mission of the Marsbee is to carry payload for a long distance

| | Strongly Disagree | 1 | 2 | 3 | 4 | 5 | Strongly Agree |

95. The Marsbee will be useful in monitoring a rover's path

| | Strongly Disagree | 1 | 2 | 3 | 4 | 5 | Strongly Agree |

96. The Marsbees will recharge at a charging station on Mars

| | Strongly Disagree | 1 | 2 | 3 | 4 | 5 | Strongly Agree |

97. The Marsbee charging station will be equipped on the rover

| | Strongly Disagree | 1 | 2 | 3 | 4 | 5 | Strongly Agree |

98. Marsbees will operate only in daylight

| | Strongly Disagree | 1 | 2 | 3 | 4 | 5 | Strongly Agree |

<u>Others</u>

1. Do you have the information you need at the time you make your decisions concerning the Marsbee system?

    _____
    _____
    _____
    _____
    _____

2. What do you value the most with regards to the Marsbee system in terms of performance metrics?

    _____
    _____
    _____
    _____
    _____

3. What are your objectives concerning the Marsbee system?

    _____
    _____
    _____
    _____
    _____

4. Is there a most important Marsbee subsystem, and if so which one?

    _____
    _____

_____
_____
_____

5. Are there aspects of the Marsbee system or design process that can be improved, and if so which one?

Table 1	
Team	Preference(s)
Wing	
Battery	
Chassis	
Tail	
Motor	
Gear Assembly	

_____
_____
_____
_____
_____

6. What do you believe other teammates prefer in regards to each subsystem? (Table 1)

7. Is there anything else you would like to add? Any comments or suggestions?

_____
_____
_____
_____
_____

Demographic Questionnaire

1. Gender: Male 1 Female 2 Other 3
2. Age: _____
3. What is your ethnic heritage?
   - African American
   - American Indian/Alaska Native
   - Asian
   - Caucasian
   - Hispanic /Latino
   - Multi-racial
   - Native Hawaiian/Pacific Islander
   - Other (please specify) _____
4. What is your role on the project?
   - Determine and validate the wing shape and motion to hover on Mars
   - Assess the feasibility of the Marsbee architecture in a mission context
   - Develop path-planning and control algorithms for 3D topographic mapping
5. What subsystem are you working on? (choose all that apply)
   - Wing
   - Battery
   - Chassis
   - Tail
   - Motor
   - Gear assembly
   - Other (please specify) _____
6. What is your highest degree?
   - Doctoral degree
   - Master's degree
   - Bachelor's degree
   - Associate degree
   - High school diploma
7. What university are you affiliated with?
   - University of Alabama in Huntsville
   - Tokyo University of Science
   - George Washington University
   - Other (please specify) _____

REFERENCES

1.   Young, L. A., Aiken, E. W., Derby, M. R., Demblewski, R. & Navarrete, J. "Experimental Investigation and Demonstration of Rotary-Wing Technologies for Flight in the Atmosphere of Mars," *AHSF02*, 58th Annual Forum of AHS, International; 11-13 Jun. 2002; Montreal; Canada, International; 11-13 Jun. 2002; Montreal; Canada,

2.   Ambrose, R. O., Allen, B. D., Mueller, R., Nesnas, I., Fong, T., Chandler, F., Matthies, L., Hinkel, H., Sylvester, A., Redlinger, M., Wilcox, B. & Stillwater, R. "2015 NASA Technology Roadmaps TA 4: Robotics and Autonomous Systems," *NASA*, 1–188, 2015

3.   Wall, M. "SpaceX's Elon Musk Unveils Interplanetary Spaceship to Colonize Mars (2016/9/27)," *Space.com*, http://www.space.com/34210-elon-musk-unveils-spacex-mars-colony-ship.html

4.   Thorbecke, C. "Space Race to Mars: Boeing CEO Says It Will Land People First (2016/10/5)," *ABC News*, http://abcnews.go.com/US/space-race-mars-boeing-ceo-put-man-mars/story?id=42584441

5.   Sullivan, R., Greeley, R., Kraft, M., Wilson, G., Golombek, M., Herkenhoff, K., Murphy, J. & Smith, P. "Results of the Imager for Mars Pathfinder windsock experiment," *Journal of Geophysical Research: Planets*, Vol. 105, 24547–24562, 2000 (doi: 10.1029/1999JE001234), http://doi.wiley.com/10.1029/1999JE001234

6.   Liu, H., Aono, H. & Tanaka, H. "Acta Futura Bioinspired Air Vehicles for Mars Exploration," *Acta Futura*, Vol. 6, 81–95, 2013 (doi: 10.2420/AF06.2013.81)

7.   Schofield, J. T., Barnes, J. R., Crisp, D., Haberle, R. M., Larsen, S., Magalhaes, J. A., Murphy, J. R., Seiff, A. & Wilson, G. "The Mars Pathfinder Atmospheric Structure Investigation/Meteorology (ASI/MET) Experiment," *Science*, Vol. 278, 1752–1758, 1997 (doi: 10.1126/science.278.5344.1752), http://www.sciencemag.org/cgi/doi/10.1126/science.278.5344.1752

8.   Shrestha, R., Benedict, M., Hrishikeshavan, V. & Chopra, I. "Hover Performance of a Small-Scale Helicopter Rotor for Flying on Mars," *Journal of Aircraft*, Vol. 53, 1160–1167, 2016 (doi: 10.2514/1.C033621), http://arc.aiaa.org/doi/10.2514/1.C033621

9.   Petrosyan, A., Galperin, B., Larsen, S. E., Lewis, S. R., Määttänen, A., Read, P. L., Renno, N., Rogberg, L. P. H. T., Savijärvi, H., Siili, T., Spiga, A., Toigo, A. & Vázquez, L. "The Martian Atmospheric Boundary Layer," *Reviews of Geophysics*, Vol. 49, RG3005, 2011 (doi: 10.1029/2010RG000351), http://doi.wiley.com/10.1029/2010RG000351

10.   Shyy, W., Aono, H., Kang, C. & Liu, H. *An Introduction to Flapping Wing Aerodynamics*, New York, Cambridge University Press, 2013

11.   Levine, J. S., Croom, M. A., Wright, H. S., Killough, B. D. & Edwards, W. C. "The Aerial Regional-Scale Environmental Surveyor (ARES): New Mars Science to Reduce Human Risk and Prepare for the Human Exploration," *Paper No. 4086, NF1676L-14788*, Workshop on Concepts and Approaches for Mars Exploration; 12-14 Jun. 2012; Houston, TX; United States, 2012

12.   Kuhl, C. A. "Mars Aerial Regional-Scale Environmental Survey (ARES) Coordinate

Systems Definitions and Transformations," *NASA TM-2009-215701*, 1–27, 2009

13. Braun, R. D., Wright, H. S., Croom, M. A., Levine, J. S. & Spencer, D. A. "Design of the ARES Mars Airplane and Mission Architecture," *Journal of Spacecraft and Rockets*, Vol. 43, 1026–1034, 2006 (doi: 10.2514/1.17956), http://arc.aiaa.org/doi/abs/10.2514/1.17956

14. Wright, H., Croom, M., Braun, R., Qualls, G., Cosgrove, P. & Levine, J. "ARES Mission Overview - Capabilities and Requirements of the Robotic Aerial Platform," *AIAA-2003-6577*, 2nd AIAA 'Unmanned Unlimited' Conf. and Workshop & Exhibit, 15 - 18 September 2003, San Diego, California, American Institute of Aeronautics and Astronautics, 2003 (http://arc.aiaa.org/doi/10.2514/6.2003-6577)

15. Sandford, S., Croom, M., Moses, R., Kuhl, C., Guynn, M., Braun, R., Levine, J. & Langford, J. "ARES and Beyond: Autonomous Aerial Platforms Provide a Unique Measurement Capability for Earth and Planetary Science," *AIAA 2003-6610*, 2nd AIAA 'Unmanned Unlimited' Conf. and Workshop & Exhibit, 15 - 18 September 2003, San Diego, California, American Institute of Aeronautics and Astronautics, 2003 (http://arc.aiaa.org/doi/10.2514/6.2003-6610)

16. Levine, J., Blaney, D., Connemey, J. E. P., Greeley, R., Head III, J., Hoffman, J., Jakosky, B., McKay, C., Sotin, C. & Summers, M. "Science from a Mars Airplane: The Aerial Regional-scale Environmental Survey (ARES) of Mars," *AIAA- 2003-6610*, 2nd AIAA 'Unmanned Unlimited' Conf. and Workshop & Exhibit, 15 - 18 September 2003, San Diego, California, American Institute of Aeronautics and Astronautics, 2003 (http://arc.aiaa.org/doi/10.2514/6.2003-6576)

17. Zubrin, R. "Mars Gashopper," *NASA Contract No.: NAS3-00074 Final Report* 2000

18. Thornblom, M. N., Lukas, J. N. & Lugo, R. A. "Systematic and Widespread Exploration with Aerocoasting and Reconnaissance of the Martian Sub-Atmosphere (SWARMS)," *Concepts and Approaches for Mars Exploration, held June 12-14, 2012 in Houston, Texas. LPI Contribution No. 1679, id.4135*, 2012

19. Wolf, A., Beegle, L., Raymond, C., Plaut, J., Pollard, B., Gim, Y., Wu, X. & Hall, J. "Mars Balloon Science," *Concepts and Approaches for Mars Exploration, held June 12-14, 2012 in Houston, Texas. LPI Contribution No. 1679, id.4294*, 2012

20. Hall, J., Pauken, M., Kerzhanovich, V., Walsh, G., Kulczycki, E., Fairbrother, D., Shreves, C. & Lachenmeier, T. "Mars Balloon Flight Test Results," *AIAA-2009-2809*, AIAA Balloon Systems Conference, 4-7 May 2009, Seattle, Washington, American Institute of Aeronautics and Astronautics, 2009 (http://arc.aiaa.org/doi/10.2514/6.2009-2809)

21. Colozza, A. & Michelson, R. C. "Planetary Exploration Using Biomimetics - An Entomopter for Flight on Mars," *NASA Institute for Advanced Concepts Phase II Project NAS5-98051* 2002

22. Bar-Cohen, Y., Colozza, A., Badescu, M., Sherrit, S. & Bao, X. "Biomimetic Flying Swarm of Entomopters for Mars Extreme Terrain Science Investigations," *Concepts and Approaches for Mars Exploration, held June 12-14, 2012 in Houston, Texas. LPI Contribution No. 1679, id.4075*, 2012

23. Colozza, A., Shahinpoor, M., Jenkins, P., Smith, C., Isaac, K. & DalBello, T. "Solid State

Aircraft Concept Overview," *2004 NASA/DoD Conference on Evolution Hardware (EH'04)*, 2004

24. Balaram, B. et al. "Mars Helicopter Technology Demonstrator," *AIAA 2018-0023*, 2018 AIAA Atmospheric Flight Mechanics Conference, Kissimmee, Florida, January 8-12, 2018, American Institute of Aeronautics and Astronautics, 2018

25. Bluman, J. E. & Kang, C. "Wing-wake interaction destabilizes hover equilibrium of a flapping insect-scale wing," *Bioinspiration & Biomimetics*, Vol. 12, 046004, 2017 (doi: 10.1088/1748-3190/aa7085), http://stacks.iop.org/1748-3190/12/i=4/a=046004?key=crossref.7459e3f2714111ab90e18f935d7a02ee

26. Keennon, M., Klingebiel, K., Won, H. & Andriukov, A. "Development of the Nano Hummingbird: A tailless flapping wing Micro Air Vehicle," *AIAA-2012-0588*, 50th AIAA Aerospace Sciences Meeting, 09 - 12 January 2012, Nashville, Tennessee, 2012

27. Nakata, T., Liu, H., Tanaka, Y., Nishihashi, N., Wang, X. & Sato, A. "Aerodynamics of a Bio-inspired Flexible Flapping-wing Micro Air Vehicle," *Bioinspiration & Biomimetics*, Vol. 6, 045002, 2011

28. Aono, H., Ozawa, Y., Yamamoto, M., Ishikawa, H., Kang, C., Nonomura, T. & Liu, H. "Effects of wing flexibility on sound characteristics of a four-wing flapping wing micro air vehicle," *The Journal of the Acoustical Society of America*, Vol. 140, 3421–3421, 2016 (doi: 10.1121/1.4971003), http://asa.scitation.org/doi/10.1121/1.4971003

29. Kang, C., Aono, H., Cesnik, C. E. S. & Shyy, W. "Effects of flexibility on the aerodynamic performance of flapping wings," *Journal of Fluid Mechanics*, Vol. 689, 32–74, 2011 (doi: 10.1017/jfm.2011.428)

30. Shyy, W., Aono, H., Chimakurthi, S. K. K., Trizila, P., Kang, C., Cesnik, C. E. S. E. S. & Liu, H. "Recent progress in flapping wing aerodynamics and aeroelasticity," *Progress in Aerospace Sciences*, Vol. 46, 284–327, 2010 (doi: 10.1016/j.paerosci.2010.01.001)

31. Tang, J., Viieru, D. & Shyy, W. "Effects of Reynolds Number and Flapping Kinematics on Hovering Aerodynamics," *AIAA Journal*, Vol. 46, 967–976, 2008 (doi: 10.2514/1.32191)

32. Bluman, J. E. & Kang, C. "Achieving hover equilibrium in free flight with a flexible flapping wing," *Journal of Fluids and Structures*, Vol. 75, 117–139, 2017 (doi: 10.1016/j.jfluidstructs.2017.08.011)

33. Shyy, W., Kang, C., Chirarattananon, P., Ravi, S. & Liu, H. "Aerodynamics, sensing and control of insect-scale flapping-wing flight," *Proceedings of the Royal Society A: Mathematical, Physical and Engineering Science*, Vol. 472, 20150712, 2016 (doi: 10.1098/rspa.2015.0712), http://rspa.royalsocietypublishing.org/lookup/doi/10.1098/rspa.2015.0712

34. Lau, G.-K., Chin, Y.-W., Goh, J. T.-W. & Wood, R. J. "Dipteran-Insect-Inspired Thoracic Mechanism With Nonlinear Stiffness to Save Inertial Power of Flapping-Wing Flight," *IEEE Transactions on Robotics*, Vol. 30, 1187–1197, 2014 (doi: 10.1109/TRO.2014.2333112), http://ieeexplore.ieee.org/document/6860250/

35. Blomgren, G. E. "The Development and Future of Lithium Ion Batteries," *Journal of The*

Electrochemical Society, Vol. 164, A5019–A5025, 2017 (doi: 10.1149/2.0251701jes), http://jes.ecsdl.org/lookup/doi/10.1149/2.0251701jes

36. New Energy and Industrial Technology Development Organization "NEDO Activity Report, Annual Report," 2016 (http://www.nedo.go.jp/content/100795560.pdf)

37. Vandenheede, R. B. R., Bernal, L. P., Morrison, C. L., Gogulapati, A., Friedmann, P. P., Kang, C. & Shyy, W. "Experimental and Computational Study on Flapping Wings with Bio-Inspired Hover Kinematics," *AIAA Journal*, Vol. 52, 1047–1058, 2014 (doi: 10.2514/1.J052644)

38. Ol, M. V., Bernal, L., Kang, C. K. & Shyy, W. "Shallow and deep dynamic stall for flapping low Reynolds number airfoils," *Animal Locomotion*, Vol. 46, 321–339, 2010 (doi: 10.1007/978-3-642-11633-9_26)

39. Kang, C., Aono, H., Baik, Y. S., Bernal, L. P. & Shyy, W. "Fluid dynamics of pitching and plunging flat plate at intermediate Reynolds numbers," *AIAA Journal*, Vol. 51, 315–329, 2013 (doi: 10.2514/1.J051593)

40. McElroy, T. & Landrum, D. B. "Simulated High-Altitude Testing of a COTS Electric UAV Motor," *AIAA 2012-1045*, 50th AIAA Aerospace Sciences Meeting including the New Horizons Forum and Aerospace Exposition 09 - 12 Jan, Nashville, Tennessee, Nashville, Tennessee, 2012

41. Sridhar, M. K., Kang, C., Landrum, D. B. & Aono, H. "Effects of altitude on the aerodynamic performance of Monarch butterflies," *AIAA 2017-0093*, 55th AIAA Aerospace Sciences Meeting, Grapevine, Texas, January 9 - 13, 2017, 2017

42. Saaty, T. L. "What is the Analytic Hierarchy Process?," *Mathematical Models for Decision Support*, 109–121, 1988

43. Akao, Y. *Quality function deployment*, New York, NY, NY, Productivity Press, 2004

44. Collopy, P. "Aerospace System Value Models: A Survey and Observations," *AIAA-2009-6560*, AIAA SPACE 2009 Conference & Exposition, 14 - 17 Septeber, 2004, Pasadena, CA, 14 - 17 Septeber, 2004, Pasadena, CA, American Institute of Aeronautics and Astronautics, 2009 (http://arc.aiaa.org/doi/10.2514/6.2009-6560)

45. Collopy, P., Bloebaum, C., Mesmer, B. & Green, L. "The Distinct and Interrelated Roles of Value-Driven Design, Multidisciplinary Design Optimization, and Decision Analysis," *AIAA-2012-5575*, 12th AIAA Aviation Technology, Integration, and Operations (ATIO) Conference and 14th AIAA/ISSMO Multidisciplinary Analysis and Optimization Conference, Indianapolis, IN, 17 - 19 September, 2012, Integration, and Operations (ATIO) Conference and 14th AIAA/ISSMO Multidisciplinary Analysis and Optimization Conference, Indianapolis, IN, 17 - 19 September, 2012, American Institute of Aeronautics and Astronautics, 2012 (http://arc.aiaa.org/doi/10.2514/6.2012-5575)

46. Collopy, P. D. & Hollingsworth, P. M. "Value-Driven Design," *Journal of Aircraft*, Vol. 48, 749–759, 2011 (doi: 10.2514/1.C000311), http://arc.aiaa.org/doi/10.2514/1.C000311

47. Goetzke, E. D., Bloebaum, C. L. & Mesmer, B. "Profit and Operational-Based Value Functions," *AIAA 2014-2432*, 15th AIAA/ISSMO Multidisciplinary Analysis and Optimization Conference, Atlanta, GA, Atlanta, GA, American Institute of Aeronautics

and Astronautics, 2014 (http://arc.aiaa.org/doi/10.2514/6.2014-2432)

48. Goetzke, E. D., Bloebaum, C. L. & Mesmer, B. "Value-Driven Design of Non-Commercial Systems using Bargain Modeling," *AIAA 2015-0134*, 56th AIAA/ASCE/AHS/ASC Structures, Structural Dynamics, and Materials Conference, Structural Dynamics, and Materials Conference, American Institute of Aeronautics and Astronautics, 2015 (http://arc.aiaa.org/doi/10.2514/6.2015-0134)

49. Topcu, T. G. & Mesmer, B. "Customer, Commercial, and Government Value Functions for Electric Vehicle System Design," *Proceedings of the 2015 Industrial and Systems Engineering Research Conference*, 959–968. Nashville, TN, TN, 2015

50. Browning, T. R. "Applying the design structure matrix to system decomposition and integration problems: a review and new directions," *IEEE Transactions on Engineering Management*, Vol. 48, 292–306, 2001 (doi: 10.1109/17.946528), http://ieeexplore.ieee.org/document/946528/

51. Eppinger, S. D. & Browning, T. R. *Design structure matrix methods and applications*, Cambridge, Massachusetts, MIT Press, 2012

52. Yassine, A. "An introduction to modeling and analyzing complex product development processes using the design structure matrix (DSM) method," *Urbana*, Vol. 51, 1–17, 2004

53. English, K. W. & Bloebaum, C. L. "Visual dependency structure matrix for multidisciplinary design optimization tradeoff studies," *Journal of Aerospace Computing, Information, and Communication*, Vol. 5, 274--297, 2008

54. Kannan, H., Bloebaum, C. L. & Mesmer, B. "Incorporation of Coupling Strength Models in Decomposition Strategies for Value-based MDO," *AIAA 2014-2430*, AIAA AVIATION Forum, Atlanta, GA,

55. Dyas, J. E., Clerkin, J. & Mesmer, B. "Value Modeling NASA Funding Allocations with a Congressional Stakeholder," *AIAA 2017-5327*, AIAA SPACE and Astronautics Forum and Exposition, AIAA SPACE Forum, Orlando, Florida, 12 - 14 September, 2017,

56. Kaufman, E. T. & Lee, T. "Autonomous Aerial Exploration for Topological Mapping of Mars Environments," AIAA 2019-1915, AIAA 2019 Scitech Forum, San Diego, California, January 7 - 11, 2019, 2019

57. Kang, C. & Shyy, W. "Scaling law and enhancement of lift generation of an insect-size hovering flexible wing," *Journal of Royal Society Interface*, Vol. 10, 20130361, 2013 (doi: 10.1098/rsif.2013.0361), https://sites.google.com/a/uah.edu/compfluidslab/files/2013_JRSInterface_Kang_etal.pdf

58. Magnan, A. *Le vol des insectes*, Paris, Hermann, 1934

59. Weis-fogh, T. "Quick estimates of flight fitness in hovering animals, including novel mechanisms for lift production," *Journal of Experimental Biology*, Vol. 59, 169–230, 1973

60. Ellington, C. P., van den Berg, C., Willmott, A. P. & Thomas, A. L. R. "Leading-edge vortices in insect flight," *Nature*, Vol. 384, 626–630, 1996 (doi: 10.1038/384626a0), http://www.nature.com/doifinder/10.1038/384626a0

61. Dickinson, M. H., Lehmann, F.-O. & Sane, S. P. "Wing rotation and the aerodynamic basis of insect flight," *Science*, Vol. 284, 1954–1960, 1999 (doi: 10.1126/science.284.5422.1954), http://www.ncbi.nlm.nih.gov/pubmed/10373107

62. Birch, J. M. & Dickinson, M. H. "The influence of wing-wake interactions on the production of aerodynamic forces in flapping flight," *Journal of Experimental Biology*, Vol. 206, 2257–2272, 2003 (doi: 10.1242/jeb.00381)

63. Sane, S. P. & Dickinson, M. H. "The aerodynamic effects of wing rotation and a revised quasi-steady model of flapping flight," *Journal of Experimental Biology*, Vol. 205, 1087–1096, 2002 , http://jeb.biologists.org/content/205/8/1087.long

64. Dudley, R. & Ellington, C. P. "Mechanics of forward flight in bumblebees I. Kinematics and morphology," *Journal of Experimental Biology*, Vol. 52, 19–52, 1990

65. Ardema, M. D., Chambers, M. C., Patron, A. P., Hahn, A. S., Miura, H. & Moore, M. D. "Estimation of Transport Aircraft Analytical Fuselage and Wing Weight," *NASA Technical Memorandum 110392* 1996

66. Bluman, J. E., Kang, C.-K., Landrum, D. B., Fahimi, F. & Mesmer, B. "Marsbee - Can a Bee Fly on Mars?," *AIAA-2017-0328*, 55th AIAA Aerospace Sciences Meeting, Grapevine, Texas, January 9-13, 2017

67. Bluman, J. E., Pohly, J. A., Sridhar, M. K., Kang, C. K., Landrum, D. B., Fahimi, F. & Aono, H. "Achieving bioinspired flapping wing hovering flight solutions on Mars via wing scaling," *Bioinspiration & Biomimetics*, Vol. 13, 046010, 2018 (doi: 10.1088/1748-3190/aac876), http://iopscience.iop.org/article/10.1088/1748-3190/aac876

68. Wood, R. J. "The first takeoff of a biologically inspired at-scale robotic insect," *IEEE Trans. Rob.*, Vol. 24, 341–347, 2008

69. Lentink, D. & Dickinson, M. H. "Rotational accelerations stabilize leading edge vortices on revolving fly wings," *Journal of Experimental Biology*, Vol. 212, 2705–2719, 2009 (doi: 10.1242/jeb.022269)

70. Usherwood, J. R. & Ellington, C. P. "The aerodynamics of revolving wings I. Model hawkmoth wings.," *The Journal of experimental biology*, Vol. 205, 1547–64, 2002 , http://www.ncbi.nlm.nih.gov/pubmed/12000800

71. Usherwood, J. R. & Ellington, C. P. "The aerodynamics of revolving wings II. Propeller force coefficients from mayfly to quail.," *The Journal of experimental biology*, Vol. 205, 1565–76, 2002

72. Nabawy, M. R. A. & Crowther, W. J. "On the quasi-steady aerodynamics of normal hovering flight part II: model implementation and evaluation," *Journal of The Royal Society Interface*, Vol. 11, 20131197–20131197, 2014 (doi: 10.1098/rsif.2013.1197)

73. Nabawy, M. R. A. & Crowthe, W. J. "A quasi-steady lifting line theory for insect-like hovering flight," *PLoS ONE*, Vol. 10, 1–18, 2015 (doi: 10.1371/journal.pone.0134972)

74. Trizila, P., Kang, C., Aono, H., Shyy, W. & Visbal, M. "Low-Reynolds-number aerodynamics of a flapping rigid flat plate," *AIAA Journal*, Vol. 49, 806–823, 2011 (doi: 10.2514/1.J050827),
https://sites.google.com/a/uah.edu/compfluidslab/files/2011_AIAA_Trizila_etal.pdf

75. Birch, J. M. & Dickinson, M. H. "Spanwise flow and the attachment of the leading-edge vortex on insect wings.," *Nature*, Vol. 412, 729–33, 2001 (doi: 10.1038/35089071), http://www.ncbi.nlm.nih.gov/pubmed/11507639

76. Shyy, W., Trizila, P., Kang, C.-K. & Aono, H. "Can tip vortices enhance lift of a flapping wing?," *AIAA Journal*, Vol. 47, 289–293, 2009 (doi: 10.2514/1.41732), https://sites.google.com/a/uah.edu/compfluidslab/files/2009_AIAAJLetter_Shyy_etal.pdf

77. Shyy, W. & Liu, H. "Flapping wings and aerodynamic lift: the role of leading-edge vortices," *AIAA Journal*, Vol. 45, 2817–2819, 2007 (doi: 10.2514/1.33205), http://cat.inist.fr/?aModele=afficheN&cpsidt=19924720

78. Wang, Z. J., Birch, J. M. & Dickinson, M. H. "Unsteady forces and flows in low Reynolds number hovering flight: two-dimensional computations vs robotic wing experiments," *Journal of Experimental Biology*, Vol. 207, 449–460, 2004 (doi: 10.1242/jeb.00739)

79. Bomphrey, R. J., Taylor, G. K., Lawson, N. J. & Thomas, A. L. R. "Digital particle image velocimetry measurements of the downwash distribution of a desert locust Schistocerca gregaria.," *Journal of the Royal Society, Interface / the Royal Society*, Vol. 3, 311–7, 2006 (doi: 10.1098/rsif.2005.0090), http://www.pubmedcentral.nih.gov/articlerender.fcgi?artid=1578738&tool=pmcentrez&rendertype=abstract

80. Bomphrey, R. J., Taylor, G. K. & Thomas, A. L. R. "Smoke visualization of free-flying bumblebees indicates independent leading-edge vortices on each wing pair," *Animal Locomotion*, 249–259, 2010 (doi: 10.1007/978-3-642-11633-9_20)

81. Berman, G. J. & Wang, Z. J. "Energy-minimizing kinematics in hovering insect flight," *Journal of Fluid Mechanics*, Vol. 582, 153, 2007 (doi: 10.1017/S0022112007006209), http://www.journals.cambridge.org/abstract_S0022112007006209

82. Badrya, C., Sridharan, A., Baeder, J. D. & Kroninger, C. M. "Multi-Fidelity Coupled Trim Analysis of a Flapping-Wing Micro Air Vehicle Flight," *Journal of Aircraft*, 1–17, 2017 (doi: 10.2514/1.C034236)

83. Sun, M. & Xiong, Y. "Dynamic flight stability of a hovering bumblebee," *Journal of Experimental Biology*, Vol. 208, 447–459, 2005 (doi: 10.1242/jeb.01407)

84. Faruque, I. & Humbert, J. S. "Dipteran insect flight dynamics. Part 1: Longitudinal motion about hover," *Journal of Theoretical Biology*, Vol. 264, 538–552, 2010 (doi: 10.1016/j.jtbi.2010.02.018), http://www.ncbi.nlm.nih.gov/pubmed/20170664

85. Aono, Hikaru; Liang, Fuyou; Liu, H. "Near- and far-field aerodynamics in insect hovering flight: an integrated computational study," *Journal of Experimental Biology*, Vol. 211, 239–257, 2008 (doi: 10.1242/jeb.008649), http://jeb.biologists.org/content/211/2/239.long

86. Sane, S. P. "The aerodynamics of insect flight," *Journal of Experimental Biology*, Vol. 206, 4191–4208, 2003 (doi: 10.1242/jeb.00663), http://jeb.biologists.org/cgi/doi/10.1242/jeb.00663

87. Ansari, S. A., Zbikowski, R. & Knowles, K. "Aerodynamic modelling of insect-like flapping flight for micro air vehicles," *Progress in Aerospace Sciences*, Vol. 42, 129–172, 2006 (doi: 10.1016/j.paerosci.2006.07.001)

88.   Ellington, C. P. "The Aerodynamics of Hovering Insect Flight. II. Morphological Parameters," *Philosophical Transactions of the Royal Society B: Biological Sciences*, Vol. 305, 17–40, 1984 (doi: 10.1098/rstb.1984.0050), http://rstb.royalsocietypublishing.org/cgi/doi/10.1098/rstb.1984.0050

89.   Engels, T., Kolomenskiy, D., Schneider, K., Lehmann, F.-O. & Sesterhenn, J. "Bumblebee Flight in Heavy Turbulence," *Phys. Rev. Lett.*, Vol. 116, 28103, 2016 (doi: 10.1103/PhysRevLett.116.028103)

90.   Dudley, R. & Ellington, C. P. "Mechanics of Forward Flight in Bumblebees II. Quasi-Steady Lift and Power Requirements," *Journal of Experimental Biology*, Vol. 148, 53–88, 1990

91.   Lau, G. K., Chin, Y. W., Goh, J. T. W. & Wood, R. J. "Dipteran-insect-inspired thoracic mechanism with nonlinear stiffness to save inertial power of flapping-wing flight," *IEEE Transactions on Robotics*, Vol. 30, 1187–1197, 2014 (doi: 10.1109/TRO.2014.2333112)

92.   Willmott, A. P. & Ellington, C. P. "The mechanics of flight in the hawkmoth Manduca sexta. Part I. Kinematics of hovering and forward flight," *Journal of Experimental Biology*, Vol. 200, 2705–2722, 1997

93.   Anderson, J. D. *Fundamentals of Aerodynamics*, 6th edn. Boston, McGraw-Hill, 2001

94.   Pohly, J., Kang, C., Sridhar, M. K., Landrum, D. B., Fahimi, F., Mesmer, B., Bluman, J. E., Aono, H. & Lee, T. "Scaling Bioinspired Mars Flight Vehicles for Hover," AIAA 2019-0567, AIAA 2019 Scitech Forum, San Diego, California, January 7 - 11, 2019, 2019

95.   Zheng, L., Hedrick, T. & Mittal, R. "A comparative study of the hovering efficiency of flapping and revolving wings," *Bioinspiration & biomimetics*, Vol. 8, 036001, 2013 (doi: 10.1088/1748-3182/8/3/036001)

96.   Azuma, A. *The biokinetics of flying and swimming*, Second. American Institute of Aeronautics and Astronautics, 2006

97.   Pohly, A. J., Salmon, L. J., Bluman, E. J., Nedunchezian, K. & Kang, C. "Quasi-Steady versus Navier–Stokes Solutions of Flapping Wing Aerodynamics," *Fluids* 2018

98.   Pohly, J., Sridhar, M. K., Bluman, J. E., Kang, C., Landrum, D. B., Fahimi, F., Aono, H. & Liu, H. "Payload and Power for Dynamically Similar Flapping Wing Hovering Flight on Mars," AIAA 2018-0020, AIAA Atmospheric Flight Mechanics Conference, Kissimmee, Florida, January 8 - 12, 2018, 2018

99.   Fry, S. N., Sayaman, R. & Dickinson, M. H. "The aerodynamics of hovering flight in Drosophila," *Journal of Experimental Biology*, Vol. 208, 2303–2318, 2005 (doi: 10.1242/jeb.01612), http://www.ncbi.nlm.nih.gov/pubmed/15939772

100.   Dudley, R. & Ellington, C. P. "Mechanics of forward flight in bumblebees I. Kinematics and morphology," *Journal of Experimental Biology*, Vol. 52, 19–52, 1990

101.   Han, J.-S., Chang, J. W. & Cho, H.-K. "Vortices behavior depending on the aspect ratio of an insect-like flapping wing in hover," *Experiments in Fluids*, Vol. 56, 181, 2015 (doi: 10.1007/s00348-015-2049-9)

102.   Lee, Y. J., Lua, K. B. & Lim, T. T. "Aspect ratio effects on revolving wings with Rossby

number consideration," *Bioinspiration and Biomimetics*, Vol. 11, 2016 (doi: 10.1088/1748-3190/11/5/056013)

103. Nabawy, M. R. A. & Crowther, W. J. "Aero-optimum hovering kinematics," *Bioinspiration & Biomimetics*, Vol. 10, 044002, 2015 (doi: 10.1088/1748-3190/10/4/044002)

104. Wu, P., Stanford, B. K., Sällström, E., Ukeiley, L. & Ifju, P. G. "Structural dynamics and aerodynamics measurements of biologically inspired flexible flapping wings.," *Bioinspiration & biomimetics*, Vol. 6, 016009, 2011 (doi: 10.1088/1748-3182/6/1/016009), http://www.ncbi.nlm.nih.gov/pubmed/21339627

105. Kang, C., Cranford, J., Sridhar, M. K., Kodali, D., Landrum, D. B. & Slegers, N. "Experimental Characterization of a Butterfly in Climbing Flight," *AIAA Journal*, Vol. 56, 15–24, 2018 (doi: 10.2514/1.J055360), https://arc.aiaa.org/doi/10.2514/1.J055360

106. Dickinson, M. H., Lehmann, F.-O. & Sane, S. P. "Wing Rotation and the Aerodynamics Basis of Insect Flight," *Science*, Vol. 284, 1954–1960, 1999 (doi: 10.1126/science.284.5422.1954)

107. Pimmler, T. U. & Eppinger, S. D. "Integration analysis of product decompositions," 1994

108. Sosa, M. E., Eppinger, S. D. & Rowles, C. M. "The Misalignment of Product Architecture and Organizational Structure in Complex Product Development," *Management Science*, Vol. 50, 1674–1689, 2004 (doi: 10.1287/mnsc.1040.0289)

109. Sosa, M. E., Eppinger, S. D. & Rowles, C. M. "Identifying Modular and Integrative Systems and Their Impact on Design Team Interactions," *Journal of Mechanical Design*, Vol. 125, 240–252, 2003 , http://dx.doi.org/10.1115/1.1564074

110. Pektaş, Ş. T. & Pultar, M. "Modelling detailed information flows in building design with the parameter-based design structure matrix," *Design Studies*, Vol. 27, 99–122, 2006 (doi: 10.1016/j.destud.2005.07.004), https://linkinghub.elsevier.com/retrieve/pii/S0142694X05000517

111. HAJELA, P., BLOEBAUM, C. L. & SOBIESZCZANSKI-SOBIESKI, J. "Application of global sensitivity equations in multidisciplinary aircraft synthesis," *Journal of Aircraft*, Vol. 27, 1002–1010, 1990 (doi: 10.2514/3.45974)

112. Yassine, A., Falkenburg, D. & Chelst, K. "Engineering design management: An information structure approach," *International Journal of Production Research*, Vol. 37, 2957–2975, 1999 (doi: 10.1080/002075499190374)

113. Clerkin, J. & Mesmer, B. "A Review of Value Modeling in the NASA Systems Engineering Research Consortium," 2018 Conference on Systems Engineering Research (CSER 2018), Charlottesville, VA, May, 2018,

114. Palma, G. E. & Mesmer, B. "A Preliminary Content Analysis of NASA's Nextstep-2 Habitat Documentation for Preference Representation," *AIAA 2018-0709*, 2018 AIAA Aerospace Sciences Meeting, AIAA SciTech Forum, Kissimmee, Florida, 8 - 12 January, 2018, 2018

115. Jet_Propulsion_Laboratory "Energy Storage Technologies for Future Planetary Science Missions," *JPL D-101146, https://solarsystem.nasa.gov/resources/549/energy-storage-*

technologies-for-future-planetary-science-missions/ 2017

116. Smart, M. C., Ratnakumar, B. V., Ewell, R. C., Surampudi, S., Puglia, F. J. & Gitzendanner, R. "The use of lithium-ion batteries for JPL's Mars missions," *Electrochimica Acta*, Vol. 268, 27–40, 2018 (doi: 10.1016/J.ELECTACTA.2018.02.020)

117. Smart, M. C., Ratnakumar, B. V, Krause, F. C., Whitcanack, L. D., Dewell, E. A., Dawson, S. F., Shaw, R. B. & Santee, S. "Performance Testing of Yardney Li-Ion Cells in Support of NASA's MSL and Insight Missions," *2015 NASA Aerospace Battery Workshop; 17-19 Nov. 2015; Huntsville, AL; United States* 2015

118. Nagasubramanian, G. "Electrical characteristics of 18650 Li-ion cells at low temperatures," *Journal of Applied Electrochemistry*, Vol. 31, 99–104, 2001 (doi: 10.1023/A:1004113825283)

119. Zhang, S. S., Xu, K. & Jow, T. R. "A new approach toward improved low temperature performance of Li-ion battery," *Electrochemistry Communications*, Vol. 4, 928–932, 2002 (doi: http://dx.doi.org/10.1016/S1388-2481(02)00490-3)

120. Zhang, S. S., Xu, K. & Jow, T. R. "The low temperature performance of Li-ion batteries," *Journal of Power Sources*, Vol. 115, 137–140, 2003 (doi: 10.1016/s0378-7753(02)00618-3)

121. Zhang, S. S., Xu, K. & Jow, T. R. "Electrochemical impedance study on the low temperature of Li-ion batteries," *Electrochimica Acta*, Vol. 49, 1057–1061, 2004 (doi: 10.1016/j.electacta.2003.10.016)

122. Zhang, S. S., Xu, K. & Jow, T. R. "Charge and discharge characteristics of a commercial LiCoO2-based 18650 Li-ion battery," *Journal of Power Sources*, Vol. 160, 1403–1409, 2006 (doi: 10.1016/j.jpowsour.2006.03.037)

123. Fan, J. "On the discharge capability and its limiting factors of commercial 18650 Li-ion cell at low temperatures," *Journal of Power Sources*, Vol. 117, 170–178, 2003 (doi: 10.1016/s0378-7753(03)00354-9)

124. Fan, J. & Tan, S. "Studies on Charging Lithium-Ion Cells at Low Temperatures," *Journal of the Electrochemical Society*, Vol. 153, A1081–A1092, 2006 (doi: 10.1149/1.2190029)

125. Jow, T. R., Zhang, S. S., Xu, K. & Allen, J. L. "Electrolytes for low temperature operations of Li-ion batteries," *Lithium-Ion Batteries: Materials and Devices - 210th ECS Meeting, October 29, 2006 - November 3, 2006*, 51–58. Cancun, Mexico, Electrochemical Society Inc., 2007

126. Ji, Y., Zhang, Y. & Wang, C.-Y. "Li-Ion Cell Operation at Low Temperatures," *Journal of The Electrochemical Society*, Vol. 160, A636–A649, 2013 (doi: 10.1149/2.047304jes)

127. Ouyang, M., Chu, Z., Lu, L., Li, J., Han, X., Feng, X. & Liu, G. "Low temperature aging mechanism identification and lithium deposition in a large format lithium iron phosphate battery for different charge profiles," *Journal of Power Sources*, Vol. 286, 309–320, 2015 (doi: http://dx.doi.org/10.1016/j.jpowsour.2015.03.178)

128. Abraham, D. P., Heaton, J. R., Kang, S. H., Dees, D. W. & Jansen, A. N. "Investigating the low-temperature impedance increase of lithium-ion cells," *Journal of the Electrochemical Society*, Vol. 155, A41–A47, 2008 (doi: 10.1149/1.2801366)

129. Lin, H. -p., Chua, D., Salomon, M., Shiao, H.-C., Hendrickson, M., Plichta, E. & Slane, S. "Low-Temperature Behavior of Li-Ion Cells," *Electrochemical and Solid-State Letters*, Vol. 4, A71–A73, 2001 (doi: 10.1149/1.1368736)

130. Ratnakumar, B. V & Smart, M. C. "Lithium Plating Behavior in Lithium-Ion Cells," *ECS Transactions*, Vol. 25, 241–252, 2010 (doi: 10.1149/1.3393860)

131. Zinth, V., Von Lüders, C., Hofmann, M., Hattendorff, J., Buchberger, I., Erhard, S., Rebelo-Kornmeier, J., Jossen, A. & Gilles, R. "Lithium plating in lithium-ion batteries at sub-ambient temperatures investigated by in situ neutron diffraction," *Journal of Power Sources* 2014 (doi: 10.1016/j.jpowsour.2014.07.168)

132. Petzl, M. & Danzer, M. A. "Nondestructive detection, characterization, and quantification of lithium plating in commercial lithium-ion batteries," *Journal of Power Sources* 2014 (doi: 10.1016/j.jpowsour.2013.12.060)

133. Petzl, M., Kasper, M. & Danzer, M. A. "Lithium plating in a commercial lithium-ion battery - A low-temperature aging study," *Journal of Power Sources* 2015 (doi: 10.1016/j.jpowsour.2014.11.065)

134. Waldmann, T., Hogg, B.-I., Kasper, M., Grolleau, S., Couceiro, C. G., Trad, K., Matadi, B. P. & Wohlfahrt-Mehrens, M. "Interplay of Operational Parameters on Lithium Deposition in Lithium-Ion Cells: Systematic Measurements with Reconstructed 3-Electrode Pouch Full Cells," *Journal of the Electrochemical Society*, Vol. 163, A1232–A1238, 2016 (doi: 10.1149/2.0591607jes)

135. Li, Z., Huang, J., Yann Liaw, B., Metzler, V. & Zhang, J. "A review of lithium deposition in lithium-ion and lithium metal secondary batteries," *Journal of Power Sources*, Vol. 254, 168–182, 2014 (doi: http://dx.doi.org/10.1016/j.jpowsour.2013.12.099)

136. Liu, Q., Du, C., Shen, B., Zuo, P., Cheng, X., Ma, Y., Yin, G. & Gao, Y. "Understanding undesirable anode lithium plating issues in lithium-ion batteries," *RSC Advances*, Vol. 6, 88683–88700, 2016 (doi: 10.1039/C6RA19482F)

137. Waldmann, T., Hogg, B. I. & Wohlfahrt-Mehrens, M. "Li plating as unwanted side reaction in commercial Li-ion cells – A review," *Journal of Power Sources* 2018

138. Yang, X.-G. & Wang, C.-Y. "Understanding the trilemma of fast charging, energy density and cycle life of lithium-ion batteries," *Journal of Power Sources*, Vol. 402, 489–498, 2018 (doi: https://doi.org/10.1016/j.jpowsour.2018.09.069)

139. Panasonic "Specifications for NCR18650BF https://www.orbtronic.com/content/ncr18650bf-panasonic-datasheet-specs.pdf," 2018

140. USDRIVE "Electrochemical Energy Storage Technical Team Roadmap," *https://www.energy.gov/sites/prod/files/2017/11/f39/EESTT%20roadmap%202017-10-16%20Final.pdf* 2017

141. Keil, P., Englberger, M. & Jossen, A. "Hybrid Energy Storage Systems for Electric Vehicles: An Experimental Analysis of Performance Improvements at Subzero Temperatures," *IEEE Transactions on Vehicular Technology*, Vol. PP, 1, 2015 (doi: 10.1109/TVT.2015.2486040)

142. Huang, C. -K., Sakamoto, J. S., Wolfenstine, J. & Surampudi, S. "The Limits of Low-

Temperature Performance of Li-Ion Cells," *Journal of the Electrochemical Society*, Vol. 147, 2893–2896, 2000 (doi: 10.1149/1.1393622)

143. Valoen, L. O. & Reimers, J. N. "Transport properties of LiPF6-based Li-ion battery electrolytes," *Journal of the Electrochemical Society*, Vol. 152, A882–A891, 2005 (doi: Doi 10.1149/1.1872737)

144. Gering, K. L. "Low-Temperature Performance Limitations of Lithium-Ion Batteries," *ECS Transactions*, Vol. 1, 119–149, 2006 (doi: 10.1149/1.2209364)

145. Zhu, G., Wen, K., Lv, W., Zhou, X., Liang, Y., Yang, F., Chen, Z., Zou, M., Li, J., Zhang, Y. & He, W. "Materials insights into low-temperature performances of lithium-ion batteries," *Journal of Power Sources*, Vol. 300, 29–40, 2015 (doi: https://doi.org/10.1016/j.jpowsour.2015.09.056)

146. Smart, M. C., Huang, C., Ratnakumar, B. V & Surampudi, S. "Development of advanced lithium-ion rechargeable cells with improved low temperature performance," *IECEC-97 Proceedings of the Thirty-Second Intersociety Energy Conversion Engineering Conference (Cat. No.97CH6203)*, 52–57 vol.1. 1997

147. Smart, M. C. "Electrolytes for Low-Temperature Lithium Batteries Based on Ternary Mixtures of Aliphatic Carbonates," *Journal of The Electrochemical Society*, Vol. 146, 486, 1999 (doi: 10.1149/1.1391633)

148. Ratnakumar, B. V., Smart, M. C., Huang, C. K., Perrone, D., Surampudi, S. & Greenbaum, S. G. "Lithium ion batteries for Mars exploration missions," *Electrochimica Acta*, Vol. 45, 1513–1517, 2000 (doi: 10.1016/S0013-4686(99)00367-9)

149. Smart, M. C., Ratnakumar, B. V & Surampudi, S. "Use of Organic Esters as Cosolvents in Electrolytes for Lithium-Ion Batteries with Improved Low Temperature Performance," *Journal of the Electrochemical Society*, Vol. 149, A361–A370, 2002 (doi: 10.1149/1.1453407)

150. Smart, M. C., Ratnakumar, B. V, Whitcanack, L. D., Chin, K. B., Surampudi, S., Croft, H., Tice, D. & Staniewicz, R. "Improved low-temperature performance of lithium-ion cells with quaternary carbonate-based electrolytes," *Journal of Power Sources*, Vol. 119–121, 349–358, 2003 (doi: http://dx.doi.org/10.1016/S0378-7753(03)00154-X)

151. Smart, M. C., Whitacre, J. F., Ratnakumar, B. V & Amine, K. "Electrochemical performance and kinetics of Li1+x(Co1/3Ni1/3Mn1/3)1−xO2 cathodes and graphite anodes in low-temperature electrolytes," *Journal of Power Sources*, Vol. 168, 501–508, 2007 (doi: http://dx.doi.org/10.1016/j.jpowsour.2006.10.106)

152. Smart, M. C., Ratnakumar, B. V., Behar, A., Whitcanack, L. D., Yu, J.-S. & Alamgir, M. "Gel polymer electrolyte lithium-ion cells with improved low temperature performance," *Journal of Power Sources*, Vol. 165, 535–543, 2007 (doi: 10.1016/j.jpowsour.2006.10.038)

153. Smart, M. C., Ratnakumar, B. V, Chin, K. B. & Whitcanack, L. D. "Lithium-Ion Electrolytes Containing Ester Cosolvents for Improved Low Temperature Performance," *Journal of the Electrochemical Society*, Vol. 157, A1361–A1374, 2010 (doi: 10.1149/1.3501236)

154. Smart, M. C. & Ratnakumar, B. V. "Effects of Electrolyte Composition on Lithium Plating in Lithium-Ion Cells," *Journal of The Electrochemical Society* 2011 (doi: 10.1149/1.3544439)

155. Smart, M. C., Lucht, B. L., Dalavi, S., Krause, F. C. & Ratnakumar, B. V "The Effect of Additives upon the Performance of MCMB/LiNixCo1−xO2 Li-Ion Cells Containing Methyl Butyrate-Based Wide Operating Temperature Range Electrolytes," *Journal of the Electrochemical Society*, Vol. 159, A739–A751, 2012 (doi: 10.1149/2.058206jes)

156. Smart, M. C., Hwang, C., Krause, F. C., Soler, J., West, W. C., Ratnakumar, B. V & Amine, K. "Wide Operating Temperature Range Electrolytes for High Voltage and High Specific Energy Li-Ion Cells," *ECS Transactions*, Vol. 50, 355–364, 2013 (doi: 10.1149/05026.0355ecst)

157. Smart, M. C., Krause, F. C., Jones, J.-P., Whitcanack, L. D., Ratnakumar, B. V, Brandon, E. J. & Shoesmith, M. "Low Temperature Electrolytes in High Specific Energy 18650 Li-Ion Cells for Future NASA Missions,", Vol. MA2016-02, 530, 2016

158. Smart, M. C., Bugga, R. V, Jones, J.-P., Krause, F. C., Brandon, E. J., Puglia, F. & Gitzendanner, R. "The Use of Ester Co-Solvent Based Low Temperature Electrolytes in Experimental and Large Capacity Prototype Graphite-LiNiCoAlO2 Lithium-Ion Cells," *Meeting Abstracts*, Vol. MA2017-01, 231–231, 2017

159. Jones, J.-P., Smart, M. C., Krause, F. C., Ratnakumar, B. V. & Brandon, E. J. "The Effect of Electrolyte Composition on Lithium Plating During Low Temperature Charging of Li-Ion Cells," *ECS Transactions*, Vol. 75, 1–11, 2017 (doi: 10.1149/07521.0001ecst)

160. Zhang, S. S., Xu, K., Allen, J. L. & Jow, T. R. "Effect of propylene carbonate on the low temperature performance of Li-ion cells," *Journal of Power Sources*, Vol. 110, 216–221, 2002 (doi: https://doi.org/10.1016/S0378-7753(02)00272-0)

161. Jow, T. R., Ding, M. S., Xu, K., Zhang, S. S., Allen, J. L., Amine, K. & Henriksen, G. L. "Nonaqueous electrolytes for wide-temperature-range operation of Li-ion cells," *Journal of Power Sources*, Vol. 119–121, 343–348, 2003 (doi: https://doi.org/10.1016/S0378-7753(03)00153-8)

162. Ein-Eli, Y., Thomas, S. R., Chadha, R., Blakley, T. J. & Koch, V. R. "Li-Ion Battery Electrolyte Formulated for Low-Temperature Applications," *Journal of the Electrochemical Society*, Vol. 144, 823–829, 1997 (doi: 10.1149/1.1837495)

163. Sazhin, S. V, Khimchenko, M. Y., Tritenichenko, Y. N. & Lim, H. S. "Performance of Li-ion cells with new electrolytes conceived for low-temperature applications," *Journal of Power Sources*, Vol. 87, 112–117, 2000 (doi: https://doi.org/10.1016/S0378-7753(99)00434-6)

164. Shiao, H. C., Chua, D., Lin, H., Slane, S. & Salomon, M. "Low temperature electrolytes for Li-ion PVDF cells," *Journal of Power Sources*, Vol. 87, 167–173, 2000 (doi: https://doi.org/10.1016/S0378-7753(99)00470-X)

165. Ren, Y. H., Yang, C. W., Wu, B. R., Zhang, C. Z., Chen, S. & Wu, F. "Novel low-temperature electrolyte for Li-ion Battery," *2011 International Conference on Advanced Engineering Materials and Technology, AEMT 2011, July 29, 2011 - July 31, 2011*, 1283–1289. Sanya, China, Trans Tech Publications, 2011

166. Li, S., Li, X., Liu, J., Shang, Z. & Cui, X. "A low-temperature electrolyte for lithium-ion batteries," *Ionics*, Vol. 21, 901–907, 2015 (doi: 10.1007/s11581-014-1275-0)

167. Mandal, B. K., Padhi, A. K., Shi, Z., Chakraborty, S. & Filler, R. "New low temperature electrolytes with thermal runaway inhibition for lithium-ion rechargeable batteries," *Journal of Power Sources*, Vol. 162, 690–695, 2006 (doi: 10.1016/j.jpowsour.2006.06.053)

168. Rustomji, C. S., Yang, Y., Kim, T. K., Mac, J., Kim, Y. J., Caldwell, E., Chung, H. & Meng, Y. S. "Liquefied gas electrolytes for electrochemical energy storage devices," *Science* 2017 (doi: 10.1126/science.aal4263)

169. Li, Y., Wong, K. W., Dou, Q., Zhang, W. & Ng, K. M. "Improvement of Lithium-Ion Battery Performance at Low Temperature by Adopting Ionic Liquid-Decorated PMMA Nanoparticles as Electrolyte Component," *ACS Applied Energy Materials*, Vol. 1, 2664–2670, 2018 (doi: 10.1021/acsaem.8b00355)

170. Dong, X., Guo, Z. Z., Guo, Z. Z., Wang, Y. & Xia, Y. "Organic Batteries Operated at −70°C," *Joule* 2018 (doi: https://doi.org/10.1016/j.joule.2018.01.017)

171. Zhang, S. S., Xu, K. & Jow, T. R. "Low temperature performance of graphite electrode in Li-ion cells," *Electrochimica Acta*, Vol. 48, 241–246, 2002 (doi: https://doi.org/10.1016/S0013-4686(02)00620-5)

172. Zhang, S. S., Xu, K. & Jow, T. R. "Study of the charging process of a LiCoO2-based Li-ion battery," *Journal of Power Sources*, Vol. 160, 1349–1354, 2006 (doi: http://dx.doi.org/10.1016/j.jpowsour.2006.02.087)

173. Jow, T. R., Delp, S. A., Allen, J. L., Jones, J.-P. & Smart, M. C. "Factors Limiting Li+ Charge Transfer Kinetics in Li-Ion Batteries," *Journal of the Electrochemical Society*, Vol. 165, A361–A367, 2018 (doi: 10.1149/2.1221802jes)

174. Jow, T. R., Allen, J. L., Marx, M., Nechev, K., Deveney, B. & Rickman, S. "Electrolytes, SEI and charge discharge kinetics of Li-ion batteries," *Rechargeable Lithium and Lithium-Ion Batteries - 216th ECS Meeting, October 4, 2009 - October 9, 2009*, 3–12. Vienna, Austria, Electrochemical Society Inc., 2010

175. Song, H.-S., Jeong, J.-B., Lee, B.-H., Shin, D.-H., Kim, B.-H., Kim, T.-H. & Heo, H. "Experimental study on the effects of pre-heating a battery in a low-temperature environment," *2012 IEEE Vehicle Power and Propulsion Conference*, 1198–1201. 2012

176. Jaguemont, J., Boulon, L. & Dubé, Y. "A comprehensive review of lithium-ion batteries used in hybrid and electric vehicles at cold temperatures," *Applied Energy*, Vol. 164, 99–114, 2016 (doi: 10.1016/j.apenergy.2015.11.034)

177. Zolot, M. D., Kelly, K., Keyser, M., Mihalic, M., Pesaran, A. & Hieronymus, A. "Thermal evaluation of the honda insight battery pack," *36th Intersociety Energy Conversion Engineering Conference (IECECi01) Savannah, Georgia, July 29 ñ August 2, 2001* 2001

178. Vlahinos, A. & Pesaran, A. A. "Energy Efficient Battery Heating in Cold Climates," *SAE Technical Paper 2002-01-1975*, 1–8, 2002

179. Ji, Y. & Wang, C. Y. "Heating strategies for Li-ion batteries operated from subzero temperatures," *Electrochimica Acta*, Vol. 107, 664–674, 2013 (doi:

http://dx.doi.org/10.1016/j.electacta.2013.03.147)

180. Richter, F., Kjelstrup, S., Vie, P. J. S. & Burheim, O. S. "Thermal conductivity and internal temperature profiles of Li-ion secondary batteries," *Journal of Power Sources*, Vol. 359, 592–600, 2017 (doi: https://doi.org/10.1016/j.jpowsour.2017.05.045)

181. Richter, F., Vie, P. J. S., Kjelstrup, S. & Burheim, O. S. "Measurements of ageing and thermal conductivity in a secondary NMC-hard carbon Li-ion battery and the impact on internal temperature profiles," *Electrochimica Acta*, Vol. 250, 228–237, 2017 (doi: https://doi.org/10.1016/j.electacta.2017.07.173)

182. Werner, D., Loges, A., Becker, D. J. & Wetzel, T. "Thermal conductivity of Li-ion batteries and their electrode configurations – A novel combination of modelling and experimental approach," *Journal of Power Sources*, Vol. 364, 72–83, 2017 (doi: https://doi.org/10.1016/j.jpowsour.2017.07.105)

183. Maleki, H., Hallaj, S. Al, Selman, J. R., Dinwiddie, R. B. & Wang, H. "Thermal Properties of Lithium-Ion Battery and Components," *Journal of the Electrochemical Society*, Vol. 146, 947–954, 1999

184. Stuart, T. A. & Hande, A. "HEV battery heating using AC currents," *Journal of Power Sources*, Vol. 129, 368–378, 2004 (doi: http://dx.doi.org/10.1016/j.jpowsour.2003.10.014)

185. Zhang, J., Ge, H., Li, Z. & Ding, Z. "Internal heating of lithium-ion batteries using alternating current based on the heat generation model in frequency domain," *Journal of Power Sources*, Vol. 273, 1030–1037, 2015 (doi: http://dx.doi.org/10.1016/j.jpowsour.2014.09.181)

186. Zuniga, M., Jaguemont, J., Boulon, L. & Dube, Y. "Heating Lithium-Ion Batteries with Bidirectional Current Pulses," *Vehicle Power and Propulsion Conference (VPPC), 2015 IEEE*, 1–6. 2015

187. Ge, H., Huang, J., Zhang, J. & Li, Z. "Temperature-Adaptive Alternating Current Preheating of Lithium-Ion Batteries with Lithium Deposition Prevention," *Journal of the Electrochemical Society*, Vol. 163, A290–A299, 2016 (doi: 10.1149/2.0961602jes)

188. Zhu, J., Sun, Z., Wei, X. & Dai, H. "An alternating current heating method for lithium-ion batteries from subzero temperatures," *International Journal of Energy Research*, Vol. 40, 1869–1883, 2016 (doi: 10.1002/er.3576)

189. Salehi, K. "Improving Low Temperature Performance of Lithium Ion Batterie," *Mechanical Engineering* 2004 , PhD thesis, The Pennsylvania State University

190. Wang, C.-Y., Zhang, G., Ge, S., Xu, T., Ji, Y., Yang, X.-G. & Leng, Y. "Lithium-ion battery structure that self-heats at low temperatures," *Nature*, Vol. 529, 2016 (doi: 10.1038/nature16502)

191. Zhang, G., Ge, S., Xu, T., Yang, X.-G., Tian, H. & Wang, C.-Y. "Rapid self-heating and internal temperature sensing of lithium-ion batteries at low temperatures," *Electrochimica Acta*, Vol. 218, 2016 (doi: 10.1016/j.electacta.2016.09.117)

192. Yang, X.-G., Zhang, G. & Wang, C.-Y. "Computational design and refinement of self-heating lithium ion batteries," *Journal of Power Sources*, Vol. 328, 2016 (doi: 10.1016/j.jpowsour.2016.08.028)

193. Zhang, G., Ge, S., Yang, X.-G., Leng, Y., Marple, D. & Wang, C.-Y. "Rapid restoration of electric vehicle battery performance while driving at cold temperatures," *Journal of Power Sources*, Vol. 371, 2017 (doi: 10.1016/j.jpowsour.2017.10.029)

194. Zhang, G., Tian, H., Ge, S., Marple, D., Sun, F. & Wang, C.-Y. "Visualization of self-heating of an all climate battery by infrared thermography," *Journal of Power Sources*, Vol. 376, 2018 (doi: 10.1016/j.jpowsour.2017.11.052)

195. Wang, C.-Y., Xu, T., Ge, S., Zhang, G., Yang, X.-G. & Ji, Y. "A fast rechargeable lithium-ion battery at subfreezing temperatures," *Journal of the Electrochemical Society*, Vol. 163, 2016 (doi: 10.1149/2.0681609jes)

196. Yang, X.-G., Zhang, G., Ge, S. & Wang, C.-Y. "Fast charging of lithium-ion batteries at all temperatures," *Proceedings of the National Academy of Sciences*, Vol. 115, 7266–7271, 2018 (doi: 10.1073/pnas.1807115115)

197. Du, Z., Wood, D. L., Daniel, C., Kalnaus, S. & Li, J. "Understanding limiting factors in thick electrode performance as applied to high energy density Li-ion batteries," *Journal of Applied Electrochemistry*, Vol. 47, 405–415, 2017 (doi: 10.1007/s10800-017-1047-4)

198. Jiang, F. & Peng, P. "Elucidating the Performance Limitations of Lithium-ion Batteries due to Species and Charge Transport through Five Characteristic Parameters," *Sci Rep*, Vol. 6, 32639, 2016 (doi: 10.1038/srep32639)

199. Arico, A. S., Bruce, P., Scrosati, B., Tarascon, J.-M. & Van Schalkwijk, W. "Nanostructured materials for advanced energy conversion and storage devices," *Nature Materials*, Vol. 4, 366–377, 2005 (doi: 10.1038/nmat1368)

200. Zaghib, K., Dontigny, M., Guerfi, A., Charest, P., Rodrigues, I., Mauger, A. & Julien, C. M. "Safe and fast-charging Li-ion battery with long shelf life for power applications," *Journal of Power Sources*, Vol. 196, 3949–3954, 2011 (doi: http://dx.doi.org/10.1016/j.jpowsour.2010.11.093)

201. Sun, Y.-K., Chen, Z., Noh, H.-J., Lee, D.-J., Jung, H.-G., Ren, Y., Wang, S., Yoon, C. S., Myung, S.-T. & Amine, K. "Nanostructured high-energy cathode materials for advanced lithium batteries," *Nature Materials*, Vol. 11, 942, 2012 (doi: 10.1038/nmat3435https://www.nature.com/articles/nmat3435#supplementary-information)

202. Hudak, N. S. "4 - Nanostructured Electrode Materials for Lithium-Ion Batteries," *Lithium-Ion Batteries*, 57–82, 2014

203. Du, Z., Li, J., Wood, M., Mao, C., Daniel, C. & Wood, D. L. "Three-dimensional conductive network formed by carbon nanotubes in aqueous processed NMC electrode," *Electrochimica Acta*, Vol. 270, 54–61, 2018 (doi: https://doi.org/10.1016/j.electacta.2018.03.063)

204. Li, J., Du, Z., Ruther, R. E., An, S. J., David, L. A., Hays, K., Wood, M., Phillip, N. D., Sheng, Y., Mao, C., Kalnaus, S., Daniel, C. & Wood, D. L. "Toward Low-Cost, High-Energy Density, and High-Power Density Lithium-Ion Batteries," *JOM*, Vol. 69, 1484–1496, 2017 (doi: 10.1007/s11837-017-2404-9)

205. DOE_Office_of_Science "Report of Basic Research Needs Workshop on Next Generation

Electric   Energy   Storage
https://science.energy.gov/~/media/bes/pdf/reports/2017/BRN_NGEES_rpt.pdf," 2017

206. Dai, Y. & Srinivasan, V. "On Graded Electrode Porosity as a Design Tool for Improving the Energy Density of Batteries," *Journal of the Electrochemical Society*, Vol. 163, A406–A416, 2016 (doi: 10.1149/2.0301603jes)

207. Thorat, I. V, Stephenson, D. E., Zacharias, N. A., Zaghib, K., Harb, J. N. & Wheeler, D. R. "Quantifying tortuosity in porous Li-ion battery materials," *Journal of Power Sources*, Vol. 188, 592–600, 2009 (doi: 10.1016/j.jpowsour.2008.12.032)

208. DuBeshter, T., Sinha, P. K., Sakars, A., Fly, G. W. & Jorne, J. "Measurement of Tortuosity and Porosity of Porous Battery Electrodes," *Journal of the Electrochemical Society*, Vol. 161, A599–A605, 2014 (doi: 10.1149/2.073404jes)

209. Pouraghajan, F., Knight, H., Wray, M., Mazzeo, B., Subbaraman, R., Christensen, J. & Wheeler, D. "Quantifying Tortuosity of Porous Li-Ion Battery Electrodes: Comparing Polarization-Interrupt and Blocking-Electrolyte Methods," *Journal of the Electrochemical Society*, Vol. 165, A2644–A2653, 2018 (doi: 10.1149/2.0611811jes)

210. Bae, C.-J., Erdonmez, C. K., Halloran, J. W. & Chiang, Y.-M. "Design of Battery Electrodes with Dual-Scale Porosity to Minimize Tortuosity and Maximize Performance," *Advanced Materials*, Vol. 25, 1254–1258, 2013 (doi: 10.1002/adma.201204055)

211. Sander, J. S., Erb, R. M., Li, L., Gurijala, A. & Chiang, Y. M. "High-performance battery electrodes via magnetic templating,", Vol. 1, 16099, 2016 (doi: 10.1038/nenergy.2016.99https://www.nature.com/articles/nenergy201699#supplementary-information)

212. Li, J., Smyrek, P., Wood, M., Zheng, Y., Sheng, Y., Rakebrandt, J.-H., Du, Z., Pfleging, W. & Wood, D. L. "Laser-Structured Electrodes for Lithium-Ion Batteries," *Meeting Abstracts*, Vol. MA2017-02, 584, 2017

213. Cobb, C. L. & Blanco, M. "Modeling mass and density distribution effects on the performance of co-extruded electrodes for high energy density lithium-ion batteries," *Journal of Power Sources*, Vol. 249, 357–366, 2014 (doi: https://doi.org/10.1016/j.jpowsour.2013.10.084)

214. Chen, C., Zhang, Y., Li, Y., Kuang, Y., Song, J., Luo, W., Wang, Y., Yao, Y., Pastel, G., Xie, J. & Hu, L. "Highly Conductive, Lightweight, Low-Tortuosity Carbon Frameworks as Ultrathick 3D Current Collectors," *Advanced Energy Materials*, Vol. 7, 1700595–n/a, 2017 (doi: 10.1002/aenm.201700595)

215. Diederichsen, K. M., McShane, E. J. & McCloskey, B. D. "Promising Routes to a High Li+ Transference Number Electrolyte for Lithium Ion Batteries," *ACS Energy Letters*, 2563–2575, 2017 (doi: 10.1021/acsenergylett.7b00792)

216. Li, Q., Chen, J., Fan, L., Kong, X. & Lu, Y. "Progress in electrolytes for rechargeable Li-based batteries and beyond," *Green Energy & Environment*, Vol. 1, 18–42, 2016 (doi: https://doi.org/10.1016/j.gee.2016.04.006)

217. Ramadesigan, V., Methekar, R. N., Latinwo, F., Braatz, R. D. & Subramanian, V. R. "Optimal porosity distribution for minimized ohmic drop across a porous electrode,"

Journal of the Electrochemical Society, Vol. 157, A1328–A1334, 2010 (doi: 10.1149/1.3495992)

218. Hosseinzadeh, E., Marco, J. & Jennings, P. "The impact of multi-layered porosity distribution on the performance of a lithium ion battery," *Applied Mathematical Modelling*, Vol. 61, 107–123, 2018 (doi: https://doi.org/10.1016/j.apm.2018.04.001)

219. Qi, Y., Jang, T., Ramadesigan, V., Schwartz, D. T. & Subramanian, V. R. "Is There a Benefit in Employing Graded Electrodes for Lithium-Ion Batteries?," *Journal of the Electrochemical Society*, Vol. 164, A3196–A3207, 2017 (doi: 10.1149/2.1051713jes)

220. Li, Q., Li, N., Ishida, M. & Zhou, H. "Saving electric energy by integrating a photoelectrode into a Li-ion battery," *Journal of Materials Chemistry A*, Vol. 3, 20903–20907, 2015 (doi: 10.1039/C5TA06908D)

221. Zuo, X., Zhu, J., Müller-Buschbaum, P. & Cheng, Y.-J. "Silicon based lithium-ion battery anodes: A chronicle perspective review," *Nano Energy*, Vol. 31, 113–143, 2017 (doi: https://doi.org/10.1016/j.nanoen.2016.11.013)

222. Cheng, X.-B., Zhang, R., Zhao, C.-Z. & Zhang, Q. "Toward Safe Lithium Metal Anode in Rechargeable Batteries: A Review," *Chemical Reviews*, Vol. 117, 10403–10473, 2017 (doi: 10.1021/acs.chemrev.7b00115)

223. Xu, W., Wang, J., Ding, F., Chen, X., Nasybulin, E., Zhang, Y. & Zhang, J.-G. "Lithium metal anodes for rechargeable batteries," *Energy and Environmental Science*, Vol. 7, 513–537, 2014 (doi: 10.1039/c3ee40795k)

224. Shi, J.-L., Xiao, D.-D., Ge, M., Yu, X., Chu, Y., Huang, X., Zhang, X.-D., Yin, Y.-X., Yang, X.-Q., Guo, Y.-G., Gu, L. & Wan, L.-J. "High-Capacity Cathode Material with High Voltage for Li-Ion Batteries," *Advanced Materials*, Vol. 30, 1705575, 2018 (doi: doi:10.1002/adma.201705575)

225. Schipper, F., Erickson, E. M., Erk, C., Shin, J.-Y., Chesneau, F. F. & Aurbach, D. "Review—Recent Advances and Remaining Challenges for Lithium Ion Battery Cathodes: I. Nickel-Rich, LiNixCoyMnzO2," *Journal of the Electrochemical Society*, Vol. 164, A6220–A6228, 2017 (doi: 10.1149/2.0351701jes)

226. Nitta, N., Wu, F., Lee, J. T. & Yushin, G. "Li-ion battery materials: present and future," *Materials Today*, Vol. 18, 252–264, 2015 (doi: http://dx.doi.org/10.1016/j.mattod.2014.10.040)

227. Li, J., Ma, C., Chi, M., Liang, C. & Dudney, N. J. "Solid Electrolyte: the Key for High-Voltage Lithium Batteries," *Advanced Energy Materials*, Vol. 5, 1401408, 2015 (doi: doi:10.1002/aenm.201401408)

228. Chen, S., Wen, K., Fan, J., Bando, Y. & Golberg, D. "Progress and future prospects of high-voltage and high-safety electrolytes in advanced lithium batteries: from liquid to solid electrolytes," *Journal of Materials Chemistry A*, Vol. 6, 11631–11663, 2018 (doi: 10.1039/C8TA03358G)

229. Zhan, C., Cai, F., Amine, K. & Lu, J. "Advanced Lithium Batteries for Automobile Applications at ABAA-9," *ACS Energy Letters*, Vol. 2, 1628–1631, 2017 (doi: 10.1021/acsenergylett.7b00407)

230. Thomas, J. P. & Qidwai, M. A. "The design and application of multifunctional structure-battery materials systems," *JOM*, Vol. 57, 18–24, 2005 (doi: 10.1007/s11837-005-0228-5)

231. Roberts, S. C. & Aglietti, G. S. "Satellite multi-functional power structure: Feasibility and mass savings," *Proceedings of the Institution of Mechanical Engineers, Part G: Journal of Aerospace Engineering*, Vol. 222, 41–51, 2008 (doi: 10.1243/09544100jaero255)

232. Singh, A. K., Cao, L., Ma, J., Seo, J., Bakis, C. E., Zhang, Y., Hickner, M. A. & Rahn, C. D. "Design, manufacture and test of a novel structural battery based on sandwich construction," *Journal of Sandwich Structures & Materials*, Vol. 17, 666–690, 2015 (doi: 10.1177/1099636215591908)

233. Zhang, Y., Ma, J., Singh, A. K., Cao, L., Seo, J., Rahn, C. D., Bakis, C. E. & Hickner, M. A. "Multifunctional structural lithium-ion battery for electric vehicles," *Journal of Intelligent Material Systems and Structures*, Vol. 28, 1603–1613, 2017 (doi: 10.1177/1045389x16679021)

234. Ma, J., Rahn, C. & Frecker, M. "Multifunctional NMC-Si Batteries With Self-Actuation and Self-Sensing,", V001T01A010, 2017 (doi: 10.1115/SMASIS2017-3886)

235. Bi, Z., Song, L., De Kleine, R., Mi, C. C. & Keoleian, G. A. "Plug-in vs. wireless charging: Life cycle energy and greenhouse gas emissions for an electric bus system," *Applied Energy*, Vol. 146, 11–19, 2015 (doi: https://doi.org/10.1016/j.apenergy.2015.02.031)

236. Bi, Z., Kan, T., Mi, C. C., Zhang, Y., Zhao, Z. & Keoleian, G. A. "A review of wireless power transfer for electric vehicles: Prospects to enhance sustainable mobility," *Applied Energy*, Vol. 179, 413–425, 2016 (doi: https://doi.org/10.1016/j.apenergy.2016.07.003)

237. Kalwar, K. A., Aamir, M. & Mekhilef, S. "Inductively coupled power transfer (ICPT) for electric vehicle charging – A review," *Renewable and Sustainable Energy Reviews*, Vol. 47, 462–475, 2015 (doi: https://doi.org/10.1016/j.rser.2015.03.040)

238. Fisher, T. M., Farley, K. B., Gao, Y., Bai, H. & Tse, Z. T. H. "Electric vehicle wireless charging technology: a state-of-the-art review of magnetic coupling systems," *Wireless Power Transfer*, Vol. 1, 87–96, 2014 (doi: 10.1017/wpt.2014.8)

239. Tavakoli, R. & Pantic, Z. "Analysis, Design, and Demonstration of a 25-kW Dynamic Wireless Charging System for Roadway Electric Vehicles," *IEEE Journal of Emerging and Selected Topics in Power Electronics*, Vol. 6, 1378–1393, 2018 (doi: 10.1109/JESTPE.2017.2761763)

240. Bi, Z., Keoleian, G. A. & Ersal, T. "Wireless charger deployment for an electric bus network: A multi-objective life cycle optimization," *Applied Energy*, Vol. 225, 1090–1101, 2018 (doi: https://doi.org/10.1016/j.apenergy.2018.05.070)

241. Long, T., Ozger, M., Cetinkaya, O. & Akan, O. B. "Energy Neutral Internet of Drones," *IEEE Communications Magazine*, Vol. 56, 22–28, 2018 (doi: 10.1109/MCOM.2017.1700454)

242. Vincent, D., Huynh, P. S., Patnaik, L. & Williamson, S. S. "Prospects of Capacitive Wireless Power Transfer (C-WPT) for Unmanned Aerial Vehicles," *2018 IEEE PELS Workshop on Emerging Technologies: Wireless Power Transfer (Wow)*, 1–5. 2018

243. Lu, M., Bagheri, M., James, A. P. & Phung, T. "Wireless Charging Techniques for UAVs: A Review, Reconceptualization, and Extension," *IEEE Access*, Vol. 6, 29865–29884, 2018 (doi: 10.1109/ACCESS.2018.2841376)

244. Campi, T., Cruciani, S. & Feliziani, M. "Wireless Power Transfer Technology Applied to an Autonomous Electric UAV with a Small Secondary Coil," *Energies*, Vol. 11, 352, 2018

245. Guo, W., Xue, X., Wang, S., Lin, C. & Wang, Z. L. "An Integrated Power Pack of Dye-Sensitized Solar Cell and Li Battery Based on Double-Sided TiO2 Nanotube Arrays," *Nano Letters*, Vol. 12, 2520–2523, 2012 (doi: 10.1021/nl3007159)

246. Paolella, A. et al. "Light-assisted delithiation of lithium iron phosphate nanocrystals towards photo-rechargeable lithium ion batteries," *Nature Communications*, Vol. 8, 14643, 2017 (doi: 10.1038/ncomms14643), http://www.nature.com/doifinder/10.1038/ncomms14643

247. Li, Q., Liu, Y., Guo, S. & Zhou, H. "Solar energy storage in the rechargeable batteries," *Nano Today*, Vol. 16, 46–60, 2017 (doi: https://doi.org/10.1016/j.nantod.2017.08.007)

248. Gurung, A. & Qiao, Q. "Solar Charging Batteries: Advances, Challenges, and Opportunities," *Joule*, Vol. 2, 1217–1230, 2018 (doi: https://doi.org/10.1016/j.joule.2018.04.006)

249. Nandini, K., Usha, K., Srinivasan, M. S., Pramod, M., Satyanarayana, P. & Sankaran, M. "Study on survivability of 18650 Lithium-ion cells at cryogenic temperatures," *Journal of Energy Storage*, Vol. 17, 409–416, 2018 (doi: https://doi.org/10.1016/j.est.2018.03.018)

250. Aasen, S., Page, A. M., Skjolden Skau, K. & Nygaard, T. A. "Effect of foundation modelling on the fatigue lifetime of a monopile-based offshore wind turbine," *Wind Energy Science*, Vol. 2, 361–376, 2017 (doi: 10.5194/wes-2-361-2017), https://www.wind-energ-sci.net/2/361/2017/

251. Tomic, T., Schmid, K., Lutz, P., Mathers, A. & Haddadin, S. "The flying anemometer: Unified estimation of wind velocity from aerodynamic power and wrenches," *2016 IEEE/RSJ International Conference on Intelligent Robots and Systems (IROS)*, 1637–1644. IEEE, 2016 (http://ieeexplore.ieee.org/document/7759264/)

252. Smith, D. E. "The Global Topography of Mars and Implications for Surface Evolution," *Science*, Vol. 284, 1495–1503, 1999 (doi: 10.1126/science.284.5419.1495), http://www.sciencemag.org/cgi/doi/10.1126/science.284.5419.1495

253. Thrun, S., Burgard, W. & Fox, D. *Probabilistic Robotics*, Cambridge, Massachusetts, Massachusetts Institute of Technology, 2005

254. Kai M., W., Hornung, A., Bennewitz, M., Stachniss, C. & Burgard, W. "OctoMap: A probabilistic, flexible, and compact 3D map representation for robotic systems," *In Proc. of the ICRA 2010 Workshop on Best Practice in 3D Perception and Modeling for Mobile Manipulation* 2010

255. Kaufman, E., Taeyoung Lee, Zhuming Ai & Moskowitz, I. S. "Bayesian occupancy grid mapping via an exact inverse sensor model," *2016 American Control Conference (ACC)*, 5709–5715. IEEE, 2016 (http://ieeexplore.ieee.org/document/7526564/)

256. Kaufman, E., Takami, K., Lee, T. & Ai, Z. "Autonomous Exploration with Exact Inverse Sensor Models," *Journal of Intelligent & Robotic Systems*, Vol. 92, 435–452, 2018 (doi: 10.1007/s10846-017-0710-7), https://doi.org/10.1007/s10846-017-0710-7

257. Zhu, C., Ding, R., Lin, M. & Wu, Y. "A 3D Frontier-Based Exploration Tool for MAVs," *2015 IEEE 27th International Conference on Tools with Artificial Intelligence (ICTAI)*, 348–352. IEEE, 2015 (http://ieeexplore.ieee.org/document/7372156/)

258. Senarathne, P. G. C. N. & Wang, D. "Towards autonomous 3D exploration using surface frontiers," *2016 IEEE International Symposium on Safety, Security, and Rescue Robotics (SSRR)*, 34–41. IEEE, 2016 (http://ieeexplore.ieee.org/document/7784274/)

259. Dornhege, C. & Kleiner, A. "A frontier-void-based approach for autonomous exploration in 3d," *2011 IEEE International Symposium on Safety, Security, and Rescue Robotics*, 351–356. IEEE, 2011 (http://ieeexplore.ieee.org/document/6106778/)

260. Stachniss, C., Grisetti, G. & Burgard, W. "Information Gain-based Exploration Using Rao-Blackwellized Particle Filters," *Robotics: Science and Systems I*, Robotics: Science and Systems Foundation, 2005 (http://www.roboticsproceedings.org/rss01/p09.pdf)

261. Kaufman, E., Lee, T. & Ai, Z. "Autonomous exploration by expected information gain from probabilistic occupancy grid mapping," *2016 IEEE International Conference on Simulation, Modeling, and Programming for Autonomous Robots (SIMPAR)*, 246–251. IEEE, 2016 (http://ieeexplore.ieee.org/document/7862403/)

262. Kaufman, E., Takami, K., Ai, Z. & Lee, T. "Autonomous Quadrotor 3D Mapping and Exploration Using Exact Occupancy Probabilities," *2018 Second IEEE International Conference on Robotic Computing (IRC)*, 49–55. IEEE, 2018 (http://ieeexplore.ieee.org/document/8329880/)

263. Maurović, I., Đakulović, M. & Petrović, I. "Autonomous Exploration of Large Unknown Indoor Environments for Dense 3D Model Building," *IFAC Proceedings Volumes*, Vol. 47, 10188–10193, 2014 (doi: 10.3182/20140824-6-ZA-1003.01275), https://linkinghub.elsevier.com/retrieve/pii/S1474667016432301

264. Dijkstra, E. "A note on two problems in connexion with graphs," *Numerische Mathematik*, Vol. 1, 269–271, 1959

265. Johnson, S. G. "Saddle-point integration of C_∞ 'bump' functions," *arXiv:1508.04376* 2015 , http://arxiv.org/abs/1508.04376

266. USGS Astrogeology Research Program "Map-a-Planet: Data Sets," 2013

267. Lee, T. "A video of Case 1," 2018

268. National Academy of Science *NASA Space Technology Roadmaps and Priorities Revisited*, Washington, D.C., D.C., National Academies Press, 2016

269. Zhang, G., Ge, S., Xu, T., Yang, X.-G., Tian, H. & Wang, C.-Y. "Rapid self-heating and internal temperature sensing of lithium-ion batteries at low temperatures," *Electrochimica Acta*, Vol. 218, 149–155, 2016 (doi: 10.1016/j.electacta.2016.09.117), http://linkinghub.elsevier.com/retrieve/pii/S0013468616320357

270. Wang, C.-Y., Zhang, G., Ge, S., Xu, T., Ji, Y., Yang, X.-G. & Leng, Y. "Lithium-ion

battery structure that self-heats at low temperatures," *Nature*, Vol. 529, 515–518, 2016 (doi: 10.1038/nature16502), https://www.nature.com/articles/nature16502

271. Zhang, G., Ge, S., Yang, X.-G., Leng, Y., Marple, D. & Wang, C.-Y. "Rapid restoration of electric vehicle battery performance while driving at cold temperatures," *Journal of Power Sources*, Vol. 371, 35–40, 2017 (doi: 10.1016/j.jpowsour.2017.10.029), http://linkinghub.elsevier.com/retrieve/pii/S0378775317313617

272. Wang, C.-Y., Xu, T., Ge, S., Zhang, G., Yang, X.-G. & Ji, Y. "A Fast Rechargeable Lithium-Ion Battery at Subfreezing Temperatures," *Journal of The Electrochemical Society*, Vol. 163, A1944–A1950, 2016 (doi: 10.1149/2.0681609jes), http://jes.ecsdl.org/lookup/doi/10.1149/2.0681609jes

273. Hou, Z., Gao, H. & Lewis, F. L. "Data-Driven Control and Learning Systems," *IEEE Transactions on Industrial Electronics*, Vol. 64, 4070–4075, 2017 (doi: 10.1109/TIE.2017.2653767), http://ieeexplore.ieee.org/document/7895273/

274. Formentin, S., van Heusden, K. & Karimi, A. "A comparison of model-based and data-driven controller tuning," *International Journal of Adaptive Control and Signal Processing*, Vol. 28, 882–897, 2014 (doi: 10.1002/acs.2415), http://doi.wiley.com/10.1002/acs.2415

275. Gibo, D. L. "Altitudes Attained By Migrating Monarch Butterflies, Danaus P. Plexippus (Lepidoptera: Danainae), as Reported By Glider Pilots," *Canadian Journal of Zoology*, Vol. 59, 571–572, 1981

276. Brower, L. "Monarch butterfly orientation: missing pieces of a magnificent puzzle," *The Journal of Experimental Biology*, Vol. 199, 93–103, 1996 , http://www.ncbi.nlm.nih.gov/pubmed/9317405

277. Srygley, R. B., Dudley, R., Oliveira, E. G. & Riveros, A. J. "El Niño, Host Plant Growth, and Migratory Butterfly Abundance in a Changing Climate," *Biotropica*, Vol. 46, 90–97, 2014 (doi: 10.1111/btp.12081)

278. Templin, R. J. "Spectrum of animal flight: Insects to pterosaurs," *Progress in Aerospace Sciences*, Vol. 36, 393–436, 2000 (doi: 10.1016/S0376-0421(00)00007-5)

279. Masters, A. R., Malcolm, S. B. & Brower, L. P. "Monarch Butterfly (Danaus Plexippus) Thermoregulatory Behavior and Adaptations for Overwintering in Mexico," *Ecology*, Vol. 69, 458, 1988 (doi: 10.2307/1940444), http://www.jstor.org/stable/1940444?origin=crossref

280. Merlin, C., Gegear, R. J. & Reppert, S. M. "Antennal Circadian Clocks Coordinate Sun Compass Orientation in Migratory Monarch Butterflies," *Science*, Vol. 325, 1700–1704, 2009 (doi: 10.1126/science.1176221), http://www.sciencemag.org/cgi/doi/10.1126/science.1176221

281. Simpson, T. W. & Martins, J. R. R. A. "Multidisciplinary Design Optimization for Complex Engineered Systems: Report From a National Science Foundation Workshop," *Journal of Mechanical Design*, Vol. 133, 101002, 2011 (doi: 10.1115/1.4004465), http://mechanicaldesign.asmedigitalcollection.asme.org/article.aspx?articleid=1450669

282. Bloebaum, C. L., Collopy, P. D. & Hazelrigg, G. A. "NSF/NASA Workshop on the

Design of Large-Scale Complex Engineered Systems - From Research to Product Realization," *AIAA 2012-5572*, 12th AIAA Aviation Technology, Integration, and Operations (ATIO) Conference and 14th AIAA/ISSM, 17 - 19 September 2012, Indianapolis, Indiana, Integration, and Operations (ATIO) Conference and 14th AIAA/ISSM, 17 - 19 September 2012, Indianapolis, Indiana, 2012

283. Collopy, P. D. "Final Report: National Science Foundation Workshop on the Design of Large Scale Complex Systems," *University of Alabama in Hunsville: Center for System Studies* 2011